Construction and Testing of a Portable Time Projection Chamber for Fast Neutron Detection

by

William L Koch

B.S. Physics, United States Military Academy at West Point (2004)
S.M. Physics, Massachusetts Institute of Technology (2013)

Submitted to the Department of Nuclear Science and Engineering
in partial fulfillment of the requirements for the degree of

Doctor of Philosophy in Nuclear Science and Engineering

at the

MASSACHUSETTS INSTITUTE OF TECHNOLOGY

June 2021

Author .....
William L Koch
Department of Nuclear Science and Engineering
May 26, 2021

Certified by .....
Areg Danagoulian
Associate Professor of Nuclear Science and Engineering
Thesis Supervisor

Certified by .....
Richard C. Lanza
Senior Research Scientist, Nuclear Science and Engineering
Thesis Reader

Accepted by .....
Ju Li
Battelle Energy Alliance Professor of Nuclear Science and Engineering
Professor of Materials Science and Engineering
Chair, Department Committee on Graduate Students

Construction and Testing of a Portable Time Projection Chamber for Fast Neutron Detection

by

William L Koch

Submitted to the Department of Nuclear Science and Engineering
on May 26, 2021, in partial fulfillment of the
requirements for the degree of
Doctor of Philosophy in Nuclear Science and Engineering

Abstract

The need to closely monitor the flow of nuclear fuel through the entire fuel cycle is an increasingly important component of global security. Closely connected to this monitoring is the need for improved radiation detectors. Gamma ray detectors experienced a boom in development over the last half century, but neutron detectors have met a higher level of resistance. When monitoring for the potential proliferation of irradiated nuclear fuel, the fast neutron signature from the spontaneous fission of Plutonium-240 offers a window of opportunity for interdicting illicit nuclear material movement. Directly detecting fast neutrons, as opposed to reaction-based detectors that rely on signal moderation, retains the directional information which can be used to offset low intrinsic efficiency for fast neutron detection. There are currently no portable, directional fast neutron detectors built to date.

This work presents an investigation to build a one-person portable Time Projection Chamber (TPC) for the directional detection of a source of spontaneous fission neutrons, capitalizing on the relative motion to build algorithms for rapidly locating the source of neutrons. A triple mesh avalanche setup is studied to understand the limitations for achieving higher single electron gain. In addition to boosting the gain, an imaging system that uses the light amplification by means of a micro-channel plate is also investigated, with a new approach to the data acquisition algorithms.

New algorithms for data analysis were coupled with new techniques for event-by-event data handling. These were tested using data collected with an AmBe fast neutron source and compared to simulated data. Using the measured fast neutron background and estimates of the measurement uncertainties from stationary data runs, simulations involving relative motion between source and detector show promising results for this technology.

With a one-person portable detector, multiple people can carry detectors that are wirelessly linked to each other, building a combined radiation field map and reducing the time to locating a source through a shared probabilistic model. A portable, directional fast neutron detector will aid in International Atomic Energy Agency (IAEA) inspections, portal security monitoring, emergency response teams, and military search operations.

Thesis Supervisor: Areg Danagoulian
Title: Associate Professor of Nuclear Science and Engineering

Thesis Reader: Richard C. Lanza
Title: Senior Research Scientist, Nuclear Science and Engineering

Acknowledgments

The Creator for giving us the freedom think, dream, and work towards a better society.

My committee, Professors Danagoulian, Lanza, Fisher, and Horn - Thank you for your support, patience and empathy.

Members of the Dark Matter Time Projection Chamber (DMTPC) - I continue to stand on the shoulders of the brilliant people of DMTPC. Thank you for teaching me from 2011-2013 and for thoroughly documenting all of your work.

Members of the Laboratory of Nuclear Physics (LANPh) - For your help, inspiration, and support over the past three years.

My office mates and classmates, Ethan, Jake, and Peter - Thank you for spending the time to patiently explain the maths to an old guy like me.

Physics, Astronautics, and Nuclear Engineering (PANE) department at West Point - Thank you for the opportunity, the support through the years, and for giving my family and me a home.

The Defense Thread Reduction Agency (DTRA) through the action arm of the Nuclear Science and Engineering Research Center (NSERC) at West Point - Thank you for your support and funding for this project.

Friends, neighbors at HAFB, and classmates - Thank you for being a sounding board, an example of awesome, and a beacon of hope.

The Lawrence family - For the (literally) 55 Zoom calls on Monday nights since the pandemic started. I need those one hour breaks of laughter in my week more than you could ever imagine.

Mom and Dad, Erin and Derek, Tommy - Thank you for the 4×10^1 years of support in my crazy career choices, no matter how dangerous, difficult, or frustrating.

My kiddos, William and Annelise - You two are my strength and my hope for the future of this world. Thank you for letting me be tired, stressed, and distracted at the dinner table every night. Now let's go camping!

My lovely wife, Vanessa - You are the solution to my equation. Thank you for pushing me when I needed pushing and hugging me when I needed hugging. I could never imagine a more perfect human being to navigate this crazy life with.

Contents

1 Introduction **17**

1.1 The Spread of Nuclear Power 17

1.2 Proliferation Pathways 19

1.3 Radiation Detection 21

1.3.1 Radiation Signatures from Nuclear Material 23

1.3.2 Methods of Radiation Detection for Nuclear Security 24

1.3.3 Portable Radiation Detectors 25

1.4 The Case for Detecting Fast Neutrons 26

1.5 Additional Fast Neutron Signatures 27

1.6 The Portable Time Projection Chamber 27

1.7 Conclusion 28

2 Detector Principles and Background **29**

2.1 Time Projection Chambers 30

2.1.1 A New Twist for TPCs 30

2.1.2 Optical TPC Fundamentals 31

2.2 Target Gas Selection 33

2.2.1 Elastic Scattering with Helium 35

2.2.2 Amplification Plane Direction Uncertainty 36

2.3 Camera Signal to Noise 39

2.3.1 Initial Recoil Electron Linear Density 39

2.3.2 Electron Drift 40

2.3.3 Avalanche 43

2.3.4 Penning Transfer Rate 44

2.3.5 Relative Reaction Rate 46

2.3.6 Solid Angle Losses 47

2.3.7 Camera Noise 50

2.4 Time Component 51
2.5 Detector Principles Conclusion 51

3 Detector Operation, Data Acquisition and Data Analysis Algorithms 53
3.1 Introduction 53
3.2 Detector Operation 54
3.3 Data Acquisition 55
3.4 Image Processing 56
3.4.1 Dark Frame Images for CCD Data Runs 56
3.4.2 Track Brightening 57
3.4.3 Determining Track Bounds 58
3.4.4 Track Analysis 60
3.5 Digital Waveform Analysis 62
3.5.1 CSP Waveform Analysis 62
3.5.2 PMT Waveform Analysis 63
3.6 Combining All Data Streams 65
3.7 The Photonis Cricket™Image Intensifier 69
3.7.1 Image Intensifier Fundamentals 69
3.7.2 Measuring the Cricket Noise 71
3.7.3 A New DAQ 71
3.8 Data Analysis Conclusion 74

4 Investigations on Gain Improvements Using a Triple Mesh Avalanche 75
4.1 Introduction 75
4.2 Background 75
4.2.1 Electron Gain through Avalanche 76
4.3 Limitations to Gain by Electron Avalanche 78
4.3.1 Streamer Formation and Breakdown 78
4.3.2 Manufacturing Flaws and Corona Discharge 80
4.3.3 Mesh Transparency 80
4.4 Simulations in Garfield++ 81
4.5 Experimental Materials and Methods 84
4.6 Experimental Results and Discussion 87
4.6.1 Limitations and Stability 88
4.7 Gain Improvements Conclusion 89

5 Detector Background Studies **91**
5.1 Gamma Ray Rejection . . . 91
5.2 Alpha Sources in Construction Material . . . 92
5.3 Direct Cosmic and "Ship Effect" Neutrons . . . 94
5.3.1 Direct Cosmic Neutrons . . . 94
5.3.2 Ship Effect Neutrons . . . 95
5.4 Experimental Methods . . . 96
5.5 Cosmic Data Results and Analysis . . . 97
5.6 Detector Background Conclusion . . . 101

6 Stationary AmBe Source Results **103**
6.1 Experimental Methods . . . 103
6.1.1 Neutron Source . . . 104
6.1.2 Detector and Laboratory Environment . . . 104
6.2 Experimental Results . . . 106
6.2.1 Reaction Rate and Intrinsic Efficiency . . . 106
6.2.2 Measured Energy Spectrum . . . 111
6.2.3 Direction to Neutron Source . . . 111
6.3 Discussion . . . 114
6.4 Minimum Expected Capabilities . . . 115
6.5 Conclusion . . . 116

7 Dynamic Probabilistic Back Projection **117**
7.1 Introduction . . . 117
7.2 Inverted Geometry Tomography . . . 117
7.3 Probabilistic Back Projection . . . 119
7.4 Response Function . . . 123
7.5 Experimental Setup . . . 124
7.6 Experimental Results . . . 127
7.7 Discussion of Results . . . 131
7.8 Conclusion . . . 132

8 Conclusion **133**
8.1 Operating at Higher Pressures . . . 134
8.2 Image Signal to Noise and Z-Position Reconstruction . . . 135
8.3 Adding Sensitivity to Thermal Neutrons . . . 136
8.4 Conclusion . . . 136

A Equipment and Source Calibrations **137**
A.1 Calibration Source 137
A.2 Work Function 138
A.3 Charge Sensitive Preamplifier (CSP) Calibration 141
A.4 Calibration of the Ludlow 3.5" Photomultiplier Tube (PMT) 142

B Calculating Reaction Rates **145**
B.1 Cosmic Neutron Energy Spectrum 145

List of Figures

2-1 A cut-away view of the Time Projection Chamber (TPC). 32

2-2 ^{4}He total interaction cross section superimposed with the Watts fission spectrum. 34

2-3 The probability distribution of neutron recoil angle as a function of incident neutron energy. 37

2-4 The results of SRIM simulations using 90% ^{4}He and 10% CF_4, where the linear stopping power has been converted into linear electron density and plotted versus position along the track. 41

2-5 An image of a simulated electron avalanche with the simulation package Garfield++. 44

2-6 Electron-neutral cross sections for reactions that produce or remove electrons from the avalanche. 46

2-7 A comparison between the scintillation spectrum of CF_4 versus the quantum efficiency for the two systems used in this course of research, the Alta U6 Scientific CCD camera and the Cricket Image Intensifier. 48

2-8 The volume integral dimensions to integrate all photons produced within a single pixel mapped to the avalanche plane. 50

3-1 This diagram depicts every connection to the detector chamber, denoted by the thick black line. 54

3-2 An example of the average pixel-to-pixel noise across 100 dark images taken before the start of a run. 58

3-3 This figure depicts the before and after images using the track brightening method. 59

3-4 A cartoon depiction using a simulated track image, showing the algorithm to determine the track bounds as the pixel values are readout from left to right in a row-by-row basis. 60

3-5 The difference between short and long drift distances in the total energy within a track image compared with the energy reported by the CSP or PMT. 61
3-6 Depiction of solid angle differences between the center of the anode versus the outer edges of the anode. 66
3-7 Track examples showing the spatial variation of a track computed by the location of the track within the image. 67
3-8 The energy reported by the calibrated CSP versus the calibrated PMT. 68
3-9 Cricket and Finger Lakes Instrument CCD Noise Profile. 72
3-10 Chart depicting the re-imagined data acquisition algorithms. 73

4-1 Track diffusion as a function of drift distance and electric field strength. 77
4-2 Dipole created between drifting electrons in the electron avalanche and the quasi-stationary counter-drifting ions. 79
4-3 The linear density of electron impact ionization as a function of depth into the avalanche region. 83
4-4 The lateral ion point-of-creation distribution compared between a two mesh avalanche setup and a triple mesh setup. 84
4-5 A miniature version of the full scale field cage to test the triple mesh configuration and compare with the two mesh setup. 85
4-6 Gain curve constructed from two different two-mesh setups to compare the limiting gain value between different avalanche distances. 87
4-7 A comparison of double versus triple mesh setups across several different run parameters. 88

5-1 Possible source locations for alpha background from construction material that are currently incapable of being rejected as background events. 93
5-2 The differential cosmic neutron energy flux 95
5-3 A depiction of the laboratory layout during the cosmic data run. . . . 97
5-4 A comparison of the measured alpha recoil spectrum versus the simulated direct, cosmic-shower differential alpha recoil spectrum. 98
5-5 A comparison of the total range measured by the data analysis algorithms versus energy deposited across the 20-hour cosmic data run. . 99
5-6 Simulated versus measured results for angular double differential spectrum of alpha recoil events for the cosmic-generated background as a function of azimuthal angle and polar angle. 100

5-7 Simulated versus measured results for angular differential spectrum of alpha recoil events for the cosmic-generated background as a function of polar angle. 100

6-1 A depiction of the experimental setup during the stationary AmBe source runs with the Alta Scientific CCD camera. 105
6-2 Reduction in intrinsic efficiency due to dead spots, resistor chain, and imaging volume. 108
6-3 A snapshot of 100 simulated events. 109
6-4 A comparison between the detected and simulated alpha recoil energy spectrum. 110
6-5 The neutron energy spectrum as calculated by unfolding the data from the Troxler source data. 112
6-6 The predicted source direction using data from measurements involving the Troxler gauge source and the Alta U6 Scientific CCD camera. . . 113

7-1 An example of a blocking mask used in typical gamma ray coded apertures for inverted geometry straight line tomography, reproduced from. 119
7-2 The double differential distribution function of alpha recoil events when a flux of fission spectrum neutrons is incident on the detector. 121
7-3 A diagram depicting the manner of computing the implied neutron direction, implied alpha scattering angle, and the implied probability of a neutron source located in that direction. 122
7-4 The response function for detecting the direction from a stationary detector. 124
7-5 A visual rendering of the moving source and neutrons emitted in a portion of the solid angle that includes the detector. 126
7-6 The three dimensional weighting from a single pass of a portable TPC at a closest approach of two meters from 1kg of WGPu. 128
7-7 A comparison of the signal-to-noise in the weighting function compared between simulated background signals and simulated background with 1 kg WGPu. 128
7-8 The distribution of the predicted source location after 1,000 single passes at a minimum approach of 2m and a walking pace of 1 mph. . 130

8-1 A future test to confirm the uncertainty in the Z-position reconstruction.135

A-1 The energy spectrum of the Am-241 0.9 μCi source. 138

A-2 The measurement of the work function using simulations fit to data by a least squares method. 140
A-3 An example of a linear fit to determine the gain for the Charge Sensitive Preamplifier, the Cremat 110 CSP. 142

B-1 The elastic scattering, angular, differential distribution for a flat neutron energy spectrum from 10keV to 20MeV, built from data downloaded from the Evaluated Neutron Data File [1]. 146
B-2 The expected distribution of alpha energy given a cosmic neutron energy flux from Figure 5-2. 147

List of Tables

2.1 The angular uncertainty for an alpha track of given energy. 39

6.1 The uncertainty from each measured quantity in the primary AmBe source data run. 114

Chapter 1

Introduction

Nuclear power is rapidly moving back into the spotlight as a proven technology that has powered 20% of the United States grid for the past 50 years with no carbon by-product. With modern reactor designs that are walk-away safe, capable of load following, and include designs for pairing power production with renewable energy sources, these new reactors are ready to take-on the burden of transitioning to a carbon-free electric grid [2–4]. With the pending second nuclear renaissance, the time is ripe to update the fleet of radiation detectors for non-proliferation, counter-proliferation, and disaster response. The fleet of gamma detectors have witnessed an impressive growth of detector technology, with designs including directional and ultra-compact detectors capable of being hand carried or flown on small drones [5, 6]. The closest neighbor to these designs for neutron detection are directional, field-deployable, but not necessarily mobile detectors [7, 8]. A backpack portable, directional neutron detector produces a significant improvement in locating a source of fast neutrons. With the boom in growth for nuclear power on the horizon, a mobile, directional fast neutron detector will help stem the synchronously growing threat of nuclear material smuggling and rogue nuclear weapons development programs.

1.1 The Spread of Nuclear Power

From the very onset of nuclear power for civilian power production, nuclear states have sought to introduce nuclear power into developing nations as a source of reliable power. The first commercial nuclear reactor in the United States did not start providing power to the grid until after President Eisenhower was already pushing nuclear power to developing nations [9]. Referred to as Atoms for Peace, nuclear reactors were

constructed around the world to bring clean, reliable power for peaceful purposes [10]. This program was closely followed by an international effort to monitor the safe uses of nuclear power while preventing the proliferation of nuclear weapons [11].

The International Atomic Energy Agency was created in the wake of the Atoms for Peace efforts as the action arm of the international effort to monitor global nuclear power. After more than a decade, the agency developed a framework for nations' to disclose the safe use of nuclear power and nuclear materials through a program called "Safeguards" [12]. Over the decades, these Safeguards came to include a collection of material accountability protocols and reporting procedures for host nations using the latest fleet of radiation detectors [13]. On a parallel timeline, the knowledge of nuclear weapons remained a close held secret to only a handful of nations, while most other nations avoided the hassle of building a nuclear weapons program. Over the same time frame, the international community came together to declare a Treaty on the Non-Proliferation of Nuclear Weapons (NPT) [14]. This also fell into the realm of oversight of the IAEA, where the Safeguards program would become the primary means of managing the NPT.

In parallel to the NPT, concern grew over the size of the US and USSR nuclear arsenal and the dual policies of Mutually Assured Destruction. As such, nuclear test ban treaties and nuclear disarmament discussions began to surface in the 70s and 80s. These discussions displayed the shared concern for nuclear warfare but also the lack of trust between the Union of Soviet Socialist Republics and the United States. A significant turn in the tide of the arms race occurred when Mikhail Gorbachev was elected as the General Secretary. President Reagan and Secretary Gorbachev had a "positive personal relationship", changing the tide of negotiations between the two nuclear mega-states [15]. However, even with the positive relationship, the two knew that every action would require some level of verification, with the famous phrase from President Ronald Reagan, originating from a Russian proverb, "Trust but verify" [15]. In the initial stages, nuclear armed nations were satisfied with disarming delivery vehicles, with verification efforts focused on aerial imagery of dismantled rockets and bomber aircraft [16]. However, after exhausting this strategy through verification of dismantling a variety of delivery vehicles, the last few decades have witnessed a renewed effort of the international community to call for actual munitions disarmament. The latest efforts in disarmament are focusing on zero knowledge protocols, where munitions are verified to be fully functional nuclear warheads immediately prior to disarmament, without any knowledge of the warhead being disclosed to international inspectors [17].

One of the main themes across the spectrum of nuclear security are the availability and capability of radiation detection equipment. The international community of nuclear scientists have established and operate radiation portal monitors, with the goal of detecting the illicit flow of nuclear material across international borders [18]. The IAEA Safeguards program conducts materials assay, where all nuclear material is accounted for throughout the entire life cycle of nuclear fuel [13]. Zero knowledge verification efforts rely on the entire range of legacy to ultra modern accelerator beams and radiation detection equipment [19]. All of these areas stand to benefit from new technology that is one person portable but provides sensitivity to fast neutrons across the 4π solid angle.

1.2 Proliferation Pathways

Prior to improving the fleet of radiation detection equipment tailored to nuclear security, one must fully understand the possible routes for nuclear weapons technology proliferation. From an understanding of the proliferation pathways, radiation technology can be developed and modernized to fill in gaps between human intelligence, signals intelligence, and current radiation detection capabilities. The two commonly accepted paths available to a nation developing a nuclear weapons program are the development of domestic enrichment capabilities that can be used to produce High Enriched Uranium (HEU) or the development of domestic nuclear power plants that can be altered to produce Weapons Grade Plutonium (WGPu). A third route for nuclear weapons proliferation is available to rogue states as well as terrorist organizations through a nuclear warhead theft, where the device is already assembled. The latter pathway becomes a more realistic threat as nuclear weapons technology transitions to the hands of unstable regimes.

Originally thought to be protected by the technological difficulty, the enrichment process has become accessible to any nation with a reasonable budget dedicated to weapons development. Iran presents the ideal case study, where enrichment capabilities were designed in house with the help of a global nuclear black market led by A.Q. Khan [20]. Iran started from Khan's smuggled information as a foundation and built domestic enrichment institutional knowledge, resulting in the capability of assembling a uranium-based weapon whenever the nation decides [21]. Regardless of declared intent, once the capability to enrich uranium is developed, any future leader can switch the low-enrichment commercial plant to a military-use program, where the commercial enrichment is already three-quarters of the enrichment effort required

for weapons grade [22]. However, uranium-based weapons have a theoretical smallest size limit of 12-kg of uranium, with additional material for tampers, explosives, and sub-critical mechanism. As such, rogue nations with terrorist mindsets and limited missile delivery technologies will likely seek the smallest sized weapon possible: a plutonium-based weapon.

The second approach to proliferation requires some form of a nuclear reactor to irradiate Uranium-238, producing the fissile isotope Plutonium-239. In this scenario, rather than domestic enrichment capabilities, the rogue nation requires access to a nuclear reactor. As uranium is irradiated, remaining in the neutron field for extended periods of time produces a higher concentration of Plutonium-240, reducing the capability of the material in a weaponized form. In a modernized society where nuclear power is used globally, a nuclear fuel program that leases fuel to the countries alleviates the stress of managing key components of the fuel cycle [23]. In this scenario, the nation operates and maintains the reactor while "fuel-cycle" nations maintain the enrichment and reprocessing facilities, shipping only the fuel. A "reactor" state that turns rogue will need to develop domestic glove-box processing facilities to convert irradiated reactor fuel into plutonium metal. However, true Weapons Grade Plutonium, or plutonium metal at isotopic levels of 93% Pu-239 or higher, may not be necessary to have a similar effect for terrorist activities. Previous research has shown lower levels of Pu-239 isotopic percentage have explosive properties and as such are still dangerous when assembled into a crude weapon [24].

The third pathway to proliferation becomes more likely when nuclear power programs are sought by unstable regimes, opening the door for terrorist organizations to acquire a crude or highly developed nuclear weapon in the vacuum of security within the unstable regime. In this scenario, the method of weapon deployment is significantly different from state-sponsored use, as a terrorist organization will not have extended range airborne delivery capabilities. This approach differs from the first two proliferation pathways discussed above from weapon assembly to weapon deployment. The organization would have to first acquire the material, smuggle the material to a safe zone to assemble into a crude weapon, and then smuggle the weapon across borders to detonate [25]. Any of these border crossings are opportunities to detect radiation signatures.

1.3 Radiation Detection

On a broader scope than nuclear security, radiation detection in general has fully converged with every corner of modern society, from medical imaging and cancer treatment monitoring to cargo security and nuclear safeguards, to name a few. In recent years, radiation detection equipment has been shifting towards more portable equipment that can be carried by one person and more capable than a simple count registered for each radiation interaction. Portable equipment provides a tremendous capability for first responders, safeguards inspectors, and military personnel attempting to locate sources of radiation for various goals, while additional information offers capabilities of suppressing background radiation signatures improving signal to noise. Further, one person portable equipment is rapidly replaced when malfunctions occur at stationary radiation detection facilities, such as portal monitors and container inspection stations.

Radiation detection rests on the foundation of turning an ionizing interaction into a recorded signature. The ionization can result from direct interactions or indirect. For example, an alpha or beta particle emitted in a radioisotope decay within a gaseous detector directly ionizes the gas. However, a neutron will cause ionization in a similar detector indirectly through elastic scattering from a target nucleus, which in turn ionizes the gas. The recorded signature ranges from a visible track of tiny bubbles in a cloud chamber to fully reconstructed events with multiple detection mediums, multiple digitizers, and multiple computers [26]. As discussed in the next section, nuclear security is typically focused on detecting x-rays, gamma rays, and neutrons. Gamma rays are primarily detected through interactions with electrons in the target medium, where the reaction is split between an ejected electron from the photoelectric effect, a scattered electron through Compton scattering, or an electron-positron pair created in the vicinity of the strong electromagnetic field near the nucleus [27]. The ratio between these three reactions vary depending on the energy of the gamma and the atomic number,Z, of the isotope.

Neutron signatures can be detected through a variety of interactions as well. Fast neutrons are overwhelmingly detected through elastic scattering. The typical fast neutron signature for nuclear security is at too low of an energy range for inelastic reactions and too fast for resonance reactions. As such, low-Z material offers a better energy transfer to the target medium, improving the energy threshold for detection. Thermal and epithermal neutrons, on the other hand, have energies up to approximately the 100s of electron-Volts and are best detected through nuclear reactions.

These reactions have historically been the ^{3}He(n,p)T reaction, where the significantly high cross section of ^{3}He to thermal neutrons give a ^{3}He detector nearly 100% intrinsic efficiency for neutrons in that energy range. However, these detectors must moderate first to detect fast neutrons, reducing the intrinsic efficiency considerably, and high energy gamma interactions can create a noticeable background. Further, the act of moderating the fast neutron signal destroys valuable directional information.

Radiation detectors provide a variety of capabilities to professionals across multiple fields in modern society. At a minimum, a detector will provide a count for each interaction, which can readily be paired with time for additional information. As detectors grow in complexity, they are capable of providing the energy of the interaction and details about the direction of the original particle. This information, paired with the rate and the time, can be analyzed to determine the likelihood of a radiation source being present versus a purely background signal. As such, inspectors use these more advanced detectors to check for radiation signatures where there should be none, as in cargo scanning, or radiation signatures that match what is reported, as in IAEA Safeguards material assay.

In the case of first responders, if a radioisotope deployment mechanism commonly referred to as a "dirty" bomb detonates and deploys a variety of radioisotopes, quickly finding and removing the sources is paramount to the local population. Similarly, technicians continue to scan the contaminated areas near the Fukushima power plants almost a decade after the accident. The technicians need small, portable equipment mounted to drones to image remote areas not large enough for helicopter operations [28]. A backpack-scale or smaller detector is critical in this scenario. For safeguards inspectors, confirming the absence of additional, undeclared sources should be an integral part of the inspection process. Being able to hand-carry the detector into and around the facility is vital to be considered for wide spread use for safeguards inspectors. And for military personnel, many operational scenarios in tactical nuclear warfare could play out requiring the need for mapping the presence of dangerous levels of radiation, as well as searching for and seizing unused weapons. All of these scenarios encourage the use of radiation detection equipment that is one person portable.

Gamma ray detectors have answered the call for portable detectors. Modern and portable gamma ray detectors range from wrist watch scale detectors up to Compton cameras built into Unmanned Aerial Vehicles (UAVs) [5]. These portable gamma ray detectors typically focus on a specific energy range and provide some additional feature to counter the small size. In other words, the UAV-born Compton camera manages to suppress background gammas through spectral analysis as well as

direction [28]. For modern neutron detectors, if the detector is one person portable, the detector provides minimal information. In fact, in many cases, modern, portable neutron detectors have significant signal overlap with gamma signatures, requiring additional data collection until the two signals can be separated. These detectors provide only a count rate for neutrons, as the energy information is lost through the continuous range of possibilities in neutron elastic scattering. It is in this space that this research seeks to provide steps forward: a portable neutron detector that provides a powerful stream of data for neutrons with minimal overlap with other signatures.

1.3.1 Radiation Signatures from Nuclear Material

In order to address the concern for nuclear proliferation, many signals have to converge and work together, with human intelligence feeding into signals intelligence, which should include an overlapping network of radiation detection equipment in as many locations as possible. The radiation signature from special nuclear material covers essentially every terrestrial type of radiation: alpha particles, high energy electrons and positrons, x-rays, gamma rays, neutrinos, and neutrons. However, in a realistic sense, the only radiation signature with enough penetrating power to be considered for illicit source detection and location are higher energy gamma rays, neutrinos, and fast neutrons. Neutrinos have a low interaction probability and a very high background from solar radiation. As such, neutrinos are not feasible for detecting illicit material in a portable package. Gamma rays and fast neutrons become the two primary means for detecting illicit nuclear material.

The gamma signature from Highly Enriched Uranium (HEU) presents a handful of higher energy gamma rays capable of penetrating moderate amounts of shielding, including a 185keV that is less penetrating but has a very high activity and a 1.001 MeV gamma that has a lower activity but is much more penetrating [25]. Weapons Grade Plutonium (WGPu) also has the 1.001 MeV gamma and a few low activity signatures at 662 keV, 723 keV, and 769 keV [25]. HEU has effectively no signature of fast neutrons, but WGPu has a considerable signature of fast neutrons originating predominantly from the spontaneous fission of the isotope Pu-240 [25]. Further, these neutrons cause (n,2n) reactions in tampers, which results in a detectable level of neutron activity, conservatively 10^5 neutrons per second per kilogram, from a fully assembled plutonium warhead [29].

1.3.2 Methods of Radiation Detection for Nuclear Security

The field of radiation detection for nuclear security pairs the two concepts of passively detecting radiation signatures or interrogating the cargo to look for specific results within the cargo that will differentiate between normal cargo and illicit nuclear material. The majority of passive monitors are used where people are passing through an entry point, while active systems are only employed for pure cargo passage points. The passenger portals can be vehicle entry points or pedestrian traffic check points and are monitored by laboratory scientists around the world [18]. These check points typically use neutron count rate as the primary means of neutron detection and count rate plus spectral analysis for gamma ray detection. However, the passage points inherently have a relative motion between possible source smuggling locations and detector array, where a directional system could improve the false-negative rate considerably. The inspectors for IAEA Safeguards also rely on a variety of passive detection equipment in order to accomplish material assay in safeguards inspections.

The large active inspection sites are commonly located at cargo container processing facilities at major ports, where a multi-million dollar array of detectors and an interrogation radiation beam can sit stationary while containers ride through the beam on an automated track [30]. The active beam interrogates the object, producing radiographic images from the moderation of the beam, as well as information from the induced reactions in the cargo [31, 32]. Again, in this scenario, relative motion creates an opportunity to capitalize on directional detectors in addition to the time coincidence for the active beam time, improving the false-negative rate by locating sources of illicit nuclear material in a faster time.

Finally, a variety of radiation detection scenarios arise where the operator must carry the detection equipment to scan in non-standard locations or search for undisclosed radiation sources. These scenarios include IAEA Safeguards inspectors, military personnel searching for signs of illicit nuclear material, and first responders. In each of these scenarios, the suite of detectors should search for all penetrating radiation, gamma rays and fast neutrons, and should be capable of being hand carried into the inspection site. Neither of the three situations can guarantee vehicle passage to all locations of concern. As such, one person portable radiation detectors are highly preferable in these three illicit nuclear material search scenarios.

1.3.3 Portable Radiation Detectors

The need for radiation detection spans many fields with a variety of necessary capabilities. The field of nuclear security can learn new capabilities from the medical imaging field and vice versa. While the medical field commonly needs position sensitive devices to provide high resolution images, the field of nuclear security on a fundamental level needs the capability to detect a source of illicit nuclear material with an incredibly high success rate. The success rate comes with a two-fold requirement: the detector should have a very low false-positive probability and a high detection probability. While the medical and nuclear security fields have significantly different problems to solve, one field can learn from the other in terms of detecting a localized source of radiation. The cases of Computed Tomography (CT) and Positron Emission Tomography (PET) scans have shown the power of localizing a source of radiation through line integrals and position sensitive detectors. This problem can be inverted for a stationary source and a moving detector, where instead of a position-sensitive detector, now a direction-sensitive detector is used [33].

Many studies have focused on the capabilities of this style of detector with direction-sensitive gamma ray detectors through the use of coded apertures and Compton cameras, but very few studies have created analogues with neutron detection. In the case of a direction-sensitive neutron detectors, fast neutrons are the logical choice, as thermal neutrons have lost any directional information during moderation. This creates a difficult problem to solve, as detecting fast neutrons becomes a much more challenging problem than detecting gamma rays. Due to the penetrating nature of neutrons coupled with the nature of neutrons to primarily interact with low-Z material, and hence lower density, most fast neutron detectors have low intrinsic efficiencies. Further, any variety of a coded aperture immediately imposes size constraints in order for the blocking pixels to be large enough to block neutrons, requiring the detector be scaled to the size of vehicles [34] [8]. Other directional variants have shown successful results using spinning detectors that unfold the direction through a time-encoded aperture [35]. Again, however, the coded apertures and time-encoded imagers are more closely related to field-deployable detectors, as creating relative motion between a scanning area and detectors that weigh several hundred pounds in unrealistic.

1.4 The Case for Detecting Fast Neutrons

Plutonium is commonly accepted as the most logical route to a "suitcase" nuclear weapon that a rogue nation or a terrorist cell would attempt to smuggle into the United States. The minimum weight of Weapons Grade Plutonium required for a reflected core in a weapon is hypothetically 4kg, with an outer radius of the entire weapon assembly of 21 cm [29]. This design is one of the most menacing threats to the modern world, as this small weapon would wreak havoc on our way of life in a few milliseconds. While similar uranium weapons are feasible, albeit a slightly larger size than a plutonium weapon, the signature is almost entirely gamma rays with a very low activity of fast neutrons. As such, any thorough passive detection system must look for both fast neutrons and the handful of high energy gamma rays from HEU.

Fast neutrons are higher energy neutrons with energies typically above 100 keV. For the case of spontaneous fission, the average neutron energy is approximately 2 MeV with a tail that extends above 10 MeV. Many isotopes are capable of spontaneous fission (SF), but few isotopes have a high activity of SF. Plutonium-240 has a rate of SF at 72,000 Bq s^{-1} kg^{-1} [25]. The fast neutron signature from WGPu comes from the Pu-240 isotope, which is essentially a contaminant in the production of WGPu. When WGPu is produced, natural or depleted uranium is placed in a reactor for a relatively short time to achieve a low burn-up. The U-238 isotope captures a neutron and undergoes two beta decays to reach Pu-239. The buildup of Pu-239 occurs simultaneously as the Pu-239 either fission or also undergoes neutron capture. As such, a tail of additional plutonium isotopes results, with Pu-240 being the highest concentration [36]. Weapons grade is considered at or above 94% Pu-239, with an overwhelmingly majority of the remainder being Pu-240. Further, for a rogue state or a terrorist organization, achieving anything close to weapons grade could be worthy of assembling into a weapon and detonating, but with a significantly lower concentration of Pu-239 and higher concentration of Pu-240. This being considered, 6% Pu-240 is the more conservative approach in considering the fast neutron signature. Previous studies show that the (n,2n) reactions slightly increases the total activity when surrounded with a tamper and explosives, bumping the total activity from 72,000 to approximately 100,000 neutrons per second per kilogram WGPu. As such, this course of work will focus on detecting a kilogram of WGPu through the 100,000 n/s with a Watts fission spectrum.

1.5 Additional Fast Neutron Signatures

Spontaneous fission is not the only fast neutron signature, however. In general, the fast neutron background arises from cosmic showers through direct interactions as well as neutron spallation, known as "ship effect". This background will be discussed in detail with results of measurements reported in Chapter 5. Further, the rate of ship effect neutrons is low for small objects. If a passive source of fast neutrons are pinned to a specific point during an inspection, the item is likely special nuclear material. If not disclosed beforehand, it is illicit nuclear material. This argument becomes slightly more convoluted for actively interrogated targets, but the principle remains the same: pinpointing a source of fast neutrons is grounds for believing the item is worthy of additional scrutiny.

During active interrogation with gamma rays, photofission becomes an additional signature that can be detected. While photofission is not exclusive to one SNM isotope or another, it is generally exclusive to very high atomic number elements, with a probabilistic shelf that starts around 5 MeV photon energy. Any active interrogation beam that reaches above 5 MeV has an opportunity to also detect neutrons generated during the active beam time windows. This can further reduce the background signal, requiring that neutrons are detected in coincidence with the active beam time window.

1.6 The Portable Time Projection Chamber

While there are many different types of fast neutron detectors, none of the current detectors are one-person portable as well as directional. ^{3}He detectors require an array of moderating material at varying thicknesses to selectively target energy ranges for fast neutron detection. Some organic scintillators are capable of pulse shape discrimination to separate the gamma and neutron signals, but energy and direction information is not gained from each event. As such, being portable does not offer much additional capability.

Time Projection Chamber (TPC) technology is more than four decades old, with as many variations as there are detectors. Essentially, every TPC is a one-of-a-kind detector, where a "Commercial Off the Shelf" version of a TPC is not in existence. However, the fundamentals all remain the same. A radiation interaction leaves a track that provides a three-dimensional reconstruction; two dimensions come from a projection onto a spatial array of readout channels and the third dimension comes from the time required to readout the track. This is discussed in more detail in

Chapter 2. As an inherent capability, TPCs provide target particle recoil energy, recoil direction, time of interaction, and position of interaction. By making this type of detector portable, sources of radiation can be effectively triangulated, comparable to gamma detectors of similar capabilities [6].

1.7 Conclusion

This work seeks to fill the void in portable fast neutron detectors through the use of a one-person portable Time Projection Chamber (TPC). This will be a comparable technology to the handheld, directional gamma ray detectors currently being deployed. In order to transition from a traditional TPC to a one-person portable, the charge readout is pushed onto a digital camera chip directly or through interaction with a Micro Channel Plate (MCP). With the additional step of the MCP, the total gain becomes high enough to image a track with a standard CCD, allowing for lower power applications and moving towards a true portable state. The new setup will allow smaller sizes and lower power requirements enabling a detector that can readily be packaged as a backpack carried into a radiation search to locate and characterize possible hot spots of fast neutrons. This capability offers a step forward in the fields of border security, military operations to locate illicit weapons programs, and International Atomic Energy Agency (IAEA) safeguards inspections.

Chapter 2

Detector Principles and Background

In order to enable a fast neutron detector that is capable of being constructed into a one-person portable package with directional sensitivity, a Time Projection Chamber (TPC) with optical readout through a digital camera offers a possible solution. By the nature of the readout information, TPCs provide directional information that can be analyzed to build probabilistic models of possible source locations in the local environment surrounding the detector. With assumptions about the neutron energy spectrum, the knowledge of the neutron scattering cross section, and the knowledge of the detector position as a function of time, a mobile TPC can offset the expected low intrinsic efficiency through dynamic, probabilistic back projection.

In the design of a detector dedicated specifically to fast neutrons, elastic scattering is dominant. While arguments have been made in the past that adding an additional gas component would aid thermal neutron detection, this work will focus primarily on the construction of a portable detector for fast neutrons [37]. Due to the dominant nature of elastic scattering reactions at higher neutron energies, the smallest possible atomic mass for the target gas will yield the best angular resolution due to recoil kinematics. Further, the target gas must have a negligible electron attachment coefficient, leading primarily to noble gases. As such, helium is a natural choice. However, finding the optimum Penning gas and mixture concentration becomes crucial to transitioning from a lab-scale experiment with power-hungry scientific cameras to a portable, battery-powered system.

This detector has been assembled and operated in multiple separate scenarios prior to this work, both with Electron Multiplying Charge Coupled Device (EMCCD) cameras and scientific CCDs [38–40]. These cameras add a weight on the order of 7 to 10 pounds and consume 100 Watts at the maximum power consumption [41, 42]. This power is primarily dedicated to cooling the chip to achieve low dark current,

described later. While this could be modified into a smaller package, a likely setup would include several batteries and end up with a two-person package, reducing the mobility aspect for dynamic reconstruction. In other words, a detector of this nature would likely be hoisted into position by two people and left to operate in a stationary nature. Whereas, operating with a truly backpack-scale detector, two people moving about with one detector each can significantly reduce the detection time, as discussed in Chapter 7.

2.1 Time Projection Chambers

Time Projection Chambers (TPCs) have been used in particle physics experiments since 1974 when a scientist at Lawrence Berkeley National Laboratory created the concept [43]. TPCs have been used in a wide range of experiments, including "A Large Ion Collider Experiment" (ALICE) looking at collisions happening on the Large Hadron Collider, the Tokai to Kamioka (T2K) experiment looking at neutrino oscillations, and the Dark Matter Time Projection Chamber experiment looking for Dark Matter interactions with the isotope ^{19}F [44–46].

Fundamentally, every TPC operates on the same principles: 1) a radiation interaction creates a track of electron-ion pairs in the target volume, 2) the electrons drift to a readout plane, 3) a readout plane provides a two dimensional projection of the recoil track, and 4) the time profile of the induced charge provides insight into the third component of the recoil track. After calibration and data analysis, each track provides the track direction, the total energy deposited, time of interaction, and position of the interaction. In a first-of-its-kind portable TPC, this information would be coupled to the position of the detector to build a map of possible locations of the radiation source. The uniqueness of each TPC detector comes through the method of readout. Traditionally, detectors used thousands of metal pads each with an individual wire passing through the target gas chamber to be read by a dedicated digitizer. Further, the addition of parallel wires, wire meshes, and Gas Electron Multipliers have all been used to boost the signal before reading out.

2.1.1 A New Twist for TPCs

Decades after the TPC concept was created at Lawrence Berkeley National Laboratory, a new readout method was imagined by switching from charge readout to optical readout with a digital camera [37, 47]. This modern update converted tens

of thousands of electrodes, each with associated wires and charge readout channels, to pixels on a digital camera chip. In an small package, a CCD or a Complementary Metal Oxide Semiconductor (CMOS) chip can pack tens of millions of readout channels capable of being readout in fractions of a second, depending on the type of camera. The critical step is finding a gas that has a high scintillation efficiency, pairs with the target gas as a Penning mixture, and scintillates in a wavelength compatible with the quantum efficiency available in digital camera chips. This modern twist was the first step in realizing the potential for a TPC to become a one-person portable sensor.

2.1.2 Optical TPC Fundamentals

In a TPC with optical readout, the interaction and drift is identical to any other TPC. After a radiation interaction leaves a track of electrons and ions, the drift field forces the electrons to drift towards the readout plane while maintaining the orientation of the track, minus diffusion along the path. Once at the readout plane, the electrons avalanche, leaving a cloud of ions that scintillate, and the digital camera and PMT both capture information about the initial radiation interaction.

The target gas for this particular TPC is helium, with CF_4 as a Penning mixture discussed in the following sections. The field shaping rings are standard copper gaskets placed in a low off-gas acetyl plastic support structure. The setup is enclosed in an 1/8 inch thick aluminum vacuum vessel. This is depicted in Figure 2-1.

The electric field in the drift portion of the detector needs to be strong enough to separate the initial clouds of electron-ion pairs immediately after the nuclear recoil [48]. Further, the field needs to be strong enough to prevent excessive diffusion along the track, as track diffusion will reduce the total light collected per pixel in the digital camera setup. The field shaping rings must keep the electric field uniform throughout the drift volume to prevent excessive warping of the track's original orientation. As such, these field shaping rings maintain a uniform field across a majority of the target volume, giving up approximately the final 1cm in radius to field non-uniformity due to ring spacing [49]. Moving the rings closer together will increase the shielding effect of neutrons entering the detector. Finally, the field shaping rings pose a spark concern depending on the distance from the chamber walls. In trying to minimize the size of the package to produce a one-person portable package, maximizing the ratio of target volume to total volume is critical. As such, future iterations should seek to use thin copper wire with smaller ring spacing to maximize field uniformity, minimize

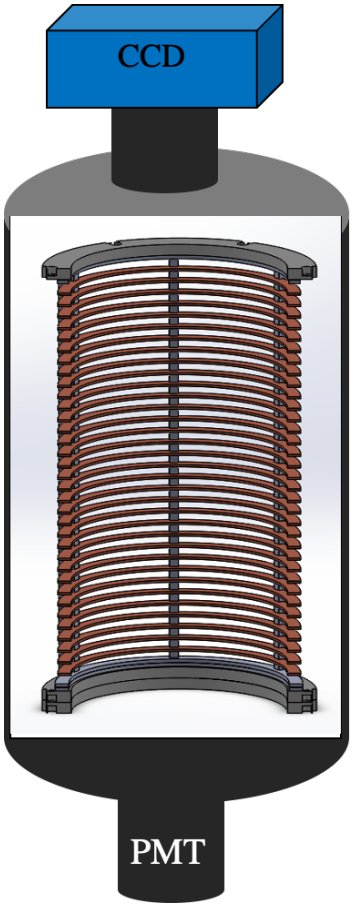

Figure 2-1: A cut-away view of the Time Projection Chamber (TPC). The blue box on top represents the CCD camera looking through a three inch viewport and the cathode mesh. The Alta U6 camera is focused on the anode mesh with an 85mm f/1.2 lens. The 35 copper field shaping rings are held in position by six acetyl ribs affixed to two acetyl rings at the top and bottom of the field cage. The PMT also views the anode mesh through a view-port at the opposite end of the field cage from the CCD. The enclosing structure is an 1/8" aluminum tube, eight inches in outer diameter and 15" long.

excessive shielding of the target gas, and decrease the loss of target volume for field cage ring dimensions.

At the anode-end of the drift field, two meshes are held approximately 500 μm apart creating an electric field strong enough to initiate an electron avalanche. The avalanche is discussed in more detail in Section 2.3.3 and Chapter 4. In the cloud of slow moving ions remaining after the avalanche, a percentage of these ions exist in excited states that decay by emission of a photon. For CF_4 ions, approximately 30% decay by emission of a photon, with approximately half of those occurring in the sensitive range of the CCD camera and PMT [50]. The decay time of a CF_4 ion, when decaying via visible photon (particular for CCD and PMT quantum efficiencies) is approximately 15 ns, fast enough to scintillate before drifting a significant distance [51].

Later in this research, the scientific CCD was swapped out to test and characterise an Image Intensifier coupled to a standard CCD in order to move towards a more compact, less power hungry system. The digital camera collects light for a set exposure time and then reads the image into computer memory for further analysis. As such, the camera only carries coarse information about the time of interaction. The PMT is read through an Alazar ATS860 PCI-card digitizer at 125MHz and triggered just above the noise. Further, if the drift distance can be estimated to within a few centimeters, the time of avalanche coupled with the drift velocity of approximately 0.9 cmμs^{-1}, the time information carried in the PMT can provide accuracy on the order of microseconds [52].

The image analysis, waveform analysis, and track detection algorithms used in this experiment are discussed in Chapter 3. After analysis, each event provides a recoil direction, energy, recoil length, time of interaction, and position within the detector. This information is coupled with detector position and orientation to build a probabilistic model of the surrounding environment for possible neutron source locations, discussed in Chapter 7.

2.2 Target Gas Selection

As discussed earlier, ^{4}He offers an affordable, low mass drift gas that doubles as the target in detecting fast neutrons. As depicted in Figure 2-2 ^{4}He has an elastic scattering cross section that matches closely to the Watts Fission spectrum, of concern when searching for illicit sources of fast neutrons. This also helps further restrict the probabilistic models of possible neutron source locations, discussed in Chapter 7.

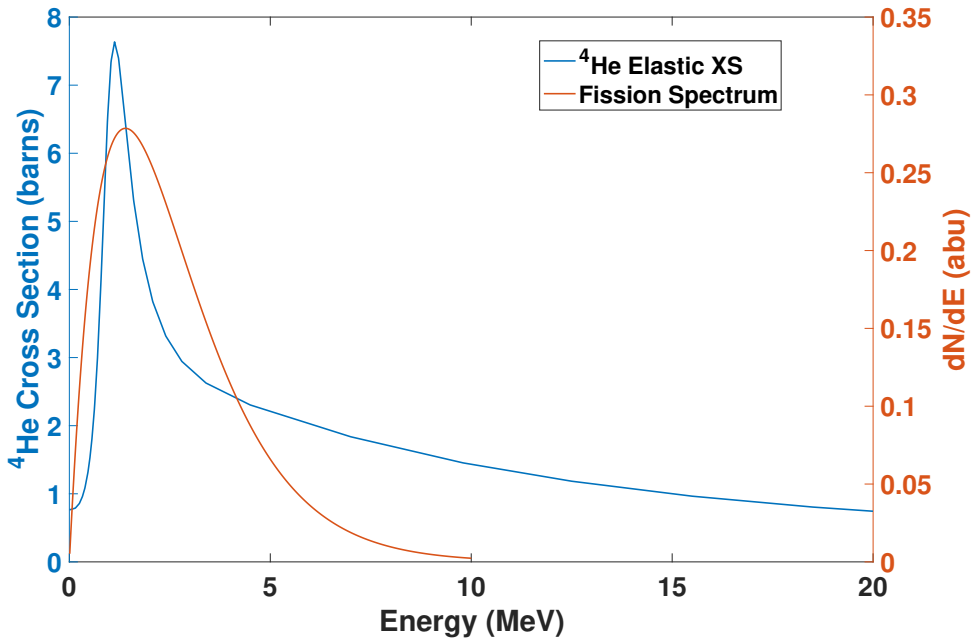

Figure 2-2: ^{4}He total interaction cross section superimposed with the Watts fission spectrum. This figure shows the single, broad resonance for neutron-helium interactions, where elastic scattering is the dominant interaction. Further, the Watts fission spectrum expected for illicit nuclear material is superimposed to show the similarities between the expected source of radiation versus the sensitive energy range of ^{4}He. This produces a flux-averaged cross section of 3.7 barns when searching for fission sources.

In an assumption that the detector is designed to detect specifically illicit nuclear material, the fast neutrons are expected to match closely to the Watts fission spectrum. Paired with the ^{4}He elastic scattering cross section, the flux-averaged cross section is 3.7 barns. Many fast neutron detectors aim for using hydrogen as the primary target (typically part of an organic scintillator), but with an assumption of a fission spectrum, ^{1}H produces a flux-averaged cross section of only 3.1 barns. While hydrogen will not function optimally as a drift gas due to the electron attachment cross section, this further encourages the use of helium to construct fast neutron detectors. Finally, the isotropic nature of elastic scattering between fast neutrons and hydrogen and the 1/E relationship scattering cross section result in a significant portion of the scattered protons occuring below the energy threshold for a detector.

If the detector is operated at 10 atmospheres, a pressure that is readily achievable in a backpack style of detector, the intrinsic efficiency will be on the order of one percent depending on the details of chamber wall material. The optimal material would be a thin metal with a thin layer of carbon-fiber over-wrapped to minimize the thickness while still managing the necessary pressure. At this pressure, the alpha recoil range is still long enough to provide directional information in the imaging system above approximately 100 keV.

2.2.1 Elastic Scattering with Helium

The dominant reaction between fast neutrons and ^{4}He is elastic scattering. In this reaction, the energy is conserved, as depicted in Equation 2.1, momentum is conserved, the center-of-mass velocities remain the same, and only the direction of motion is altered after collision. $T_{n,i}$ and $T_{n,f}$ are the initial neutron energy and $T_{\alpha,f}$ is the final alpha momentum.

$$T_{n,i} = T_{n,f} + T_{\alpha,f} \tag{2.1}$$

Note the neutrons are traveling at a small fraction of a percent of the speed of light, and as such are treated as non-relativistic. Further, the thermal motion of the helium gas is a fraction of a percent of the neutron speed, allowing the assumption that the alpha is initially at rest. The conservation of linear momentum results in Equation 2.2, where $\vec{P}_{n,i}$ and $\vec{P}_{n,f}$ are the initial and final linear momenta of the neutron and the $\vec{P}_{\alpha,f}$ is the final linear momentum of the alpha particle.

$$\vec{P}_{n,i} = \vec{P}_{n,f} + \vec{P}_{\alpha,f} \tag{2.2}$$

Equation 2.2 can be broken into two components, acknowledging the fact that the scattering will always take place in a single plane, requiring any solutions to be distributed 2π around the original neutron direction of propagation.

$$P_{n,i} = P_{n,f}cos(\theta) + P_{\alpha,f}cos(\phi) \tag{2.3}$$

$$0 = P_{n,f}sin(\theta) + P_{\alpha,f}sin(\phi) \tag{2.4}$$

From Equations 2.1, 2.3, and 2.4, the TPC is capable of providing the alpha recoil momentum, leaving the initial and final neutron energies and initial and final neutron directions unknown. However, the alpha recoil energy provides additional probabilistic information about the unknown details. As depicted in Figure 2-3, the lower energy neutrons, 100 keV to 1 MeV, favor back scattering, while neutrons above 1 MeV have a forward bias after elastic scattering. This information can be used to further condition the probabilistic model of neutron source locations. Combining Equations 2.3, and 2.4 to eliminate the final neutron momentum, knowledge of the final alpha momentum and an assumption about the incident neutron energy spectrum (and hence momentum) provides the capability to build a probabilistic model for possible recoil angles.

As a brief example, take a 1MeV incident neutron (the most common neutron energy in a fission spectrum), looking at Figure 2-3, the most likely scenario is a maximum energy transfer (center of mass scattering of $cos\theta = -1$) or minimal energy transfer (center of mass scattering of $cos\theta = 1$), but less likely energies in between. With this wide discrepancy and again, with knowledge of the source spectrum and helium differential cross section, 600 keV alpha particles in the detector are more than likely head on collisions from a 1 MeV neutron rather than a glancing collision from a 100MeV neutron). And low energy alpha recoils are likely glancing collisions from a 1MeV neutron rather than a head-on collision from 100KeV neutron. This is discussed further with results of simulations in Chapter 7.

2.2.2 Amplification Plane Direction Uncertainty

Given a lower intrinsic efficiency, additional information becomes a critical component of radiation detection using this technology. Using a low atomic mass target gas significantly improves the recoil direction uncertainty over heavier target gas options, as the lower mass target results in a higher momentum transfer. As a solution to

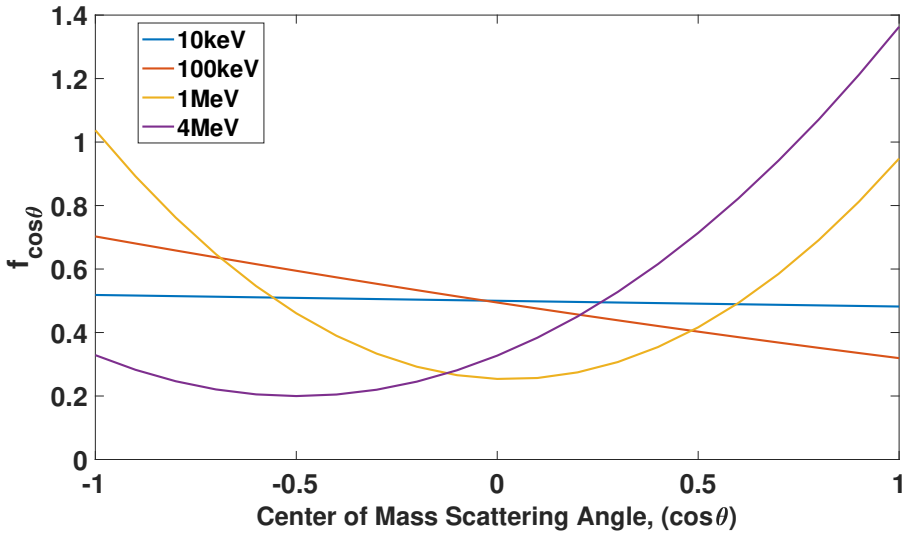

Figure 2-3: The probability distribution of neutron recoil angle as a function of incident neutron energy. This figure depicts the varying dependency of the recoil angle on the incident neutron energy, where higher energy neutrons favor a forward scattering in Center of Mass coordinates. Between 100 keV and 1MeV, a large percentage of neutrons favor back scattering, which favors maximum energy transfer to the alpha, improving angular resolution. This transforms into a forward bias to helium-neutron scattering in laboratory coordinates.

the conservation of energy and conservation of momentum equations from previous sections, Equation 2.5 shows the maximum energy transfer as a function of target gas atomic mass, A. This results in a maximum energy transfer of 64% to the ^{4}He target gas, and only 18% to the next lightest noble gas.

$$E_{\alpha,max} = (1 - \frac{(A-1)^2}{(A+1)^2})E_{n,initial} \tag{2.5}$$

However, the physical processes involved when the recoiling alpha particle slows to thermal speeds introduce uncertainty. While an ion is coming to rest in a gaseous medium, an uncertainty in the original direction is induced, primarily through nuclear scattering in the medium which induces greater deviation from the original recoil direction than electronic interactions. Unfortunately, this angular uncertainty is a difficult item to measure directly. Therefore, simulations were written to produce simulated tracks which were then fed through the same image analysis software from Chapter 3 to determine an estimate of the direction reconstruction uncertainty from initial recoil through track direction reconstruction.

Using Garfield++ and the Stopping Range of Ions in Matter (SRIM) simulation software, tracks were created, accounting for diffusion and an expected gain of $9 * 10^4$. The SRIM tracks were generated at the maximum drift distance of 18cm, assuming a two drift system with a central anode-ground-anode setup similar to [53]. The diffusion coefficients were generated by the Magboltz simulation package and checked against pure helium with data from Pack, et. al. [54,55]. The diffusion in the avalanche was estimated from empirical observations and simulations from lower gain avalanche in Garfield simulations [56]. This imposed an additional Gaussian spread of approximately 250 micrometers, the wire spacing in the mesh. Subsequently, the tracks were pushed through the custom track finding algorithms to determine a direction reconstruction uncertainty. The alpha energy was varied from 50 keV up to 500 keV, with 100 simulated tracks at each energy to give an estimate of angular uncertainty. These results are listed in Table 2.1. Beyond 200 keV, the angular resolution continues to improve to better than 5°.

α Energy	Mean Angle(°)	Error(°)
50 keV	47	10
200 keV	45	8
500 keV	46	5

Table 2.1: The angular uncertainty for an alpha track of given energy. As the energy increases, the deviations from the true direction at the beginning of the track are smaller resulting in a lower uncertainty of the track's true direction. These uncertainties were produced with the Stopping Range of Ions in Matter (SRIM) package within Garfield++ and subsequently passed through the data analysis algorithms discussed in Chapter 3.

2.3 Camera Signal to Noise

The number of photons incident on each pixel must be enough to overcome the pixel-to-pixel read noise at a high enough level that the full track length can be imaged. The number of photons per pixel is a function of the total gain in the detector, the solid angle losses between the amplification plane and the camera lens, and the magnification of the image plane to camera chip. This section will address all of the physics that takes place between an electron entering the avalanche and a pixel registering a signal.

2.3.1 Initial Recoil Electron Linear Density

One of the leading limitations to total gain is the linear density of the electron cloud along the central axis of the recoil track. At higher density, lower gain values are expected due to the breakdown conditions. However, at higher density, one should also expect a higher pixel photon density. The recoil of an alpha particle after a helium-neutron elastic scattering event produces a track of electron-ion pairs. The linear charge density of this track can be described by the Bethe-Bloch formula at the respective energies, as depicted in Equation 2.6, where the high energy corrections have been omitted due to the energy ranges of interest in this work [48]. In this equation, N refers to electron number density of the target gas, E the alpha energy, and $m_e c^2$ the rest mass of the electron. The recoil particle's electric charge, energy, and speed are given by z, E, β and γ, where $\gamma = 1/(1-\beta^2)$. I provides the mean excitation potential of the target medium. The energies considered in this work are treated as non-relativistic, with $\beta_{max} \approx .02$, giving $\gamma \approx 1$.

$$-\frac{dE}{dx} = \frac{2\pi N e^4}{E} z^2 \ln(\frac{4E\gamma^2}{I^2}) \tag{2.6}$$

The electron number density and the mean ionization potential can be written in terms of gas concentration. Treating CF_4 as an ideal gas and using the ideal gas law, the number density is the ratio of the gases partial pressure to temperature and the ideal gas constant. These can be combined to give the mixture number density in terms of the CF_4 concentration, C, as in Equation 2.7. Here, N_A is Avogadro's number, and A_{He} and A_{CF4} are the atomic masses for helium and CF_4 respectively.

$$N_{mixture} = N_A \frac{P_{total}}{RT}[(1-C)A_{He4} + CA_{C12} + 4CA_{F19}] \tag{2.7}$$

The mean excitation energy can be written in terms of the mixture concentration, $I_{mixture} = (1-C)I_{He} + CI_{CF4}$. With $I_{He} \approx 25eV$ and $I_{CF4} \approx 15eV$, $I_{mixture} \approx 25-10c$. Dividing the stopping power by the work function of the gas, an approximation of the linear electron density in the initial recoil track is given by Equation 2.8, where all of the constants (including temperature) were collected into the term Λ.

$$\lambda_{el} \approx \Lambda \frac{1}{\beta^2} P(4 + 84C)\ln(\frac{2m_e c^2 \beta^2}{(25-10C)^2}) \tag{2.8}$$

From Equation 2.8, it is clear that increasing the pressure, P, or increasing the concentration of CF_4, c, will increase the linear electron density. While an increase in linear electron density will improve the pixel photon density, increasing the concentration of CF_4 also offsets the available target volume of ^{4}He and increases the attachment reaction rate discussed in the previous section. Equation 2.6 provides reasonable agreement with data above 100keV and a good depiction of the expected behavior when adjusting the pressure and concentration. Simulating the stopping power with the program Stopping Range of Ions in Matter provides a more accurate picture for behavior at a wider range of energies [57]. From the simulated stopping power, the density of the gas and the work function are used to convert the units to number of electrons per millimeter. An example of this simulated output is provided in 2-4.

2.3.2 Electron Drift

While the previous section provides an accurate characterization of linear electron density in the recoil track as function of gas pressure and mixture concentration, this section will address the behavior of the electron cloud as it drifts through the electric field towards the avalanche region. Immediately after the electron-ion track is created, the particles begin drifting due to the drift electric field. The term "drift" refers to

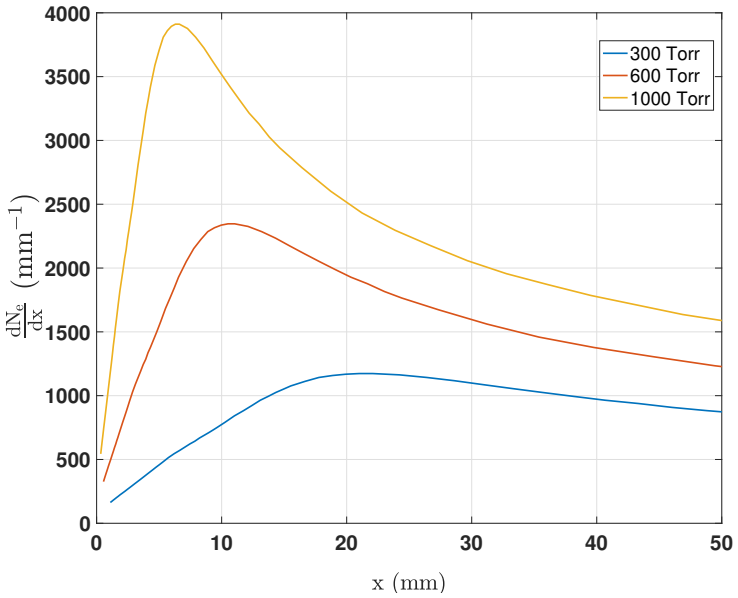

Figure 2-4: The results of SRIM simulations using 90% ^{4}He and 10% CF_4, where the linear stopping power has been converted into linear electron density and plotted versus position along the track. It is clear that increasing the pressure will directly increase the linear electron density and will reduce the total available gain for the detector, discussed in Chapter 4. However, the shortened tracks will brighten in the camera due to the track being focused onto a smaller number of pixels.

a random walk of electrons from collision to collision that favors the direction of the electric field. This can be accurately modeled by electrons following the electric field lines, with the addition of diffusion as a function of drift distance [48].

This drift electric field serves multiple roles. In the absence of this field, the electron-ion track can be treated as a radially symmetric Gaussian distribution of electrons and ions. The drift field needs to be strong enough to quickly separate the spatially overlapping cloud of charges in order to prevent recombination [48]. This typically requires field strengths at a minimum of 100 volts per centimeter, and increases with higher pressures. At the lower field strengths, recombination becomes a contributing factor to total gain. In addition to recombination, the electrons diffuse along the drift field lines (longitudinal) and orthogonal to the drift field lines (transverse), depending on the magnitude of the electric field. Prior experimentation, as well as simulation software such as Magboltz and Bolsig+ provide drift diffusion and electron mobility parameters [54] [58]. Along any appreciable drift distance, the radial distribution of electrons maintains a Gaussian distribution, with the standard deviation being given by the diffusion coefficient, D, and the time of drift, t [48]. This distribution is presented in Equation 2.9, where r represents the radial distance from the original recoil track, and n the number density of electrons in the position distribution of the track [48].

$$n = (\frac{1}{\sqrt{4\pi Dt}})^3 \exp(\frac{-r^2}{4Dt}) \tag{2.9}$$

In reality, Equation 2.9 is altered to account for differences in diffusion along the drift field versus diffusion transverse. However, simulations in Magboltz indicate this is a very minor effect for fields and gas compositions considered in this text. As such, this distribution of electrons in the track are left as depicted in Equation 2.9.

With the combination of the linear electron density along the recoil direction from the previous section, the Gaussian distribution in the radial direction described by the diffusion coefficient gives a complete picture of the electron cloud entering the avalanche region. The maximum gain limitation will be driven by the tracks occurring in the lowest portions of the drift region, resulting in minimal diffusion, other than the initial relaxation of the track. This results in volumetric densities on the same order as the linear densities given in Figure 2-4.

2.3.3 Avalanche

The electron cloud drifts towards the ground and anode meshes, where the meshes are separated by 500 μm, creating a high field region. Once the diffused electron cloud begins to enter the avalanche region, the field strength transitions from a smaller drift field strength to a significantly higher electric field. This field, on the order of 10^5 V/cm creates a condition known as avalanche, where each electron gains enough energy between collisions to ionize on the following collision, on average. Once this magnitude of field is achieved, the entire process can be described by the Townsend coefficient, α and the distance between electrodes, d, which is a ground mesh and an anode mesh in the case of the current work. The total number of electrons produced in the avalanche for every electron entering the region, known as the single electron gain G_{se}, is given by Equation 2.10.

$$G_{se} = \exp(\alpha x) \tag{2.10}$$

The distribution of electrons in the cloud make the avalanche somewhat different from typical gas discharge studies. In traditional studies of gas discharges through electron avalanche, streamers will cause a breakdown at the Meek breakdown condition when $\exp(\alpha d) \approx 10^8$ [59]. The Meek breakdown condition is essentially the gain value that corresponds to an induced field from the local cloud of electrons reaching the magnitude of the external field. In this detector, instead of a single electron, an electron cloud from the original track plays a significant factor when approaching the Meek breakdown theory, but the fundamentals remain the same: when the charge cloud density is high enough to produce an electric field comparable to the external field, streamers will begin to form and cause electric breakdown. This limitation on gain in the avalanche will be largely driven by the peak linear electron density in the recoil track and the total diffusion along the drift direction.

The spatial distribution in the avalanche can be treated as approximately Gaussian due to the diffusion along the drift [59]. The diffusion in the avalanche is greater for a comparable distance than the drift region, pushing the width of the track in the image to the scale of millimeters. Further, the time scales are too short for electrostatic repulsion to play a large factor for the electron cloud. An image of this from a simulation of a lower-gain avalanche is depicted in Figure 2-5. Considering the scale of the avalanche diffusion, the drift field only needs to limit drift diffusion to this same scale for tracks occurring at the far end of the drift field. Any additional electric field strength in the drift field is an unnecessary burden on the electronics,

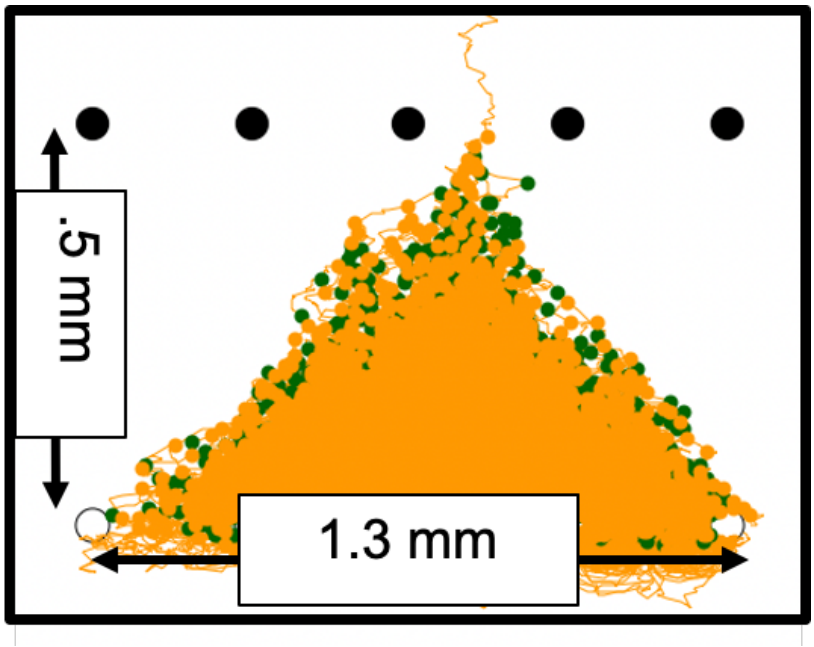

Figure 2-5: An image of a simulated electron avalanche with the simulation package Garfield++. The yellow points represent ionization locations and the green dots in the background are the locations of excitation. The length scales are comparable to larger gain settings.

primarily in forcing unnecessary gaps between the field cage rings and the detector walls.

With the avalanche gain being an exponential relationship with the distance across the avalanche gap, 98% of the ions created occur in the final 30% of the avalanche region. At this point, for an optical read-out setup, the role of the electrons is complete and the detector now relies on the cloud of ions and excited helium atoms in the immediate vicinity of the anode mesh. The relationship between excited helium atoms' decay time, frequency of collision and Penning transfer between helium atoms and ground state CF_4 molecules, and CF_4 attachment rates all contribute to the achievable light output in the avalanche.

2.3.4 Penning Transfer Rate

While helium is the preferable gas as the target medium for reasons discussed in the previous sections, helium has a scintillation light yield that is too low in total light output and primarily scintillates in the ultraviolet region, outside the sensitive region of typical digital cameras and photocathodes for image intensifiers [60]. As such, the use of a second gas with a high probability of scintillating in a spectrum aligned

with digital cameras and photocathode high quantum efficiency region is optimal. Further, choosing a gas with a lower work function introduces the Penning effect, increasing the number or primary electrons in the recoil, further improving statistics. Commonly accepted as one of the best scintillating gases is Carbon Tetrafluoride, or CF_4. Previous measurements have shown that CF_4 scintillates approximately 34% of the time when ionized in the electron avalanche [50, 61]. The dominant ionization mechanism leading to visible photon scintillation is given in Reaction 2.11, requiring an energy of approximately 15eV [62].

$$CF_4 + e^- \rightarrow CF_3^+ + F + e^- + e^- \tag{2.11}$$

An additional reaction that produces CF_4 ions arises when helium atoms are excited through the primary recoil or in the electron avalanche. These excited helium atoms have a minimum excitation energy above the ionization potential of CF_4. This energy transfers from the excited target gas atom to a small concentration of secondary gas mixture, called the Penning effect.

Helium reactions are almost equally split between excitation and ionization in the primary alpha recoil as well as in the electron avalanche, as discussed in the coming chapters. Recent work has shown that the fraction of excited helium atoms transferring energy to CF_4 can be estimated by determining the work function of the gas mixture through Equation 2.12 [63]. In this equation, W_m, W_{He} and W_{CF4} represent the mixture, pure helium gas, and pure CF_4 gas work functions respectively. The ratio of N_{ex} to N_i represents the Penning transfer rate from helium excitations to CF_4 ionizations. The "z" term is calculated from the range of ions in pure helium and the range of ions in pure CF_4, as given in Equation 2.13.

$$\frac{1}{W_m} = \frac{1}{W_{He}} z\Big(1 + \frac{N_{ex}}{N_i}\Big) + \frac{1}{W_{CF4}}(1 - z) \tag{2.12}$$

$$z = \Big(1 + \frac{R_{He}(P_{He})}{R_{CF_4}(P_{CF_4})}\Big)^{-1} \tag{2.13}$$

Appendix A describes how the work function for this gas mixture was measured. The helium and CF_4 work functions were reported in previous experiments, and the range is simulated by the SRIM software suite [57, 63, 64]. Using these formulas to calculate the Penning transfer rate for the typical running conditions in this course of research, 1000 Torr total pressure with a 10% partial pressure of CF_4, the Penning transfer rate from helium excitations to CF_4 ionizations is approximately 86%.

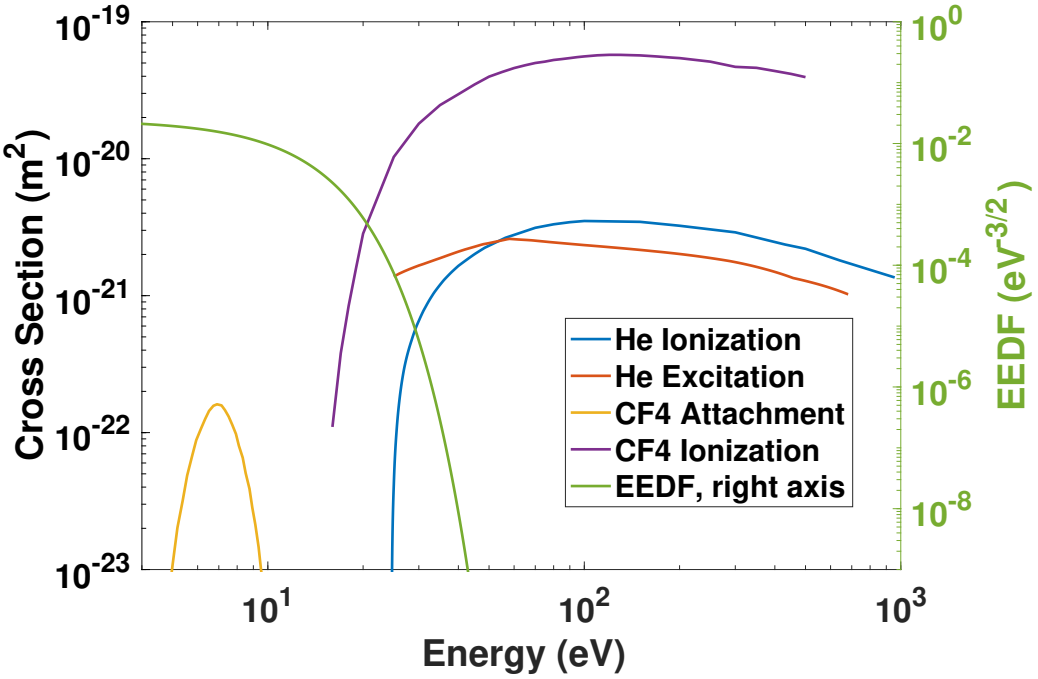

Figure 2-6: Electron-neutral cross sections for reactions that produce or remove electrons from the avalanche. The main helium excitation reactions are summed to present only one excitation curve. The Electron Energy Distribution Function (EEDF), divided by the square root of the energy, is overlaid on the plot using the right side as the ordinate to show the relative significance of each contributing reaction. The EEDF in this plot represents a collection of data collected at 830 Torr, 1100 V and 527 μm between the ground and anode meshes.

2.3.5 Relative Reaction Rate

Coupled with the Penning Transfer rate and the upper bound for electron avalanche gain given by the Loeb-Meek criteria in Chapter 3, calculating the distribution between helium ionization, helium excitation, and CF_4 ionization reactions can provide an estimate for the total photons produced in the avalanche. With data from LXCat and simulations computed online by Bolsig+, Figure 2-6 shows that the electron ionization cross section for CF_4 is almost two orders of magnitude higher than helium [58, 65]. In Figure 2-6, only reactions that create or remove electrons are displayed, where helium excitations create electrons through the Penning transfer. There are many excitation reactions with CF_4 and elastic scattering from either gas component that do not remove or create electrons. As such, these reactions are not plotted. Further, helium excitation reaction curves of significance are summed to show only one curve, to reduce noise in the plot.

The cross section curves in Figure 2-6 can be scaled for specific gas mixtures, multiplied by the electron energy distribution function (also displayed with the ordinate axis on the right), and integrated to give an estimate of the Relative Reaction Rates (RRR) for given conditions, as shown in Equation 2.14. In Equation 2.14, σ_i represents the cross section for the reaction of interest, f_E represents the electron energy distribution function, and RRR_i the relative reaction rate for the reaction of interest.

$$RRR_i = \frac{\int \sigma_i f_E dE}{\sum_i RRR_i} \tag{2.14}$$

With the understanding that the total number of electrons created in the avalanche will be limited by a different mechanism, the streamer formation and breakdown discussed in Chapter 4, only the relative reaction rate is of concern in determining the total signal. However, some interesting insight can be gained from these relative reaction rates and the Penning transfer rate. First of all, increasing the electric field (ie, smaller gap sizes require higher fields before reaching breakdown conditions), increases the relative reaction rate for attachment faster than any other reaction. Second, increasing the concentration of CF_4 also increases the relative rate of attachment, removing electrons from the avalanche. Operating at very low concentrations of CF_4 creates very high helium excitation relative reaction rates compared to all other reactions, where the Penning transfer will create CF_4 ions for scintillation.

Inevitably, a gas mixture that maximizes CF_4 ionization is preferred, as the scintillation light given by CF_4 is both optimal for detection by standard digital cameras as well as typical photocathodes in image intensifiers, depicted in Figure 2-7 and the total light output is high compared to other scintillating gases. At 1000 Torr of 90% partial pressure helium and the balance CF_4, 13% of the reactions resulted in a loss of electron due to attachment on CF_4, 39% resulted in direct CF_4 ionization, only 1.5% direct helium ionizations, and 47% helium excitations across the top 10 most probable excitation levels. With an 86% Penning transfer rate, this equates to an approximate 80% of the electrons liberated in the avalanche leading to a CF_4 ion, with approximately 15% of these ions scintillating a photon in the spectrum given in Figure 2-7.

2.3.6 Solid Angle Losses

Within tens of nanoseconds of a CF_4 ionization reaction, the ion decays by the emission of a photon from the spectrum depicted in Figure 2-7. This light is produced isotropically. The digital camera lens and distance from the avalanche region

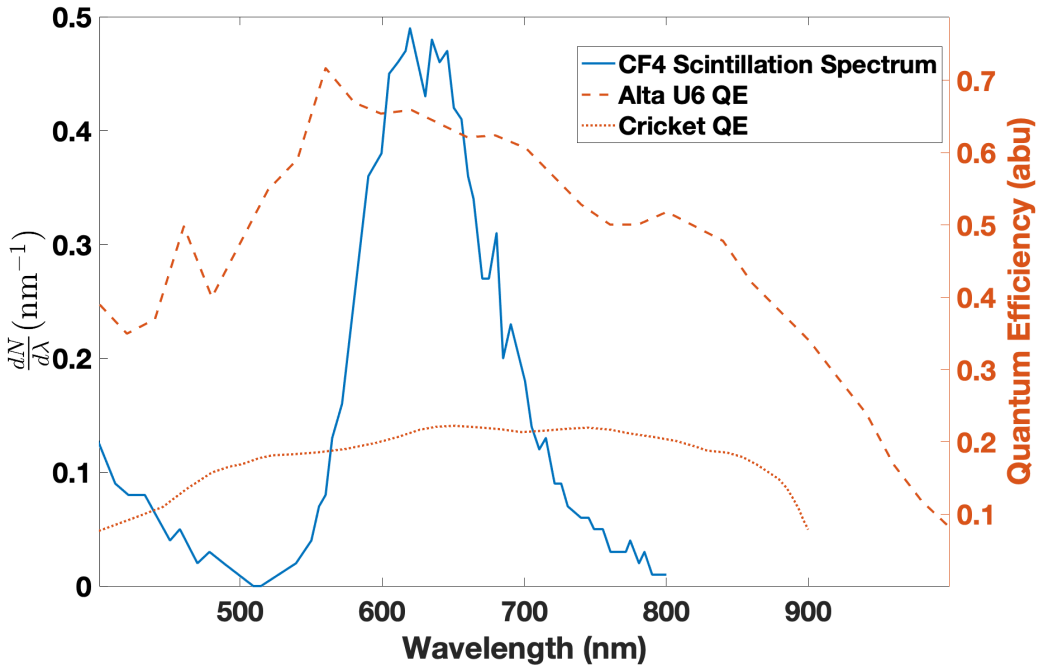

Figure 2-7: A comparison between the scintillation spectrum of CF_4 versus the quantum efficiency for the two systems used in this course of research, the Alta U6 Scientific CCD camera and the Cricket Image Intensifier. The CF_4 scintillation spectrum extends further into the UV spectrum but is omitted in this plot to focus on the quantum efficiency of the equipment used.

determine how much light is collected per pixel of the camera.

The distance between avalanche region and the camera lens, L, combined with the focal length of the lens, f, determine the magnification in the focal plane. Equation 2.15 describes the percentage of the photons reaching the pixel, here called β, from a point light source. The effective aperture is denoted by D and is equal to the focal length, f divided by the lens speed, commonly referred to as the f-stop and here denoted by F. Γ refers to the total light emitted from the point light source.

$$\beta = \frac{\pi(\frac{D}{2})^2}{4\pi L^2}\Gamma \tag{2.15}$$

Each camera pixel or micro-channel for the image intensifier is mapped to a portion of the avalanche region, given by the magnification of the lens, camera, avalanche plane distances and the focal length of the lens. This is shown in Equation 2.16, where p_{camera} is the dimensions of the pixel in the camera and p_{av} is the dimensions of the same pixel mapped by to the avalanche plane.

$$p_{av} = \frac{L}{f}p_{camera} \tag{2.16}$$

With this, the total light reaching each pixel from the avalanche is approximately the sum of all scintillating ions that occur within a column between the ground mesh and the anode mesh, with in-plane dimensions given by p_{av}^2. This is depicted in Figure 2-8 and in Equation 2.17, where β_{ppp} represents the photons per pixel and n_{ion} represents the ion number density, given approximately by a Gaussian orthogonal to the initial recoil direction and by the Bethe-Bloch along the track length. This integration is carried over the area of the camera pixel mapped to the amplification plane and the depth of avalanche, as depicted in Equation 2.17 by integrating over the volume, V, of the box shown in Figure 2-8.

$$\beta_{ppp} = \frac{(\frac{f}{2F})^2}{4L^2}(\frac{L}{f}p_{camera})^2 \int_V n_{ion}dxdydz \tag{2.17}$$

Equation 2.17 shows that the distance between the camera and avalanche region and the focal length both cancel out. This leaves the only contributing factors for the signal-to-noise ratio in each imaging pixel is the size of the pixel, the F-stop, and the single electron gain. In other words, installing a unique lens to bring the camera closer does not improve the signal-to-noise ratio per pixel. This change makes the pixel map to a smaller area in the avalanche plane, but does not increase the imaging system signal-to-noise.

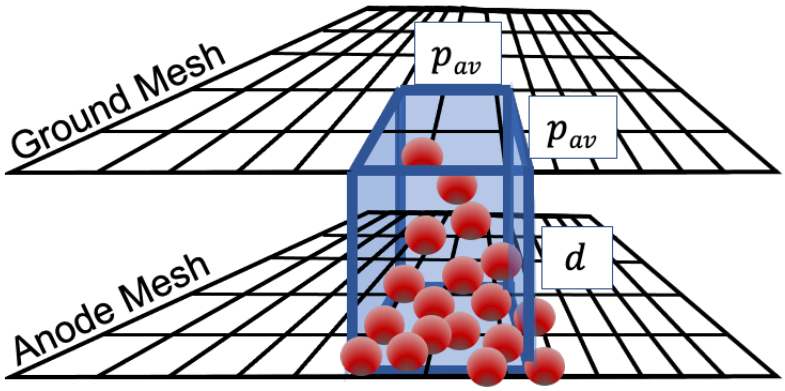

Figure 2-8: The volume integral dimensions to integrate all photons produced within a single pixel mapped to the avalanche plane. The in-plane dimensions are equal to a single camera pixel, magnified on the avalanche plane, and the distance between the two meshes, d. Any scintillation that occurs in this volume will be approximately mapped to a single pixel.

2.3.7 Camera Noise

The number of photons per pixel is competing with the imaging system's dark noise and read noise. With typical small, low-power digital cameras, the single pixel noise is under ten electrons per pixel. CCD cameras offer on-chip binning, where multiple rows are summed into one and multiple pixels summed into one bin prior to passing the charge through the on-chip amplifier. This greatly improves the signal to noise. Newer digital cameras are trending towards Complementary Metal-Oxide Semiconductor (CMOS) cameras, which have low dark noise and read noise comparable to CCD cameras. However, binning the CMOS cameras provides no benefit comparable to CCD binning, since signal amplification happens at the pixel.

Another option is to use an image intensifier. The benefit to using an image intensifier is the significant reduction in power consumption, which greatly improves the one-person portable capabilities. However, the equivalent to a camera's dark noise arises in the spontaneous emission of electrons from the photocathode. This dark current becomes a serious concern much sooner than a digital camera's dark noise. Overcoming this dark current, however, results in a signal that is significantly amplified prior to reaching any digital camera chip. As a result, the detector can be constructed with almost any small, non-cooled digital camera, as the camera will simply be taking a picture of the intensifier phosphor screen. This course of research investigated the used of an image intensifier called the Photonis Cricket and is reported in Chapter 3.

2.4 Time Component

Paired with the imaging system, an additional readout channel needs to be provided in order to provide the third component of the track, orthogonal the amplification plane. To date, this type of detector has typically used charge readout on the anode plane (mesh or plate) to provide that third component. This course of research focuses on the use of a large Photomultiplier Tube (PMT) placed only three inches from the avalanche region in order to improve statistics.

Through charge channels, a current-integrating, Charge Sensitive Preamplifier provides the total charge passing through the avalanche region. The maximum of the waveform pulse from the CSP can be used to calculate the total charge in the avalanche through knowledge of the pre-amplifier gain by manufacturer's published value and calibrated with a waveform generator. From this total charge, the detector can be calibrated to use the total charge divided by the single electron gain to provide the energy of the initial alpha recoil, necessary for the probabilistic projections used in Chapter 7. However, determining the time that the track passes through the avalanche region, which provides the third track component, becomes a more uncertain process since the pulse forms a relatively smooth, flat peak. Further, using the slope to determine the pitch of the track induces error in the fact that the first and second half of the track have different rates of change in regards to linear electron density, as depicted in Figure 2-4.

Switching to a PMT channel with high statistics provides the opportunity to time the third component based purely on start of waveform to end of waveform. Further, the head-versus-tail aspect of the PMT waveform becomes a fairly easily calibrated signal by selecting whether the peak of the pulse occurs at the end or at the beginning. This is discussed in Chapter 3 and results provided in 6.

2.5 Detector Principles Conclusion

In order to transition from a heavy, power-hungry Electron Multiplying Charged Couple Device (EMCCD) camera or scientific CCD, the number of photons per pixel must be high enough to overcome the pixel-to-pixel noise in the imaging system. Increasing this total gain will improve the signal-to-noise ratio in each pixel, allowing operation with a compact, low-power camera. As shown, the components that will improve the total number of photons per pixel are the pixel size in the camera, the F-stop (lower is better), and the single-electron gain in the avalanche. Further,

the addition of a low power image intensifier between the amplification plane and camera will remove the need to provide camera chip cooling, driving down the power requirements for the system. Finally, transitioning to a large PMT in close proximity to the avalanche region will improve the reconstruction of the third recoil component, as well as improve knowledge of the head-versus-tail information in the direction orthogonal the amplification-plane.

Chapter 3

Detector Operation, Data Acquisition and Data Analysis Algorithms

3.1 Introduction

In keeping with a portable detector concept, all equipment was selected in regards to physical size and power requirements. Further, algorithms written focused on computational efficiency. All power and voltage reference cables are represented in Figure 3-1. In future work, the goal is to transition from a desktop DAQ computer to a microcomputer that also requires minimal power. In the experiments conducted by the Dark Matter Time Projection Chamber collaboration and previous experimental efforts, multiple computers were used for data acquisition and data analysis. However, in using this similar technology and transitioning to a compact, portable detector, new track finding algorithms and Photomultiplier Tube (PMT) waveform analysis algorithms were written to capitalize on the nature of device readout, with the goal of reducing computational requirements. The data analysis algorithms written in this work are focused on rapidly compressing the data stream from a full image and multiple digital waveforms per second to a handful of output quantities, such as energy, range, position, etc. In this regard, the image analysis algorithms mimic the standard readout nature of a digital camera and the waveform analysis algorithms avoid the use of smoothing and fitting. Further, after transitioning to the Image Intensifier, software triggers were used to only read the image after a PMT signal was registered. Therefore, the images stored to memory have a high likelihood of having a nuclear recoil present in the image. This data is further compressed to reject the majority of the image, compressing to only the immediate vicinity of the

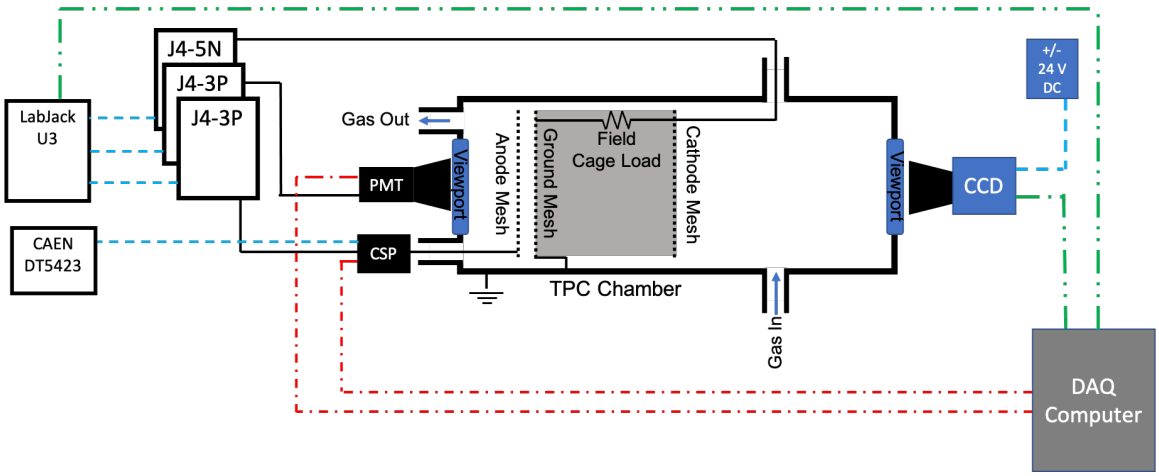

Figure 3-1: This diagram depicts every connection to the detector chamber, denoted by the thick black line. The active volume is denoted by the shaded region between the ground mesh and the cathode mesh. The blue dashed lines represent the low voltage power cables and the low voltage reference wires to the high voltage power supplies. The solid, black lines from the J4 high voltage power supplies represent Safe High Voltage (SHV) coaxial cables. The red, dot-dash lines represent the "Bayonet Neill–Concelman" (BNC) cables sending the output signals from the PMT and CSP to the DAQ computer. The green dot-dot-dash lines represent the USB cables connected the Labjack controller and the CCD to the DAQ computer.

track. Since this detector is intended to be used for fast neutron detection, alpha recoils are expected to be relatively long with many thousands of initial electrons. As such, avoiding computationally hungry image algorithms and curve smoothing and fitting algorithms is within reason.

3.2 Detector Operation

For the course of this research, data acquisition and data analysis algorithms were split between different computers in order to store all possible data streams to spot check that the algorithms were performing as expected. Prior to any data collection, the detector was pumped down to 10 mTorr for a minimum period of 10 minutes and then filled with a predetermined pressure of 90% ^{4}He and 10% CF_4, where the pressure was determined based on the goals of the run. Data was collected at a variety of pressures, most commonly 300, 600, 1000 Torr. Once the detector was filled with target gas to the appropriate pressure, the detector was operated remotely. The detector high voltages were powered by three Matsusada high voltage power supplies, controlled by a Labjack U3 [66]. The cathode power supply was a Matsusada J4-

5N, a negative polarity power supply providing up to 5 kV output voltage to the cathode at a maximum current of 500 μA and less than 10 mV peak to peak ripple. The field cage rings were all connected through 2 MΩ resistors, resulting in 50-100 μA across the variety of drift distances and cathode voltages used in this research. The anode and Photomultiplier Tube were powered by two J5-3P units, providing up to 3 kV output voltage to the anode at a maximum current of 1 mA and less than 3 mV peak to peak ripple. Each power supply required a 0-10V reference with a linear relationship between 0 and maximum voltage output. The power supplies received this reference voltage from the Labjack U3. The Labjack U3 provided two organic Digital-to-Analog Converter (DAC) channels offering up to 5V reference [67]. An additional DAC channel was added with the "LJTick-DAC" accessory, adding two channels up to 10V reference [68]. The PMT and cathode power supply were powered off the LJTick-DAC accessory. The anode power provided a bias voltage to a Cremat Charge-Sensitive Preamplifier (CSP) 113 [69]. The CSP also required a bipolar 12 V power connection, provided by a CAEN DT5423 low power, low voltage desktop power distributor [70].

3.3 Data Acquisition

Once the detector was filled with target gas and the voltages connected, the detector was operated autonomously through a Data Acquisition (DAQ) program from the DAQ computer. This program could be started and monitored remotely through a Secure Shell (SSH). The CSP and PMT were both connected through 50 Ω, DC connections to each channel of a two channel, 8-bit, Alazartech ATS-860 digitizer, which was installed on the data acquisition computer in a Peripheral Component Interconnect (PCI) slot [71]. The CCD camera was connected and readout to the data acquisition computer by a USB cable. The detector had two primary run settings: one second exposure for the Alta U6 digital camera and continual flushing for the Image Intensifier/CCD setup.

For the one second exposure data collection, an Alta U6 scientific CCD camera was used [42]. The Alta CCD has an internal shutter that was used to prevent tracks from appearing during the image readout, causing a misinterpreted position in the amplification plane. The digitizer was set to record up to five records per acquisition period, triggering each record on either the PMT at a negative trigger threshold or the CSP on a positive trigger threshold. After the DAQ started the digitizer capture algorithm on the ATS PCI card, the program opened the shutter and exposed the

Alta CCD for one second, read out the CCD image, and then pulled all five waveforms from the ATS digitizer. Later in the analysis process, the waveforms and images are scanned to match image track, CSP pulse, and PMT pulse.

When switching to the intensified CCD setup, a Phonotis Cricket Image Intensifier was coupled to a Finger Lakes Instruments (FLI) MLx285 CCD camera [72]. The CCD required continual flushing due to the temporal noise profile of the Cricket, as discussed in detail in Chapter 3.7.3. As such, the detector operated in a continual loop of CCD flushing with the digitizer triggering on a single record. At the beginning of each loop, a single call to the digitizer was performed to see if the digitizer had triggered. If the digitizer was triggered, the loop finished with a full image readout from the CCD, pulled the waveform pulses from the two digitizer channels, and finally restarted the digitizer acquisition. If the digitizer was not triggered, the loop continued with CCD flushing. This order allowed the CCD to be read immediately after the exposure was finished, versus potentially grabbing the image a short while after the exposure had completed, resulting in a varying noise profile.

3.4 Image Processing

As mentioned, the algorithm developed for this detector focuses purely on the nature of CCD readout to computer memory and compresses the image into smaller images that contain minimal wasted memory. While the algorithms were being built and tested, all full images were stored, in addition to the compressed images and track information. Further, due to the capabilities of the CCD camera for this research, additional steps were required in order to clean the track signal prior to using the linear detection algorithms. These additional steps include removing the dark frame, applying a brightening step, applying a median filter, determining the track bounds, and subsequently passing the compressed image through track detection algorithms. These steps, from bias-frame to the track detection will be described in this section.

3.4.1 Dark Frame Images for CCD Data Runs

In a detector of this nature, the overwhelming majority of individual pixel values in each CCD image is pixel-to-pixel noise generated by the CCD electronics. There are two sources of pixel-to-pixel noise within a digital camera: dark noise and readout noise. The dark noise, also referred to as dark current, is noise generated when thermal motion creates electron-electron hole pairs within the pixel, which is subsequently

passed through the readout scheme as if a photon created the charge pair. Reducing the temperature of the CCD chip and operating at shorter exposure times reduces this thermally generated noise. Readout noise is generated when the charge in a pixel is shifted from the last pixel in the readout row into the computer electronics by means of an amplifier. With typical low-noise, astrophotography digital cameras and exposure times on the order of one second or less, the readout amplifier noise dominates and produces noise comparable to tens of electrons per pixel. The light emitted from a recoil event must overcome this noise and produce a cluster of pixels above the noise floor of the CCD. With the understanding that the electron amplification coupled with an appropriate lens-CCD combination, the algorithm should assume that each useful track will meet this criteria, producing a cluster of pixels all above the noise floor.

In order to minimize the pixel-to-pixel noise and pixel-to-pixel inherent variation, the camera was operated for 100 shutter closed images prior to every run. This provides an average value for each pixel across 100 shutter-closed frames. The pixel-to-pixel read noise can be closely modeled with a Gaussian distribution, as depicted in Figure 3-2. The tail to the right of the Gaussian is from to dark noise, cooling mechanism aging, and chip aging.

3.4.2 Track Brightening

Since this camera was an older camera with a higher noise profile than camera setups anticipated for future setups, the images required additional algorithms to brighten the tracks prior to track detection. The noise is assumed to be Gaussian distributed with a small exponential tail extending to higher pixel values. The exponential tail results in approximately 5% of the pixels to have an energy higher than the standard three-sigma threshold to the Gaussian fit. This was measured over a standard dark frame data collection with 100 images. This pixel noise spectrum can be seen in Figure 3-2. The random nature of pixels that sit above the threshold and also sit next to other pixels above the threshold is assumed to be independent. The likelihood that enough "warm" pixels sit above the threshold in a five-by-five median filter window requires 13 of the 25 pixels to be above the threshold. This results in fewer than one, two-by-two pixel area, statistically generated track in one million seconds of exposure. Further, if a track is statistically generated, the likelihood that a matching pulse arrives from the PMT in the appropriate time window further suppresses the likelihood of erroneous tracks.

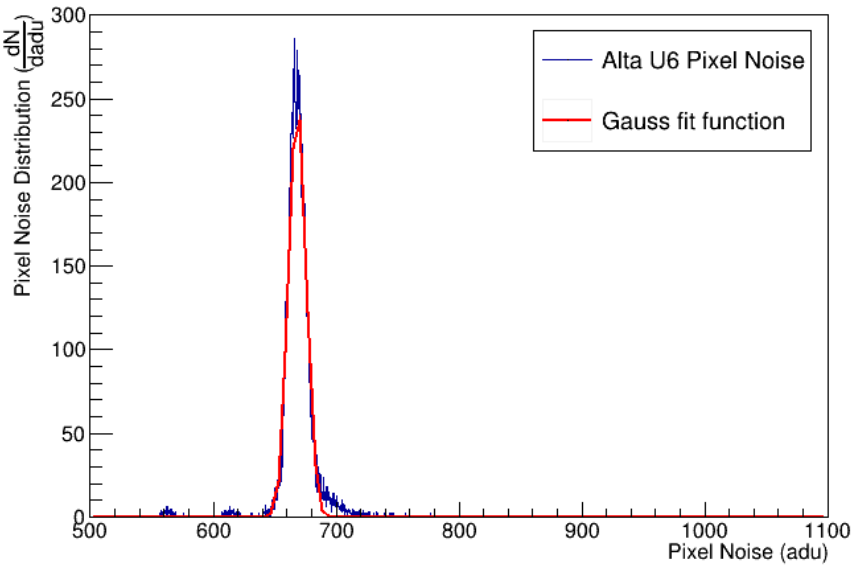

Figure 3-2: An example of the average pixel-to-pixel noise across 100 dark images taken before the start of a run. In this histogram, the blue curve denotes the Alta U6 pixel-to-pixel noise, while the red curve represents a Gaussian fit to provide details on the standard deviation in the noise profile. This standard deviation is later used to clean the image, as well as in the track finding algorithm.

Therefore, using the three sigma as a threshold, each pixel above the three sigma threshold is multiplied by a factor of ten in order to brighten the tracks for rapidly cycling through images to visually check the algorithms while training the algorithms. The image is subsequently passed through a five-by-five median filter removing isolated warm pixels randomly distributed throughout the image. After this track brightening and median filtering, the image is passed through the track bounds detection algorithms, where neighboring warm pixels are tagged as track bounds as described in the next section.

3.4.3 Determining Track Bounds

Digital cameras read out the pixels in a pixel-by-pixel followed by row-by-row fashion. In this sense, a matrix of a million pixel values (a 1000 by a 1000) is converted into a one-dimensional array with a million elements. In a similar fashion, the algorithms written for this work focused on tagging track bounds in a linear fashion to be used in future portable detectors. Rather than entering additional loops in the Nearest Neighbors method of the DMTPC collaboration, the linear approach achieved similar results while reducing computational cost for future portable detectors.

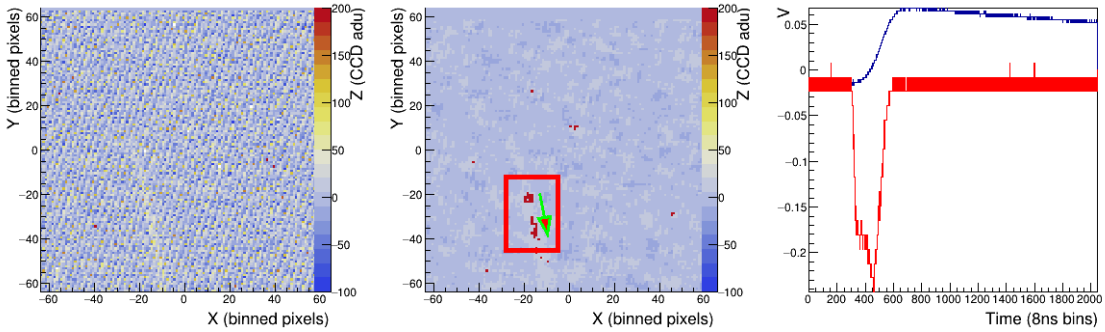

Figure 3-3: This figure depicts the before and after images using the track brightening method. This is primarily for rapidly spooling through data sets and visually confirming the presence of tracks and visually confirming the algorithms are correctly identifying the direction and track bounds. This track likely occurred at the furthest point from the amplification possible, as the image only retains an incredibly dim track. The PMT and CSP provide high resolution data for the energy and the image is used entirely to reconstruct the projected direction and range in the amplification (XY) plane.

For the linear track finding approach, the linear density of pixels above a given noise-threshold is monitored. In other words, if the mean pixel energy is μ, with a statistical variance of σ_μ, any pixel above a value of $\mu + 3\sigma_\mu$ would increase the linear warm pixel density. If the linear density in a running window of five pixels rises above a predetermined threshold, a flag is thrown that indicates the beginning of a track for that specific row. For the extent of this research, at least 80% of the pixels had to be above the three sigma threshold in a horizontal window at least three pixels wide. When this criteria is met, the left-most pixel of the running window is tagged as the left track bound. When the linear density drops below the same threshold, the algorithm registers the end of a track for that row. In this sense, multiple tracks can be detected in each row and rows are later stacked and sorted into overlapping regions to define a compressed track image.

After the track bounds are tagged, the track bounds are then sorted into groups, only handling the left and right limits of the track bounds. The tracks are combined if the track left-to-right bounds overlap and are within one to two rows. The largest column and largest row are logged as the compressed image right and top bounds while the smallest column and smallest row are logged as the left and bottom bounds. The boxes are then passed through a box-overlap check, where overlapping boxes are further combined into one compressed track image. This is depicted in Figure 3-4.

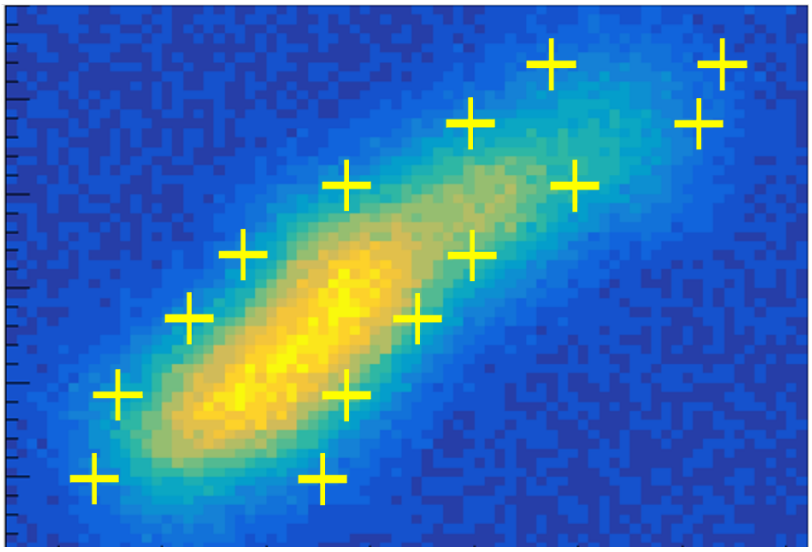

Figure 3-4: A cartoon depiction using a simulated track image, showing the algorithm to determine the track bounds as the pixel values are readout from left to right in a row-by-row basis. The yellow cross-hairs depict the track bounds that would be tagged, passing only the pixel values between the bounds to further image processing steps. This immediately reduces the computational handling of a 10^5 to 10^6 element array to a few hundred elements array per track.

3.4.4 Track Analysis

After the tracks are sorted into bounds of compressed track images, the compressed track images are processed for data. In the same fashion as the DMTPC algorithms, the angle is determined by calculating the weighted covariance matrix, and using the eigenvalues to calculate the rotated coordinate axis that aligns with the track. This is discussed in detail in [73] and [53]. The length is determined by computing the hypotenuse of a triangle formed by the maximum horizontal distance and the maximum vertical distance of the track bounds in the previous paragraph. In previous versions of this type of detector, the end of the track was determined by comparing the total integral in each half of the track. Referring back to Figure 2-4, it is clear that the point along the track with the highest electron density, or in the case of an image the brightest point of the track, will occur at the beginning of the track for tracks approximately 10mm and shorter. In this regard, the center of the brightest nine pixels (3X3 array) was logged as the maximum point in the track and logged as the beginning of a short track or the end of a long track. This cutoff corresponds to an alpha recoil energy of approximately 1.4 MeV. The opposite is true for tracks 20mm and longer, where energies greater than 2.6 MeV have the most energy deposited predominantly at the end of the track. In between these two ranges, the energy is

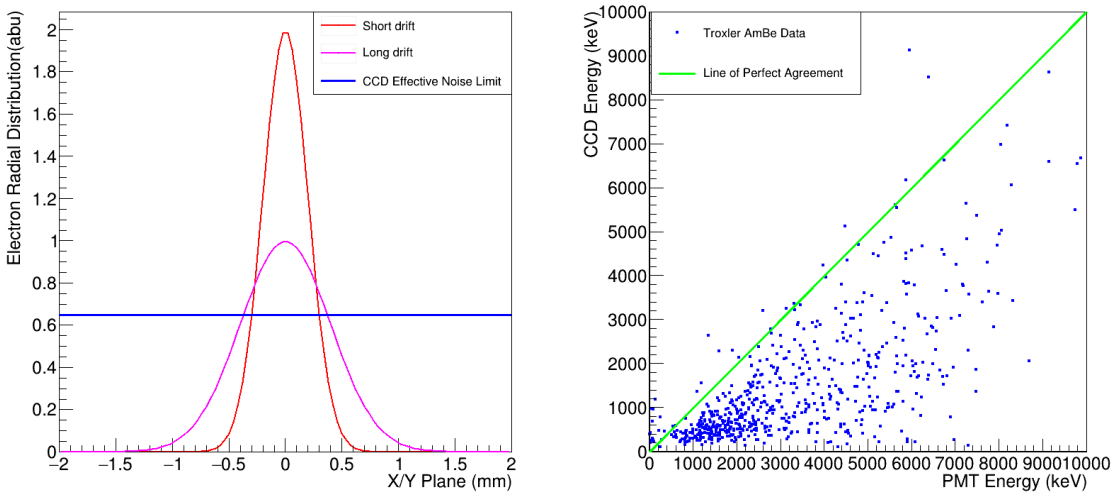

(a) (b)

Figure 3-5: (a) A cartoon sketch depicting the difference between a track occurring in the immediate vicinity of the amplification mesh and a track that has drifted a significant portion of the detector and diffused in the process. The integral of the entire track above the CCD noise will be suppressed at higher drift distances, allowing the data analysis algorithms to make low-resolution decisions about Z location. (b) Data points from a Troxler AmBe neutron source that show the discrepancy between high resolution energy reported by the PMT and the CCD energy falling anywhere between full agreement with the PMT to zero.

deposited very close to the middle of the track, resulting in significant uncertainty about the true direction of the alpha.

From this algorithm, the end point location within the amplification plane (X,Y), the direction, an estimate of the total energy, and the length of the track are determined. A low-resolution Z position can be determined by comparing the total track energy as reported by the digital image and the total track energy reported by the Photomultiplier Tube (PMT). As the track drifts and the electrons diffuse, more and more of the track will drop below the CCD noise threshold, as depicted in the left of Figure 3-5(a). The PMT is sensitive enough and in close proximity to the avalanche region, allowing it to collect a significant portion of the emitted light, regardless of track diffusion. As a result, the PMT should have the optimal energy resolution of the entire setup.

This Z-position tagging can also be viewed by analyzing the energy reported by the PMT versus the energy reported by the track integral in the image for all events. This can be seen in Figure 3-5(b), where the PMT is assumed to have a very high

energy resolution and the CCD reports energies that only follow the line of agreement on the upper edge. The data points extend from agreement all the way to zero. This is an indication that the tracks are becoming significantly more dim as the electrons drift and diffuse radially outward. To use this for tagging a low resolution Z-position, the ratio of CCD energy to PMT energy is multiplied by the total drift distance, as depicted in Equation 3.1. In this equation, $z_{estimate}$ represents the reconstructed Z-position, $L_{detector}$ the total drift distance, E_{CCD} the energy recorded by the CCD, and E_{PMT} the energy recorded by the PMT.

$$z_{estimate} = L_{detector} \times (\frac{E_{CCD}}{E_{PMT}}) \tag{3.1}$$

3.5 Digital Waveform Analysis

The primary goal for this detector is to run solely with a Photomultiplier Tube (PMT) to provide the energy, time, and the vertical track information. However, for the extent of this investigative research, a Charge Sensitive Preamplifier (CSP) is included to compare the results of the PMT with previously studied results. Both the CSP and PMT are operated in DC-mode, connected to each channel of a two-channel ATS860 digitizer, operated at 125 MHz.

3.5.1 CSP Waveform Analysis

For this research, a CREMAT Charge Sensitive Preamplifier 113 was connected to the anode and operated in DC mode. At times with the triple mesh testing, a Cremat CSP 110, 111, and 112 were also used for very low gain settings. The CSPs were operated in a CREMAT 150 evaluation board, where +/- 12V were supplied to the evaluation board. As mentioned, the CSP output was connected to an ATS 860 Peripheral Component Interconnect (PCI) card, operated at 125 MHz. For the majority of the AmBe data collection, the CSP waveform maximum range was set to $\pm$ 400 mV on the digitizer, resulting in a highest possible resolution with minimal number of waveforms clipped at the maximum range. The waveform triggers were set to 0 mV, since the CSP, operated in DC mode, had a slight negative bias offset from 0 V. The total charge for typical alpha recoil events was high enough that the waveform was well above the CSP noise floor, requiring no waveform smoothing. The first one hundred sample points were used to calculate the bias offset for that specific waveform, and the maximum value used to calculate the total charge in

the avalanche. This could then be calibrated to an energy value using an Am-241 alpha source with known energy spectrum. As discussed in previous DMTPC works, using a CSP for energy readout opens the possibility of having a ballistic deficit [73]. The ballistic deficit occurs when the time required for the track to fully pass the amplification plane is comparable to the decay time of the current-integrating, charge sensitive preamplifier. For high-pitched, alpha recoil tracks with length on the order of centimeters, drifting at approximately 0.8 to 1.0 cm/μs, and a CSP decay time of 50 μs, a ballistic deficit can commonly approach the 10% level. When primarily looking at longer alpha recoil tracks, the ballistic deficit becomes a very systematic contribution to the CSP energy resolution.

The pitch in the amplification plane orthogonal direction is determined by the time required for the CSP waveform to pass from baseline to maximum value. The uncertainty in this scenario arrives from the uncertainty in accurately determining where the maximum occurs when the ballistic deficit is already starting to add to the smooth shape of the waveform peak in this channel. Further, the Z-direction head versus tail can be computed by analyzing the rate of change of the slope of the CSP waveform. If the slope gradually decreases versus gradually increases from baseline to waveform maximum value provides evidence for the peak density of the track occurring at the bottom versus the top of the track in the Z-direction. However, this also exposes significant uncertainty in the CSP analysis. For these reasons, the primary emphasis in this research was focused on building the capabilities of a large PMT in immediate proximity to the amplification plane.

3.5.2 PMT Waveform Analysis

A 3.5" Ludlow PMT was used for this research. The PMT was placed immediately outside a 3.8" viewport that was approximately 5 cm from the amplification plane. The PMT was read-out through the second channel of an AlazarTech ATS 860 digitizer with a sampling rate of 125 MHz. For most of the AmBe data collection, the maximum range for the PMT was set to $\pm$ 4 V. With a majority of the alpha recoils having energies of 50 keV and above, the range was selected to minimize clipped waveforms for higher energy recoils. However, with only 8 bit resolution, very low energy recoils resulted in higher uncertainty due to the low waveform amplitudes. Due to the proximity between the PMT and the amplification plane, the solid angle losses were minimal, giving a significant total light collection. The PMT provided the highest energy and timing resolution, due to the fast readout time compared with

the CSP and CCD data streams. Since the PMT waveforms were never a smooth pulse and were always well above the noise threshold, no waveform smoothing was conducted. Multiple details of the original track were collected after processing each waveform.

Due to the fast data sampling and the fast nature of PMTs, the waveform gave direct feedback to the Z-component of the track. The length of time required for the entire track to pass through the amplification region, indicated directly by the temporal length of the PMT waveform, provides the Z-component of the track length through Equation 3.2, where R_z is the magnitude of the range in the direction orthogonal to the amplification plane (Z), w_t is the width of the waveform in digitizer samples, S_{rate} the digitizer sampling rate, and μ_{drift} the electron drift speed.

$$R_z = \frac{w_t}{S_{rate}} \mu_{drift} \tag{3.2}$$

In order to determine the width, the waveform algorithm tagged the sample at which the waveform dropped beneath a set threshold (negative polarity waveform), typically 50mV, and tagged the time that the waveform passed back above that threshold. Further, the waveform had to be continuously below the threshold between start and end, in order to prevent any pileup concerns occurring where additional pulses occurring shortly after the primary pulse create erroneous significantly longer waveform temporal lengths.

In addition to the Z-component of the track length, the waveform provides information on the track being directed in the positive Z or negative Z through the amount of energy deposited at the beginning and end of the pulse. The rise time of the waveform has an approximate Gaussian shape due to the Gaussian diffusion of electrons, but the decay of the waveform is exponential, related to the probabilistic nature of excited state decay and emission of scintillation light. As such, the waveform was integrated on either side of a point 45% into the temporal length of the waveform. The 45% point was empirically determined, but also loosely agrees with a Gaussian distribution of $\sigma = 10$ns (related to a diffusion of ≈ 0.1 mm) followed by an exponential decay of $\lambda \approx 15$ns (the CF_4 primary scintillation decay constant) [51].

Finally, as discussed in previous sections, the PMT is capable of excellent energy resolution due to the PMT photocathode size and the proximity of the PMT to the avalanche. For a 50keV alpha recoil, approximately 11,600 electrons are liberated in the initial recoil, calculated using quenching factors produced from SRIM data [57]. Using a conservative Fano factor of .17, the relative variance from the initial recoil

should be well below 1%. Assuming that each avalanche is independent, the fractional error of the avalanche corresponding to each electron is approximately 50% [27]. However, the large number of electrons entering the mesh will cause this relative variance to be reduced to a Gaussian distribution by the law of large numbers. Resulting in an additional fractional error again below 1%.

Using a 3.5 inch PMT only inches away from the amplification region results in maximal light collected from the avalanche, introducing minimal additional variance in the total energy resolution. With a total gain of 10^5 in the avalanche and solid angle losses of approximately 80%, the number of photons collected by the PMT is on the order of millions, using conservative estimates of the Penning transfer rate. Additional factors that will impact energy resolution are electron attachment as the electrons drift through the TPC. This will be a systematic uncertainty, bringing the energy lower than expected depending on location of initial recoil. Further, the proximity of the amplification plane to the PMT can also induce variance due to the varying solid angle coverage between a track in the middle of the plane versus a track in the far edge of the plane. This variance will be systematic in under counting the energy for edge tracks versus middle tracks. The next section will cover techniques used to compensate for solid angle variance.

3.6 Combining All Data Streams

One of the most powerful aspects of a detector of this type is the combination of separate data streams into an array of data for each specific nuclear recoil. For instance, keeping a charge channel and a light channel, the systematic reduction in reported energy due to different solid angle losses between track location and PMT can be visualized by looking at the location of the track in the CCD and comparing the CSP-reported energy versus the PMT-reported energy. The CSP-reported energy will not be effected by the different solid angle losses between track position and PMT. The PMT-reported energy can be corrected by a geometric correction curve, where the distance between the center of the amplification plane determines the difference between the PMT energy calibration point at the edge. This is plotted in Figure 3-6. The PMT pulse profile is fitted to image track projection by comparing points of highest energy, and then the PMT signal is corrected for solid angle losses as a function of position in the amplification plane for each point in the PMT pulse.

In addition to the variation of solid angle losses versus position within the amplification plane, the time profile of the PMT pulse should be similar in nature to

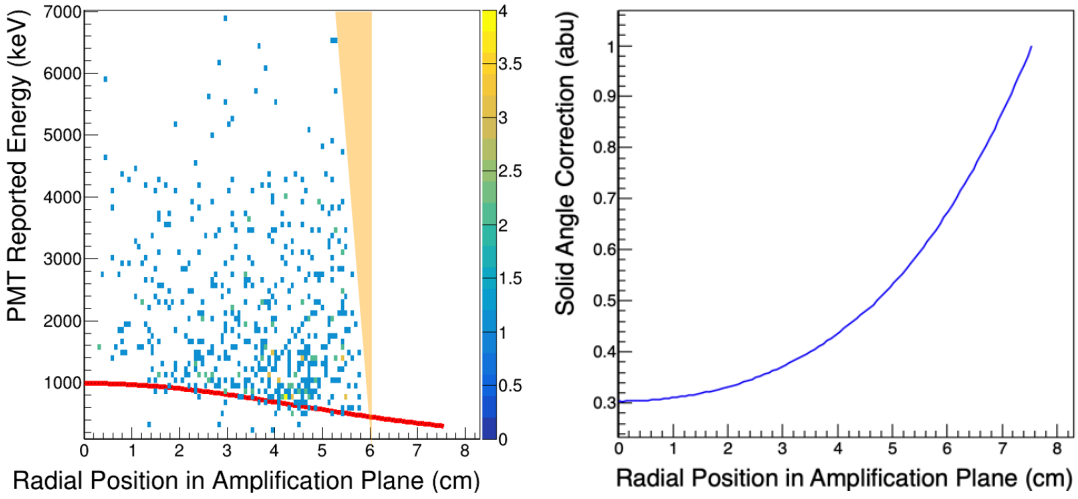

(a) (b)

Figure 3-6: (a) Data from an AmBe neutron source run that shows the solid angle difference between the center and the outer edge of the amplification plane. The red curve represents a toy Monte Carlo written to calculate the difference in solid angel coverage from center to edge. The orange highlighted region depicts the difference in long tracks being cut from the edges more favorably than short tracks. (b) A correction curve computed from the the same Monte Carlo to correct for the difference in solid angle acceptance of the PMT. The energy calibration was conducted with an alpha source at the very edge of the amplification plane, where the correction is one. As the track approaches the center of the amplification region, the total collected light increased by almost three times, and would otherwise over estimate the energy.

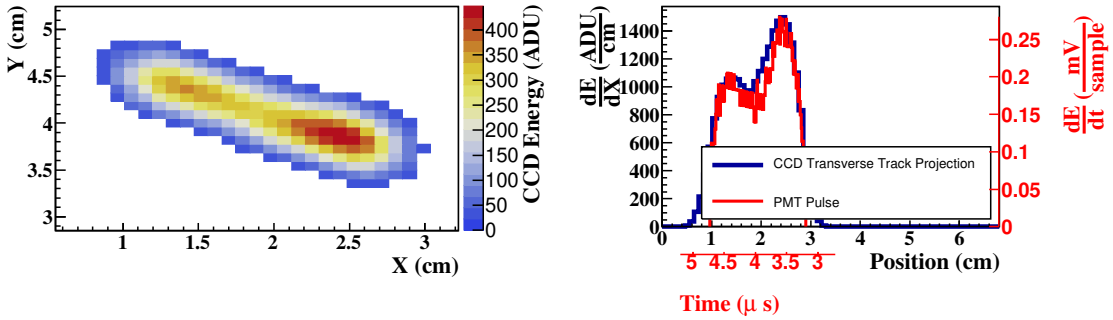

Figure 3-7: Left: An example recoil track from AmBe data to show the spatial variation of the track in the CCD image. Right: Comparing the projected total energy from the track recoil axis in the CCD with the time profile of the PMT pulse, after the PMT pulse has been reversed in time and inverted. The PMT is sampling at 125 MHz. It is clear that the variation of the track energy in the CCD is a function of the variation in energy deposited by the alpha recoil and not the data analysis algorithms as the pattern appears equivalently in the PMT pulse.

the deposited energy along the track recoil axis in the CCD, as long as the track is not nearly parallel or nearly orthogonal to the amplification plane. This can be seen in Figure 3-7. From comparing the track energy deposited in the CCD image and the energy deposited in the PMT pulse, it is clear that the variation in energy along the recoil track is not a by-product of the CCD noise profile or the data analysis algorithm, but rather a variation in the actual energy deposited along the recoil track. It is also seen that the hot-end of the track arrived at the amplification plane first, as shown in the PMT time-correlated pulse (reversed to plot against the CCD projection). If the track is nearly parallel to the amplification plane, the detail in the time profile is lost. In the same manner, if the track is nearly orthogonal to the amplification plane, the spatial variation is lost.

Finally, the PMT-reported energy approaches a resolution comparable to the CSP. Therefore, the PMT-reported energy can be compared to the CSP-reported energy as a function of the track pitch in the "Z" direction. Tracks that occur almost entirely parallel to the amplification plane should have little to no ballistic deficit, while tracks nearly orthogonal will having higher amounts of ballistic deficit. This can be seen in Figure 3-8, where data points from nearly parallel tracks are plotted in red and nearly orthogonal tracks are plotted in green.

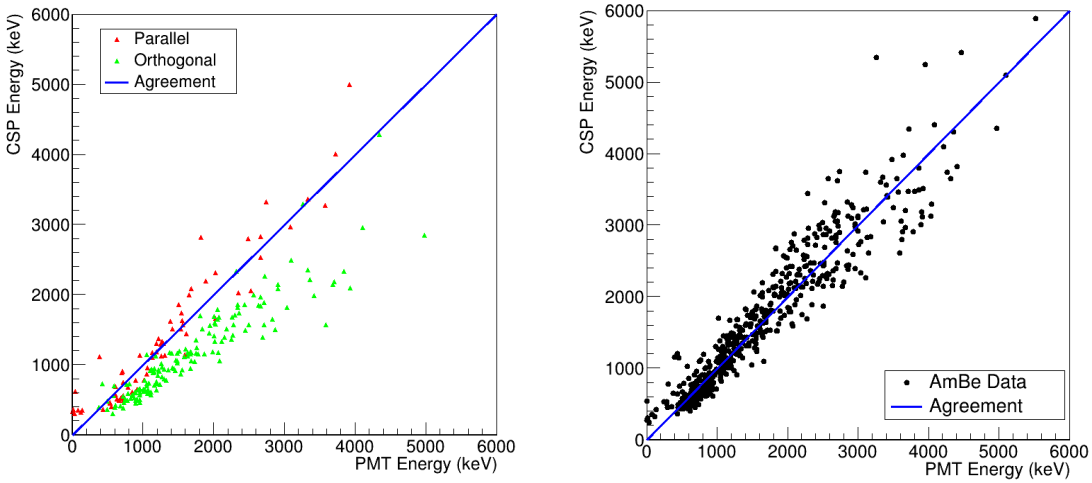

(a) (b)

Figure 3-8: (a) A comparison of the alpha energy reported by the PMT versus the CSP, after calibration and solid angel adjustments, as a function of track pitch. Tracks that are nearly orthogonal to the amplification plane see a ballistic deficit due to the 50 μs decay time of the CSP. As such, a ballistic deficit correction is applied, depending on track pitch, improving the CSP energy resolution. (b) The PMT-reported energy compared to the CSP-reported energy after solid angle corrections and ballistic deficit corrections. This curve indicates an approximate 25% energy resolution for either channel.

3.7 The Photonis Cricket™Image Intensifier

As discussed previously, the primary goal of this research is to develop a portable Time Projection Chamber (TPC) for a single person to wear as a backpack. In order to enable a truly portable system, the power requirements must be low enough that a modern battery pack can provide power for a day of operations. This rules out Electron Multiplying Charge Coupled Device (EMCCD) and Scientific CCD cameras. However, comparable work for high energy physics experiments have demonstrated using an optical TPC by boosting the light signal through a series of image intensifiers, followed by a CCD digital camera [47, 74]. This chapter is dedicated to the calibration and commissioning of a Photonis "Cricket" Image Intensifier and the sole image intensifier for the TPC discussed in Chapter 2.

The primary benefit in switching to an image intensifier is the significant power and weight savings. The power requirements drop from almost 100W for an EMCCD [41] or 40W for the Alta U6 Scientific CCD [42], to less than 60mW for the Cricket Image Intensifier [75]. In addition to the power savings, the weight of a typical EMCCD is 3.7kg (8lbs) [41], the Alta U6 is 1.4 kg (3.1 pounds) [42], and the Cricket is 450g (1 lb) [75]. Further, with an image intensifier, any non-cooled, lightweight digital camera can be installed to capture the image produced by the intensifier. Finally, this course of work seeks to also use the Cricket as an electrical shutter, powering down during read cycles to prevent erroneous readings that could include partial tracks, shifted tracks, erroneous tracks from intensifier noise, and late readout sparks negating the entire event. All of these artifacts which occur during readout are discussed in more detail in previous efforts by DMTPC [49]. For the commissioning of the Cricket, a Finger Lakes Instruments CCD camera was used due to availability, while future iterations will seek to use a Raspberry Pi camera for the significant weight and power savings.

3.7.1 Image Intensifier Fundamentals

The Cricket image intensifier can be broken into three major components: the photocathode, the Micro-channel Plate (MCP), and the phosphor screen. A fourth stage of fiber optic cables is added to direct the light into the attached camera, as the Cricket is specifically designed to mount directly in between a C-mount lens and a C-mount camera. Each of the three major components introduce a different noise and time profile from a stand-alone Scientific CCD or EMCCD.

The photocathode is the primary driver determining the quantum efficiency curve, or the likelihood of converting a scintillation photon to an electron in the image intensifier. The thermionic noise, discussed in the next section, derives from electrons spontaneously generated on the photocathode. The time characteristics of the photocathode are much faster than the phosphor screen, and therefore does not add much to the timing characteristics of the system. The measured dark count rate emitted from the surface of the photocathode at room temperature is approximately 30 Hz/cm^2 after approximately 10 minutes of operation, but can be as high as 1-2 kHz/cm^2 [76]. This seems to agree with the empirically determined settings discussed later in this chapter. When operating on a continual cycle of power on / power off cycles, the noise is in the kHz range, as opposed to the 10s of Hz range. However, operating at a continuous on results in a buildup of noise while the image is being read to memory. Future versions can incorporate a mechanical shutter between the MCP and the camera to block additional noise buildup and to aid in reducing the photocathode noise profile.

The Micro-Channel Plate (MCP) is the sole gain mechanism in the image intensifier. After an electron is created in the photocathode, the electron drifts to the MCP and multiplies in collisions with the walls of the micro-channels. Each channel is typically a glass tube coated with a semiconductor that serves as a secondary electron emitter when cascading electrons collide with the walls [77]. This cascading process is very fast, with timing properties on the order of 10s of picoseconds [78]. While the MCP will introduce new uncertainties due to the statistical fluctuation in the number of electrons created in each collision with the microchannel walls, this noise is mostly irrelevant to the image of the track. The integral of the imaging system is only used as a coarse estimate of original neutron interaction and is not used for alpha energy measurements.

The next stage in the image intensifier is a conversion of electron to light at the phosphor-coated lens. The Cricket image intensifier uses a P43 phosphor, which produces approximately 20 photons / e^- / kV on a time scale of milliseconds. As such, the data acquisition program needed to pause after registering a CSP pulse in order to allow the phosphorescence to decay. However, this can happen after the voltage to the Cricket is powered off in order to prevent any additional dark counts to accumulate.

3.7.2 Measuring the Cricket Noise

Although the power and weight savings alone support switching to the image intensifier setup, the noise of an image intensifier differs slightly from an EMCCD or scientific CCD. EMCCD and Scientific CCD cameras have read noise and dark noise. The former arises from the pixel energy being amplified through an operational amplifier, where the amplifier imposes an additional noise pattern on the readout. The dark noise arises from the spontaneous creation of an electron-hole pair in the silicon pixel, and can be reduced by cooling the chip. In most EMCCD and Scientific CCD cameras, the chip is kept at low temperatures, suppressing the dark noise and leaving only the read noise to deal with. The noise pattern in an intensifier is a function of the spontaneous emission of electrons from the photocathode [79]. At higher gain settings, the likelihood of spontaneous emission increases. Further, at longer exposure settings, the number of spontaneously emitted electrons will be higher than shorter exposures. Finally, at higher temperatures this thermionic process increases. However,introducing a cooling mechanism adds weight and power requirements. Therefore, the goal is to design a data acquisition system that overcomes the intensifier noise without requiring additional power or equipment. Since the intensifier is placed prior to the CCD electronics in the signal chain of events, overcoming the intensifier noise will minimize the effects of the CCD read noise, allowing any small CCD camera to replace the FLI cooled CCD camera. As such, a variety of tests with the intensifier-FLI camera setup were conducted to understand the noise characteristics.

Initially, 1,000 dark frames were taken with the FLI camera while the Cricket was powered off. This amounts to a measurement of the noise pattern in the digital camera, that will be later convolved with the Cricket noise pattern. Then, 1,000 images were taken with the Cricket operating at minimum gain. The noise pattern on the image intensifier follows an exponential distribution, as can be expected from thermal, spontaneous emission. This exponential noise distribution will be convoluted with the CCD Gaussian read noise profile, as can be seen in Figure 3-9.

3.7.3 A New DAQ

With the introduction of an entirely different image noise profile, the Data Acquisition (DAQ) needed to be remastered. In the traditional DMTPC DAQ software, the camera is exposed for periods of one second or longer, to be later stitched together with the CSP and PMT waveforms [80]. However, the intensifier noise beyond 100 ms would erode any capability for track detection, requiring much shorter exposure

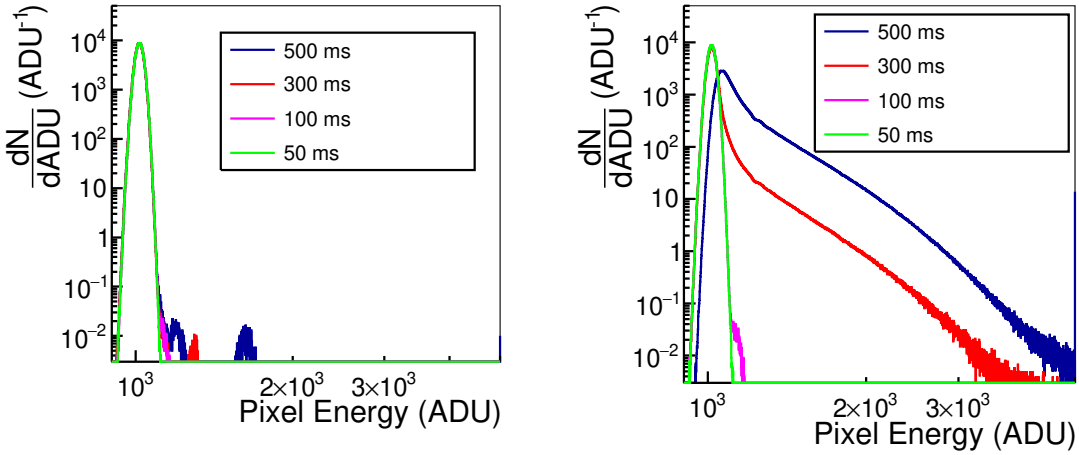

(a) (b)

Figure 3-9: (a) Noise profile for the Finger Lakes Instruments (FLI^{TM}) MLx285 Microline CCD camera. These images were taken with all voltages off to the TPC as well as all voltages to the Cricket Image Intensifier. The read noise can be considered as the 50ms green curve, while the increased noise at higher exposure settings are evidence of the dark noise. (b) Noise profile for the Cricket convolved with the CCD read noise. Image Intensifier convoluted with the FLI camera noise. It is clear that the 500 ms and 300 ms exposure settings add significant noise, while the additional noise from the 50 ms exposure was not noticeable compared to the CCD read noise.

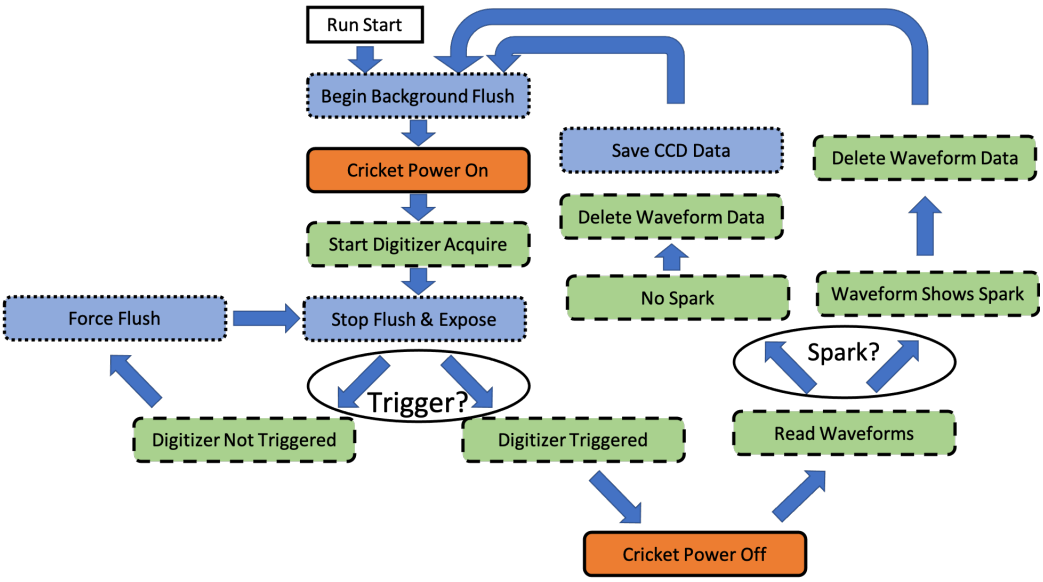

Figure 3-10: Chart depicting the re-imagined data acquisition algorithms. With the introduction of an image intensifier, shorter exposures were necessary in order to prevent dark noise building up on the CCD image.

settings. Second, with camera readout times on the order of 100s of milliseconds or longer, the detector would be down for CCD reading a significant percentage of the time, reducing the overall effective intrinsic efficiency of detection. Finally, with exposures of 50ms, significant amounts of data would need to be analyzed and stored in relatively short data runs. With all of this in mind, a program was written to continually flush the CCD until the digitizer triggered on either a PMT or CSP pulse. When the digitizer triggers an event, the algorithm switches into a different loop, where the Cricket intensifier is immediately turned off in order to prevent noise buildup during the readout process. With the intensifier powered down, sparks and additional events will be missed. With the Cricket powered down, the algorithm first confirms whether the event was a spark by comparing the integrated PMT waveform with a spark threshold derived from previous calibrations. If the triggered event was a spark, the algorithm immediately begins flushing the digital camera, deletes the waveform data, and restarts the acquisition. If the triggered event does not meet the spark threshold, the image data, waveform data, and times are all recorded into a ROOT tree structure.

Most of these processes overlap with the CCD exposure, even at short exposures. For the optimal run parameters, the CCD exposure setting was kept at 50 ms, where the exposure would be canceled to flush the chip again if the digitizer is not triggered. This creates an almost continual loop of flushing until the digitizer

is triggered. However, the C++ software calls to the digitizer and CCD occur on a timescale of microseconds, depending on the speed of the computer. As such, initial testing of this algorithm showed an approximate 90% detector dead time, with only 10% recorded events from what is expected in simulations. As such, an artificial delay was imposed on the algorithm after the exposure is started in order to increase the percentage of time available for an event to occur.

3.8 Data Analysis Conclusion

This detector produces three streams of data all related to the position, direction, energy, and time of a fast-neutron induced nuclear recoil. The algorithms written in this course of work demonstrate the capability of transitioning from a laboratory scale equipment to a one-person portable package. The latest upgrades from a Scientific CCD to lower power image intensifier coupled with a standard digital camera encourage a software trigger, only pulling data from the CCD when the charge and PMT channels are triggered. This greatly reduces the analysis and storage load on the system. Further, the image analysis algorithms demonstrate that the image can be rapidly compressed by two orders of magnitude, from millions of pixel values to hundreds, all within the nature of digital camera readout. Finally, combining the streams of data improves the resolution compared to any one system by itself.

Chapter 4

Investigations on Gain Improvements Using a Triple Mesh Avalanche

4.1 Introduction

As discussed in previous chapters, in order to enable the design of a portable device, the single electron gain should be maximized to support transitioning from an Electron Multiplying Charge Coupled Device (CCD) to a standard, astrophotography CCD or Intensified CCD setup. One method to accomplish the maximum possible gain is an idea discovered by the Dark Matter Time Projection Chamber (DMTPC) collaboration in which the team witnessed 1×10^6 single electron gain in gamma interactions by building a triple mesh, with one being held at ground, one at an intermediate high voltage, and the third mesh at higher voltage [46, 49]. This creates two avalanche regions, allowing for a boost in gain. This chapter is dedicated to understanding the mechanisms, applicability, experimental testing, and limitations of this signal amplification.

4.2 Background

In order to build a compact, portable detector, the single electron gain in the avalanche must be high enough to allow a portable imaging system. EMCCD cameras are bulky and require extensive amounts of power. In addition to a high gain, the electron avalanche has to occur over a relatively short distance with little diffusion, as the light needs to be focused onto as few pixels as possible. If the avalanche occurs over an extended distance, the camera will be out of focus for a large portion of avalanche

region and subsequently the scintillation light, projecting the unfocused light on a larger number of pixels. Also, if the track diffuses excessively, the scintillation light will again be smeared across a large number of pixels. Previous versions of this detector with comparable gas mixtures used EMCCD cameras with pixel-to-pixel read noise levels at fractions of an electron. While this worked well for testing the validity of the detector concept for nuclear security, a portable detector will have a camera that is much smaller, lighter, and less power hungry. As such, boosting the electron gain in the avalanche region is one possible route to achieving a one-person portable detector.

4.2.1 Electron Gain through Avalanche

Achieving electron multiplication through avalanche is an important process in this detector technology. Achieving the maximum possible gain, the limitations and the uncertainties of this process are key to making claims to energy resolution, directional resolution, and position resolution. However, simulating enough single electron avalanches for statistical significance at gain levels considered for this detector is not feasible. The goal is to operate as close to breakdown as possible, implying gain levels on the order of 10^5, which is the result of many hundreds of interactions per electron produced. Further, the avalanche gain follows a Polya distribution. In order to understand the average behavior of track, thousands of avalanches would need to be simulated. This would require a simulation covering approximately 10^{10} interactions per postulated setup (double mesh at varying gap distances and triple meshes at varying gap distances and voltages). A possible approach to future simulation work could be a computational fluid dynamics simulation, with similar work being completed for other detectors with different gas mixtures [81]. For the extent of this research, simulations were only conducted at significantly lower gain values to understand the behavior of the electron swarm in a triple mesh setup and build an empirical idea of describing the behavior.

Electron avalanche can be understood through a drift-diffusion model with knowledge of the Townsend and attachment coefficients. The Townsend coefficient, α, is the inverse of the mean distance traveled by a drifting electron before ionizing another atom or molecule [82]. The Townsend coefficient accounts for elastic scattering as well, which alters the distance before ionizing. The attachment coefficient, the equivalent of the Townsend but specifically for attachment, is typically regarded separately. Many studies combine the Townsend and the attachment coefficients to provide an

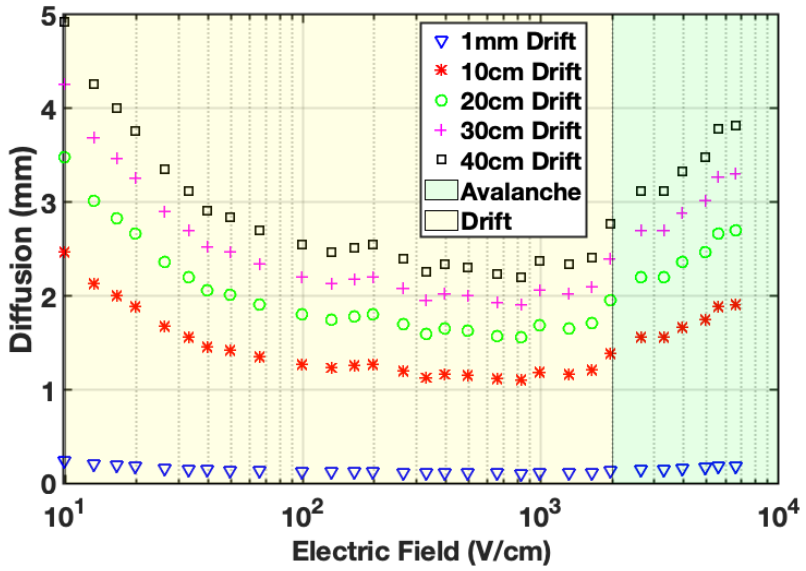

Figure 4-1: Track diffusion as a function of drift distance and electric field strength. This data is pulled from studies conducted by Pack, et al, and modified to display in this manner (diffusion versus electric field strength) [55]. This figure shows the electric field strengths required in the drift region, while also showing the increase in diffusion as tracks enter fields high enough to cause avalanche.

effective Townsend coefficient. In noble gases with no attachment cross section, the Townsend coefficient suffices. This coefficient alone can accurately predict the average avalanche size through Equation 2.10.

The diffusion along the drift, as well as diffusion within the avalanche, also plays a factor in understanding the number of photons per pixel. At high diffusion levels, the track will diffuse to the point that the scintillation light will be mapped to more pixels, causing the peak photons per pixel to drop below the noise characteristics of the camera, and the signal to be unreadable. However, at very low diffusion levels, and subsequently high drift electric fields, the minimal diffusion will increase the charge density entering the avalanche region, reducing the total achievable gain before discharge. As such, there is a balance for finding the optimal drift diffusion.

The diffusion in the avalanche is more significant than the diffusion in the drift field due to the higher frequency of collisions and higher energy involved in the collisions. This can be seen in Figure 4-1 in the right portion of the plot, highlighted in green. Even small drift distances, and hence diffusion, will eventually diffuse in the avalanche to the order of millimeters.

4.3 Limitations to Gain by Electron Avalanche

As can be seen from Equation 2.10, increasing either the distance of or the electric field in the avalanche region implies an increase the achievable electron gain. However, an upper limit exists where streamers begin to form, creating breakdown conditions. This upper limit becomes a function of the space charge buildup discussed in the remainder of this section. At shorter avalanche distances, the magnitude of the electric field is higher, reducing the likelihood of the streamer formation. However, at shorter distances and higher fields, breakdown becomes a function of manufacturing flaws and mesh wire radius resulting in Corona discharge building into a spark discharge. This requires distances on the order of hundreds of microns or greater.

4.3.1 Streamer Formation and Breakdown

The streamers are formed as a result of the electric field enhancement from the buildup of space charge. As the avalanche builds, the electrons are moving approximately an order of magnitude faster than the ions, creating a cloud of electrons cascading towards the anode and an essentially stationary trail of ions in the avalanche wake. This creates a dipole that opposes the electric field between the cloud of electrons and the trail of ions, as can be seen in Figure 4-2.

When this field approaches the magnitude of the external anode-to-ground mesh electric field, the electrons on the trailing edge see an effective neutral field. Quasi-neutral plasma conditions are formed, with any additional electrons moving into the avalanche region failing to avalanche and adding to the length of the quasi-neutral plasma. These conditions are known as a cathode-directed streamer, where in this case, the streamer is capable of quickly growing to form a conductive channel between the two meshes [59]. Previous studies have focused on breakdown conditions forming from single electron avalanche, where the accepted range of total avalanche before breakdown is known as the Loeb-Meek criteria and is typically accepted as 10^8 single electron gain [59]. In the case of single electron breakdown, the additional electrons feeding the streamer growth come from photoionization and secondary electrons liberated in ion-cathode bombardment. However, in the case of the Time Projection Chamber, a cloud of electrons are approaching the avalanche region, and this cloud will feed the streamer growth at a much lower total electron multiplication than single electron discharge.

When the track's peak electron density combined with the single electron avalanche gain approach the Loeb-Meek criteria, 10^8, the detector becomes unstable to electric

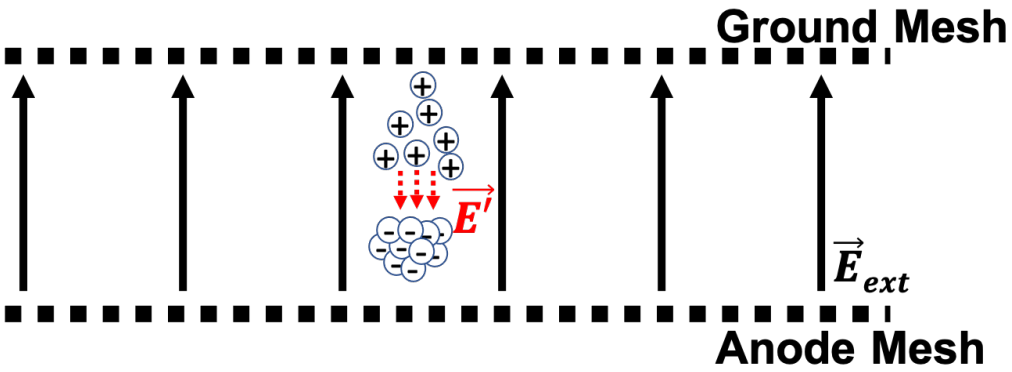

Figure 4-2: Dipole created between drifting electrons in the electron avalanche and the quasi-stationary counter-drifting ions. Electrons are drifting approximately an order of magnitude faster than the ions, causing a separation of charge between the head of the avalanche and the trail of ions. The electric field resulting from this dipole opposes the external field when near the center. When the cloud of electrons grows large enough, the space-charge induced field approaches the order of magnitude of the external field, creating conditions for a quasi-neutral plasma and streamer formation. This is a cartoon pictograph recreated from "Gas Discharge Physics" to be further used and adjusted in the upcoming sections [59].

discharge. This is not an exact number since the fluctuation in peak electron density depends on a variety of conditions, including primarily the recoil particle (^{4}He, ^{12}C, or ^{19}F in this case), track pitch, and track diffusion. Achieving the maximum possible gain for helium will imply breakdown conditions for the rare case of a carbon or fluorine recoil. Further, referencing the linear electron density of Figure 2-4, higher gain should be achievable in lower pressures since the electron density entering the avalanche region is lower. This predicts an approximately 50% difference between operating at 300 Torr and 600 Torr.

One possible modification discovered by the DMTPC collaboration is to add a middle mesh that will absorb a portion of the electrons in the avalanche and neutralize a portion of the counter-drifting ions, reducing the magnitude of the dipole and allowing the avalanche to achieve higher levels of gain. Of note to this strategy, the scintillating ion scintillates on the order or 15 ns, significantly faster than the ion will counter drift to the middle mesh to pick up an electron. As such, even the ions that neutralize on the middle mesh will produce a useful optical signal to the detector.

4.3.2 Manufacturing Flaws and Corona Discharge

At the other end of the spectrum, as the distance is decreased, the avalanche region can be operated at a higher field and theoretically achieve higher total gain prior to reaching the magnitude of the external field, and hence streamer formation. However, as the distance continues to shorten and the electric field continues to increase, manufacturing flaws begin to drive the breakdown conditions. Two manufacturing flaws dominate this process: 1) an imperfect mesh tension, causing small sections of the mesh to sag under the electrostatic load, and 2) microscopic jagged wire ends protruding from the glue on the edges of the mesh rings.

In the case of the imperfect mesh tension, a section of the mesh that has a reduction in tension becomes a location of systematic discharge while sagging under electrostatic load. When the mesh sags and the two meshes are very close together, the fractional difference between the sagging section and the rest of the mesh become significant, reducing any achievable gain in a majority of the region.

More concerning than the mesh sagging and more difficult to fix are the thousands of microscopic wires remaining after the mesh is trimmed around the outer edges of the avalanche region. In addition to the outer edges, any fray or wire imperfection poses the risk of sharp edges. Any of these sharp edges become a contributing factor when the avalanche distance is short and the electric field is high. The sharp edges introduce the possibility of corona discharge followed immediately by mesh discharge. After attempting avalanche in gaps shorter than 400 microns, the erratic spark behavior gave empirical evidence that 400 microns was the minimal achievable gap distance.

4.3.3 Mesh Transparency

As discussed previously, the gain in this detector relies on the theory of electron avalanche. After the helium-nucleus recoils and liberates a track of electrons, these electrons drift to the amplification region. After passing the grounded mesh, the electrons enter the amplification region, where the electric field abruptly increases from approximately $200\frac{\mathrm{V}}{\mathrm{cm}}$ to $15\frac{\mathrm{kV}}{\mathrm{cm}}$. The magnitude of this latter electric field is strong enough that the avalanche field lines extend well beyond the ground mesh and into the drift region. As such, an overwhelming majority of these electrons bypass the grounded mesh by drifting along the avalanche lines and around the ground mesh wires. Once the electrons reach this higher field region, electron avalanche and therefore electron multiplication begins.

This is a direct correlation to Frisch grid transparency. Several studies, dating

back to the 1980s and as recent as 2015, have focused on an accurate model of the transparency of a Frisch grid [83, 84]. Bunemann developed a theoretical framework that predicts the percentage of electrons absorbed on the ground wires in ionization chambers by computing the number of field lines that terminate on the wires, coined "grid loss" by Bunemann. The result of this research is summarized by Equation 4.1, where λ is the grid loss, ρ is a function of the wire geometry given by Equation 4.2, and E_A and E_D are the electric field in the avalanche and drift regions respectively. In Equation 4.2, r represents the wire geometry and d represents the wire spacing.

$$\lambda = \frac{E_A - E_D}{\pi E_D}\left\{\sqrt{(\frac{E_A + E_D}{E_A - E_D}\rho)^2 - 1} - cos^{-1}(\frac{E_A - E_D}{E_A + E_D}\frac{1}{\rho})\right\} \tag{4.1}$$

$$\rho = \frac{2\pi r}{d} \tag{4.2}$$

Bevilacqua, et. al., took this one step further in 2015 to factor in a difference between parallel wire Frisch Grids to a grid mesh structure, as are used in this detector [84]. This work simply doubles the wire density, or halves the distance between wires, to achieve close agreement with data while still using the results from Bunemann. Building on this understanding, a middle mesh can be added to intentionally absorb a portion of the electrons in the avalanche and neutralize some of the counter-drifting ions in order to boost to a higher gain before reaching breakdown conditions. As discussed previously, the higher the number of electrons in the head of the avalanche, the higher the magnitude of the space charge dipole, and eventually quasi-neutral plasma conditions form. The middle mesh reduces the number of electrons by absorption in the developing head of the avalanche, allowing boosting to higher gain prior to the dipole reaching the magnitude of the external field. In order to absorb the maximum number of charge, the electric field in the second avalanche region (after the middle mesh) must be lower than the electric field in the first avalanche region (prior to the middle mesh), but still within the strength to create avalanche conditions. The experiment discussed in this chapter is specifically targeted to understand the limitations of the triple mesh setup.

4.4 Simulations in Garfield++

Although the magnitude of avalanche gain in this detector is well out of reach for any extended amount of simulations, Garfield++ simulations were used to investigate the behavior of the avalanche when adding a third mesh. Garfield++ is a simulation

written in C++ that builds a two dimensional mesh for the electric field, assumes a uniform field into the third dimension, and tracks charged particles along the drift lines during drifting and avalanche [56].

The driving factor for achieving maximum gain is the electron density at the anode wire, since it is this location that will first develop a streamer leading to electric breakdown and discharge. The linear density of an avalanche can be plotted as a function of position in the drift/avalanche direction, where the location of wires are clearly seen as the sole peak in the density distribution. In this simulation, the creation point of an ion in the avalanche direction was logged, as seen in Figure 4-4. If an arbitrary line is selected that represents a desired maximum density, a dual mesh setup (ground and anode) is not able to achieve any higher gain due to this maximum density threshold. However, if a third mesh is added to the setup, some of the electrons can continue into the second avalanche region to undergo further avalanche. These electrons avalanche at a heavily reduced rate in the second region because the number of electrons entering the second region is significantly higher. This is also shown in Figure 4-4.

These simulations indicate that the electric field magnitude in the second region will be considerably lower than the first region, by a factor of approximately 2.5. The first set of simulations, with only two meshes, operated at an electric field strength of 11.8 kV/cm, resulting in a total gain of approximately 2,200. One hundred avalanches were simulated, taking the average density in the avalanche direction across the entire simulation. An arbitrary maximum density was selected at the peak of the average density to determine a triple mesh setup that would improve the total gain but remain below the threshold. The second simulation kept the first region at the same electric field strength, but added a second avalanche region of approximately 4.5 kV/cm. With the second simulation, only ten avalanches were averaged due to computational time, but resulting in an average gain of 2,900, indicating an approximate 30% boost in gain while remaining below the arbitrary threshold.

In addition to the density along the avalanche direction, the diffusion in the orthogonal plane was also studied. If the triple mesh causes any additional diffusion in the amplification plane, the additional boost in gain will likely occur below the threshold of the camera noise, resulting in no significant gain. This can be seen when comparing a two mesh to three mesh setup, where the density of ion creation points is plotted on a two dimensional plot in the avalanche direction and a perpendicular direction. As seen in Figure 4-4, the width of the avalanche does not grow appreciably from one mesh to two meshes, indicating that the pixel-to-pixel signal to noise will

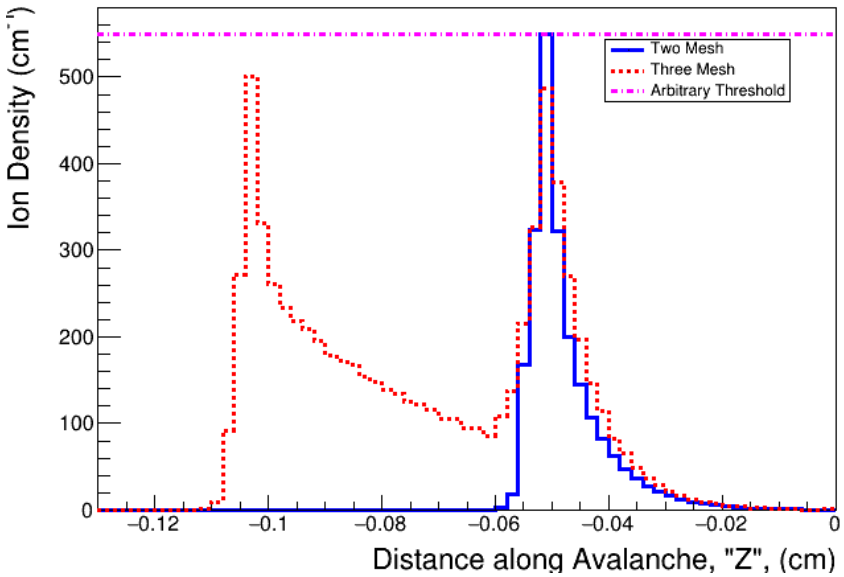

Figure 4-3: The linear density of electron impact ionization as a function of depth into the avalanche region. The electrons start at $z = 0$cm and avalanche in the negative Z-direction. Every time an electron ionizes an atom or molecule, the location is tagged and added to the histogram. Integrating each curve provides the total gain. The blue curve depicts a two-mesh setup with only one avalanche region. Choosing an arbitrary maximum density of the peak of the two-mesh avalanche, the dotted curve shows adding a second reduced-avalanche region gives the possibility to boost the gain by as much as 30% while remaining below the threshold. In reality, the threshold is a function of recoil track density entering the avalanche region and the Loeb-Meek criteria of approximately 10^8 total electrons.

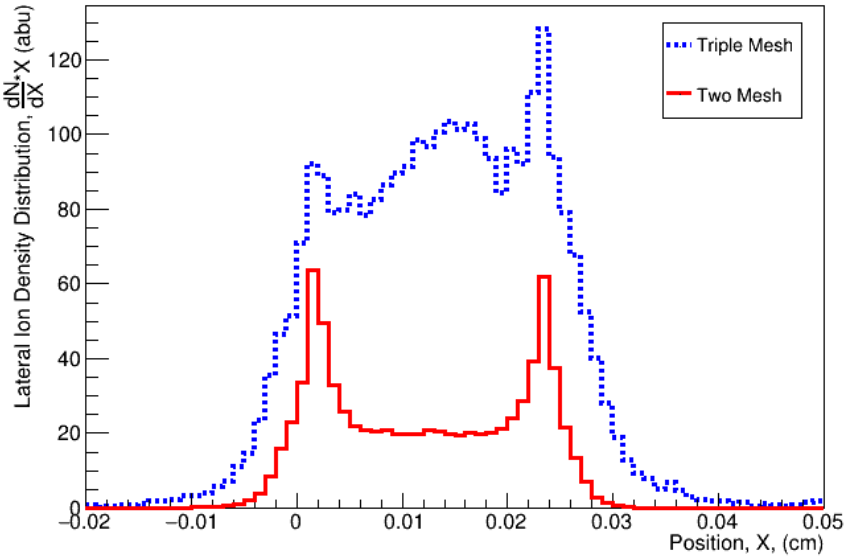

Figure 4-4: The lateral ion point-of-creation distribution compared between a two mesh avalanche setup and a triple mesh setup. This plot shows that an increased percentage of the avalanche occurs between the mesh wires (seen as peaks in the red nd blue curves), while the majority of the two mesh ions are created in the vicinity of the wires.

improve with the addition of the third mesh. Referring back to Figure 4-2, adding another mesh will pull some portion of the electrons through to the second avalanche region, reducing the density in the head of the avalanche, and thereby reducing the likelihood of streamer formation.

4.5 Experimental Materials and Methods

In order to test a triple mesh setup with conditions comparable to the operating conditions of this experiment, a miniature field cage was constructed out of low off-gas acetyl plastic, copper rings, and stainless steel mesh, as depicted in Figure 4-5. A low activity alpha source, collimated to further reduce the event rate, was placed between the field cage rings. The detector was operated in charge/PMT readout mode, with no imaging taking place. An overwhelming majority of this data was operated at such a low gain that the images would have been void of any data.

The alpha source was a 0.9 μCi ^{241}Am source pulled from a common household smoke detector. There was a thin layer of gold foil covering the alpha source, causing range and energy straggling. A two channel, 8 bit, 250MHz Alazartech ATS860

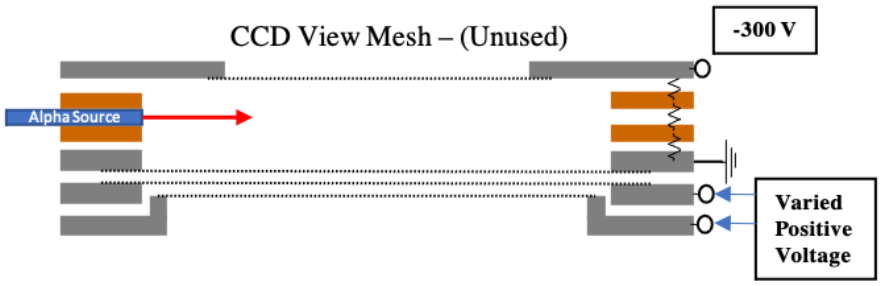

Figure 4-5: A miniature version of the full scale field cage to test the triple mesh configuration and compare with the two mesh setup. The cathode plate and mesh were connected to a negative voltage DC power supply, typically at -300 V, while the two anode meshes were connected to positive high voltage power supplies. An $^{2}41$Am alpha source was placed between the two copper field cage rings, with a collimated acetyl plastic housing.

digitizer was used to collect charge data from either of a Cremat Charge Sensitive Preamplifier or a Ludlow 3.5 inch Photomultiplier Tube. For additional details on the alpha source, energy spectrum measurement, and digitizer calibrations, see Appendix A. The Cremat CSP 113 preamplifiers were connected to the middle mesh or the third mesh depending on the particular run. When the first field was high and the second field very low, the charge cloud was nearly fully absorbed on the middle mesh, causing much of the signal to be lost on the third mesh. In this scenario, the middle mesh became opaque to signals measured on the third mesh. In a two mesh setup, the preamplifier was connected exclusively to the second mesh.

With this setup, gain curves were constructed with only two meshes in the read-out region, to confirm the agreement with the theoretical Townsend and attachment coefficients. The detector was operated at 300 Torr and 600 Torr. Additionally, the distance between the ground mesh and anode mesh was varied to investigate the optimal avalanche distance. As discussed earlier, the minimum distance was kept above the distance of concern for manufacturing flaws to plague the setup. Data was collected at an electric field magnitude just strong enough to provide measurable data points on the charge readout, and then increased at potential differences of 20 V until a spark rate of one spark approximately every 30 seconds was measured. Since a spark causes a 1-2 second dead time for multiple reasons (Residual Burn-in discussed in [50] and re-charging the two mesh equivalent capacitor), one spark every 30 seconds was

considered the maximum achievable gain.

At each voltage setting, an energy spectrum was constructed using the waveform peak of the CSP, which can then be converted into the total number of electrons created in the avalanche. The CSPs used varied depending on the gain setting, but the gain settings were anywhere from 1.4 peak volts in the waveform of a CSP 110 per picoCoulomb of charge generated all the way down to 1.3 mV in the peak for a CSP 113 and equivalent picoCoulomb of charge. Since the majority of the alpha recoils were transiting the entire distance across the field cage, a simulation was conducted in Garfield to produce the expected number of electrons deposited in the drift region given the alpha calibration source energy spectrum. This curve was fit to the measured energy spectrum with a single scaling variable: the single electron gain. These gain values are plotted in Figures 4-6(a) and 4-6(b).

The relationship between the Townsend coefficient and the electric field is approximately linear in the range of fields considered in this text. As such, the relationship between the potential difference and the total gain is exponential, as can be seen in Figure 4-6(a). In this figure, the maximum achievable gain can be seen by the red "X" at the upper portion of the curve. In Figure 4-6(b), an almost 50% reduction in maximum achievable gain is seen. As discussed earlier, this is related to the reduction in field to achieve the comparable gain levels. When the distance is double between the two meshes, the electric field required to achieve breakdown conditions is reduced by approximately half, causing the number of electrons in the head of the avalanche to achieve breakdown conditions at approximately half the gain levels.

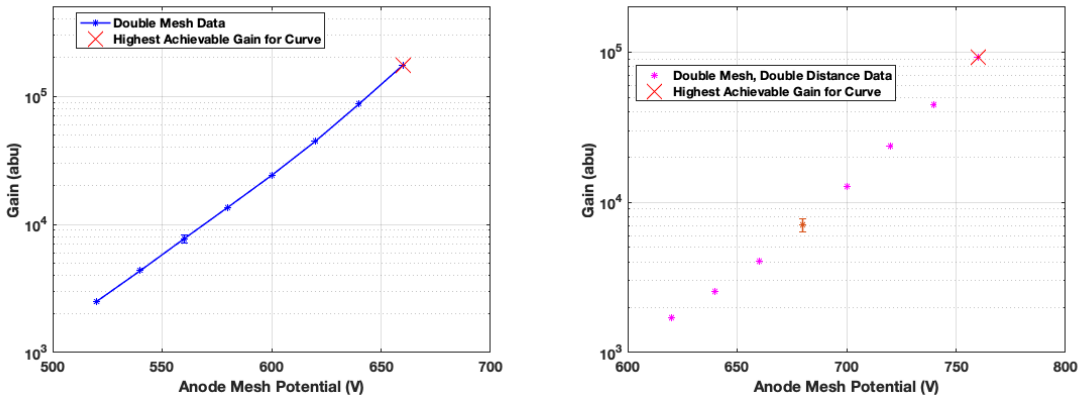

(a) (b)

Figure 4-6: (a) A gain curve produced by operating the miniature field cage setup with a two mesh avalanche held at varies electric field strengths (ordinate) and measuring the single electron gain as a result. The relationship between the field strength and the Townsend coefficient is approximately linear in this regime, resulting in an exponential relationship between the gain and the anode potential. (b) The same gain curve with double the distance between the ground mesh and anode mesh. This curve was constructed to illustrate that increasing the distance alone results in a lower total achievable gain, as discussed in Section 4.5

4.6 Experimental Results and Discussion

Building on the discussion of linear electron density in an alpha recoil from Chapter 2, the simulations earlier in this chapter, and the discussion of maximum achievable electron number from the Loeb-Meek theorem discussed earlier in this chapter, a modest expectation of boost in gain is expected from the triple mesh. The peak linear electron density at 300 Torr is approximately $10^3 \frac{N_e}{mm}$, giving an estimated 10^5 total gain prior to reaching the Loeb-Meek criteria. This can be seen in Figure 4-6(a), with the red "X" indicating the point of breakdown. Boosting the total gain above this number would indicate the triple mesh as a successful method of achieving single-stage gain higher than the Loeb-Meek theoretical limit.

If the same setup as Figure 4-6(b) is constructed with a middle mesh, the gain exceeds the gain levels of the dual mesh setup at 500 micron spacing and 1 mm spacing. This can be seen in Figure 4-7. In this set of data collection runs, a triple mesh set-up was used and the voltages on both the middle and the third mesh were varied. The data is overlaid on the 500 micron spacing dual mesh setup for easy comparison between the two outcomes. In the vertical line at 600 Volts middle mesh potential, the third mesh voltage was varied from 200 volts up to 760 V, resulting in

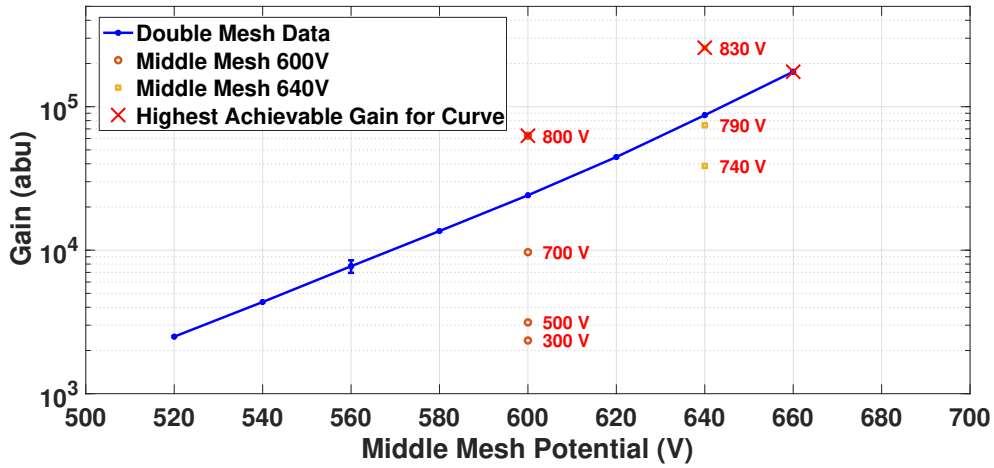

Figure 4-7: A comparison of double versus triple mesh setups across several different run parameters. The blue curve represents the same curve as the data reported in the two mesh gain curve in Figure 4-6(a). In this figure, the triple mesh data, with varying middle and third mesh voltages, is overlaid on the two mesh data. The text to the right of each data point in the vertical bands of data indicate the potential on the third mesh. The middle mesh was held at 600 V for one series of runs and at 640 V at another series of runs, creating the two vertical bands of data points. The third mesh was increased until reaching one breakdown every thirty seconds, as in the two mesh data runs. The optimal conditions are reached when the middle mesh is just below the maximum voltage for the two mesh setup, and the third mesh at 830 V, creating a significantly reduced electric field strength for the second region. This is also in agreement with the lower gain simulations conducted in Garfield++ and discussed in previous sections.

a boost above the dual mesh setup at a similar anode potential. Another data run held the middle mesh at 640 volts while varying the third mesh from 740 volts up to 800 V, resulting in the maximum achievable gain for a triple mesh setup at 300 Torr, approximately 47% boost in gain over the equivalent two mesh setup.

4.6.1 Limitations and Stability

While the triple mesh provided a boost in single electron gain while collecting charge and PMT data, the CCD was later operated in conjunction with the charge and PMT data at higher gain settings. During one of the data collection runs, it was observed that the electric breakdown seemed to transition to a state of a steady plasma with a significant after glow. When running with a two mesh setup, breakdown occurs well within the confines of a single camera exposure, allowing the voltage across the capacitor to rebuild in a few seconds and resume normal operations. However, with

the triple mesh setup, the discharge glowed for multiple seconds before returning to normal operational status, more than doubling the downtime for every spark.

This undesirable feature is assumed to be a function of the reduced charge density, resulting in a significant reduction in conductivity of the quasi-neutral plasma. Further, the secondary electron emission from the middle mesh can slowly feed the plasma, where a large number of ions contact the middle mesh during the counter drift, with a portion causing the emission of an electron into the second avalanche region. This is also occurring in the two mesh setup, but an overwhelming majority of the ions are created immediately adjacent the anode mesh and do not contact the cathode mesh until the electrons are fully absorbed on the anode mesh and the dipole is no longer present. With a triple mesh setup, at gain settings approaching the Loeb-Meek criteria, a large number of ions are created just "downstream" of the middle mesh, causing secondary electron emission almost simultaneously to the avalanche in the second region. As a result of these two features, the limiting factor becomes a glow discharge with a lower light output but significantly longer time to discharge the two meshes. The data collected with the CCD gave evidence that the steady plasma was stable for several seconds, indicated by a glow in the image.

4.7 Gain Improvements Conclusion

The triple mesh setup offers an opportunity to boost above the physical limit described by the Loeb-Meek criteria. For heavy charged particles such as alphas, the linear electron density becomes the deciding factor in determining the maximum achievable gain at various pressure settings. This research showed a 47% boost over comparable two mesh setups, in a variety of avalanche distances and electric field strengths. However, the nature of discharge changed from a rapid discharge between the two meshes to that of a several-second quasi-stable plasma formation with an ensuing glow. This several second instability was undesirable when operating a radiation detector due to the resulting extended dead time. But this quasi-stable, quasi-neutral plasma may offer an interesting opportunity for studying the behavior of plasma in other fields of research.

Chapter 5

Detector Background Studies

A portable Time Projection Chamber is a powerful tool for emergency first responders, border security personnel, and military personnel due to the high rejection rate of gamma ray interactions and full solid angle coverage for direction estimates. However, the detector is not free of background signals entirely. Backgrounds can arise from extremely high energy cosmic gamma interactions, alpha contamination in the detector construction material, and cosmic-created neutrons. The two primary contributing sources of background in a detector of this nature are both derived from cosmic neutrons: direct cosmic-shower neutrons and "ship effect" neutrons. While there are other possible backgrounds, such as muon-induced spallation neutrons, these rates are low enough that they will not contribute significantly to the event rate and are therefore not presented in this work. These top four contributing background signals are discussed in this chapter, and the two primary backgrounds are studied over an extended data run discussed in the second half of this chapter.

5.1 Gamma Ray Rejection

The dominant reaction of a gamma ray with this detector are interactions with the inner portions of the vacuum chamber walls of the detector and the copper rings, creating a high energy electron recoiling through the drift gas. Depending on the energy of the incident gamma radiation, the reaction could be the photoelectric effect, Compton scattering, or pair production. Due to the medium atomic number of the construction material, Compton scattering will likely dominate. The recoiling electrons will leave a track of free electrons with a linear electron density that is significantly lower than the typical alpha recoil tracks. As such, most of these tracks

will be invisible to the track detection algorithms due to the inherent noise of the imaging system. For incredibly high energy cosmic gamma radiation that creates electron recoils on the order of 100s of MeV, the linear energy density of the recoiling electron will be high enough to register a track in the digital imaging system. These events will be predominantly rejected due to an image threshold cut since the electron will traverse the entire diameter of the TPC. However, it is possible that the track detection algorithms will capture a portion of the track, coupled with the full energy of the entire track across the TPC in the CSP or PMT readout, being recorded as a much shorter track than the actual electron recoil. These events will be rare events but will add noise to the direction finding algorithms discussed in Chapter 7.

5.2 Alpha Sources in Construction Material

With most metal construction material, trace amounts of alpha-producing radioactive elements may be present as a contaminant. This detector was primarily constructed out of low cost materials, including standard copper gaskets, aluminum for the vacuum chamber vessel, and lead-solder to hold the field cage resistor chain connected. This material was chosen to keep the cost down as well as the knowledge that background radiation originating from the detector construction material can be removed through a image threshold, cut-based approach. As long as the rate of background alpha contamination is low, the signal does not restrict the operation of the detector in any way.

For the aluminum vacuum chamber and the copper field cage rings, the dominant background radiation is expected to be ^{2}32Thorium and ^{2}26Radon, likely present in trace amounts. Activities as high as approximately 19 Bq kg^{-1} have been reported in aluminum oxide from the Egyptian Mining Company [85], giving an upper bound. ^{2}32Thorium produces six alpha particles in a decay chain that takes several days once initiated [86]. However, only the inner most 25 μm will allow a 5.5 MeV alpha to penetrate the active volume. Further, assuming the alphas are created isotropically, the majority are emitted in a direction incapable of penetrating the inner volume. Most alpha particles emitted from the walls will not reach the active volume due to the lower energy after passing through the wall material. Finally, the alpha sources from the construction materials surviving to the active volume can largely be rejected due to the location of the start of the track as reported by the digital camera. In other words, if the edge of the track crosses the threshold, the event is automatically rejected as a background. This will fully remove any alpha recoils originating from

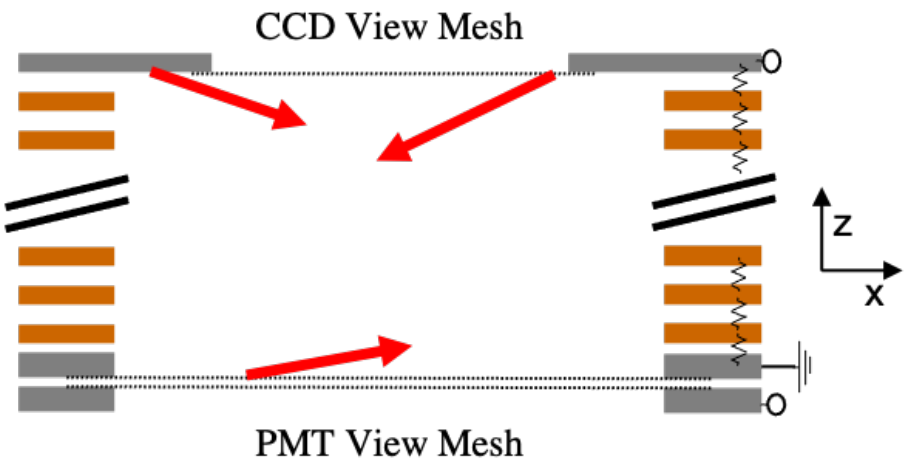

Figure 5-1: Possible source locations for alpha background from construction material that are currently incapable of being rejected as background events. The red arrows in this image depict the only three locations where alphas originating from the construction material are incapable of being rejected due to the location within the vessel. The field cage was shortened for the image. As future detectors improve the accuracy in reconstructing the position along the cylindrical axis, these events can be rejected due to originating on either the ground mesh or the cathode.

the radial direction, such as the cylindrical walls of the detector, the field cage rings, or the acetyl construction material.

However, alphas that originate on either the cathode mesh, cathode ring, or the ground mesh in the amplification region will not be capable of differentiating between source signal versus background through the digital image alone. This is depicted in Figure 5-1, where the alpha track does not cross an image threshold. The amount of material available for alpha particles originating in these locations is kept very minimal since the mesh is a fine stainless steel mesh with 100 wires per inch, each of diameter 30.5 μm, resulting in approximately 18.2 g of stainless steel for each mesh in the active volume region. In future detectors, if the position along the cylindrical axis, referred to in this work as the "Z" direction, is improved to within millimeters, any alphas originating at the amplification mesh or the cathode mesh can also be rejected by start position. Even with conservative estimates of Thorium contamination in stainless steel, the rate of alphas from the meshes is 2-3 orders of magnitude lower than alphas generated by cosmic-related neutrons.

The resistor chain with a touch of solder connecting each resister poses another source of background radiation through the $^{2}10$Pb contamination in the lead. Previous studies have showed between 0.4 and 13 alpha decays per minute per cm^2 [87].

An interesting observation was made when studying the difference between AmBe source data runs and background, no source data runs. The presence of an AmBe neutron source created a higher rate of ion recoil in the gas in the vicinity of lead than previously measured. This is expected to result from inelastic (n,α) and (n,p) reactions in the high-Z, lead components of the solder. However, not enough data was collected to be statistically significant. As such, this observation will be left for future studies and the section of the detector with the soldered chain of resistors will be removed from the active volume through an image threshold cut.

5.3 Direct Cosmic and "Ship Effect" Neutrons

Neutrons originating from cosmic ray interactions with the upper atmosphere effect the detector in one of two ways: 1) primary and secondary neutrons are created in a cosmic shower and directly interact via nuclear recoil in the target gas or 2) the same neutrons created in the cosmic shower interact with nearby high-Z material to create spallation neutrons. The former will be referred to as "direct" cosmic-shower background, although previous work indicate it is primarily composed of secondary neutrons created from a variety of interactions [88, 89]. The latter was discovered while conducting nuclear material search testing on ships at sea in the 1970s [90]. As such, it is commonly referred to as ship effect neutrons. Any large presence of high-Z, high density material will add to the background through spallation neutrons. Both of these signals have been studied extensively in the astro-particle physics and cargo nuclear security fields [90, 91]. The ability to differentiate signal from background when using the probabilistic back projection from Chapter 7 depends heavily on the rate of these cosmic-induced background neutrons.

5.3.1 Direct Cosmic Neutrons

The energy spectrum of direct, cosmic shower neutrons is given in Figure 5-2. The energy spectrum extends into very high energy, beyond what is plotted, but at an exceedingly low flux. Coupled with the steadily decreasing cross section for higher energy neutrons with ^{4}He, the calculations looked at cosmic neutrons up to an energy of 20 MeV. The angular distribution of neutrons fits closely to a function of $\frac{dN}{d\Theta} = \mathrm{a} + \mathrm{b}\cos^{2.7}\Theta$, where the coefficients "a" and "b" can be determined from differential flux and depth in the atmosphere while Θ represents the zenith angle [92]. In considering this angular flux extending to 120°and the nature of neutron forward

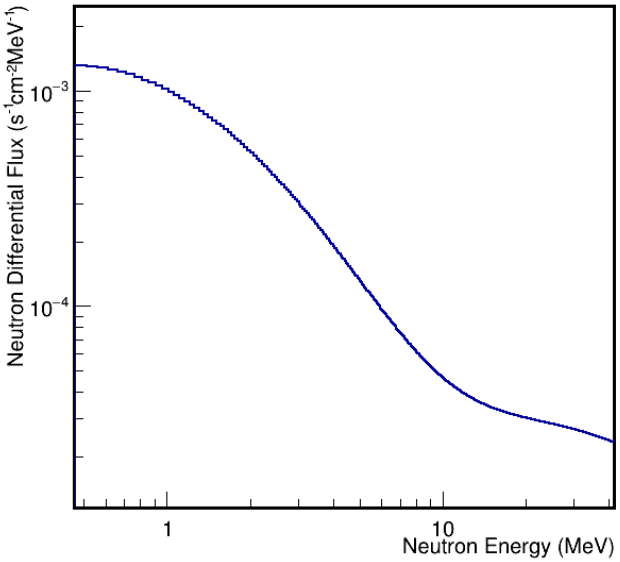

Figure 5-2: The differential cosmic neutron energy flux, reproduced by an empirical formula developed by Gordon *et al.* [93]

scattering of high energy neutrons, the angular distribution of recoil alpha particles resulting from direct cosmic-shower neutrons will be nearly isotropic. The alpha particles will not overwhelmingly point back towards the sky, although a very slight bias can be seen in a downward alpha particle recoil direction, discussed in the next section.

It is clear that the rate of neutrons passing through the detector from direct cosmic showers is not negligible. When using the probabilistic back projection, the hope is the direct atmospheric neutrons provide a signal that is essentially uniform across the 4π solid angle and ship-effect neutrons primarily point towards known high-Z or high density structures in the vicinity of the detector. The expected rate of direct atmospheric neutron-induced alpha recoils was calculated and presented in Appendix B and also simulated in Geant4 simulations for comparison with data.

5.3.2 Ship Effect Neutrons

Several studies have analyzed the rate and energy spectrum of ship effect neutrons in the proximity of higher density materials [88, 94]. A numerical calculation was performed to compute the average chord length and average solid angle for the higher density materials used in the detector materials: the aluminum vacuum/pressure chamber and the copper field cage rings. The average chord length for a neutron

produced in the copper rings and traversing the active volume was 9.5 cm with an average solid angle coverage of 13 %. The values for the aluminum chamber, extending a greater distance allowing for steeper transits through the cylindrical volume resulted in 11 cm and 23.6 % respectively. The flux averaged cross section given the energy spectrum of the ship effect neutrons and the ^{4}He elastic scattering cross section is 1.44 barns. From Kimura, the rate of ship effect neutrons from medium to high-Z material can be estimated by Equation 5.1 [95]. In this equation, A represents the atomic mass of the material. This results in a rate of ship effect neutrons in the construction material of 0.0024 n/s from the aluminum and 0.007 n/s from the copper field cage rings. Using the average chord length and the average solid angle coverage of the active volume, the ship effect rate from detector construction materials is 1.15×10^{-6} n/s for all major contributions of ship effect. This is less than one interaction in a typical extended cosmic data run.

$$G = e^{-(16.3 \pm .2)} A^{(1.8 \pm .06)} \tag{5.1}$$

For the extended background runs, the ship effect spallation neutrons from the surrounding building material will contribute to the recorded energy spectrum. The walls are made of Concrete Masonry Unit (CMUs). There are multiple concrete pillars within the lab space, as depicted in the next section in Figure 5-3. Further, all of this is likely full of iron reinforcing bars, considering this is the basement level of an industrial building. Unfortunately, the concrete is fully surrounding the detector, creating a nearly uniform distribution of spallation neutrons at a low rate surrounding the detector. Previous studies have shown the amount of ship effect neutrons to expect using Equation 5.1 [95]. As an example, 10 metric tons of concrete will produce approximately 15 neutrons per second, approximately isotropic.

5.4 Experimental Methods

An extended cosmic data run was completed with this detector after determining the optimal running conditions for a 1000 Torr, 90% ^{4}He and 10% CF_4 gas mixture with the Alta U6 CCD camera. The laboratory is located in the basement of a three story building. The building is an older industrial warehouse that has been converted to laboratory space for the university. The building is a standard structural steel construction with a brick exterior siding. The laboratory is almost perfectly centered between the outside walls of the building. However, the floors above the laboratory

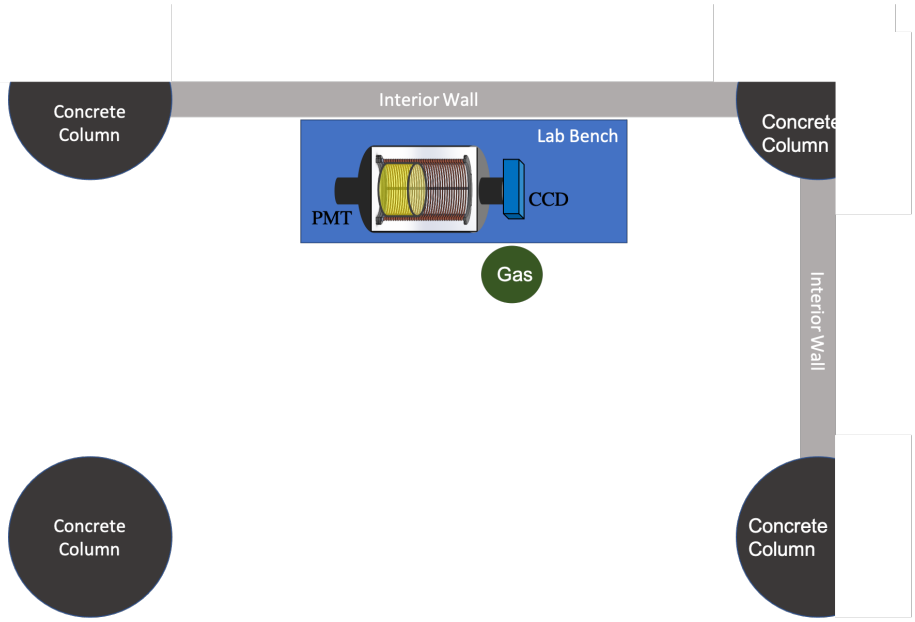

Figure 5-3: A depiction of the laboratory layout during the cosmic data run. There are four large concrete columns surrounding the experiment apparatus, with unknown amounts of steel in the form of I-beams or re-bar. The walls of the lab space are interior walls with wood studs covered with sheet rock. The gas cylinder, also depicted, was placed close enough to the detector that ship effect neutrons from the heavy steel cylinder may create a signal.

appear to have concrete construction, which implies a thin layer of steel beneath the concrete. The concrete is expected to be relatively thin since it is installed above the ground floor level. In addition to the three layers of concrete and steel above the lab, there are multiple structural columns located in the lab space, depicted in Figure 5-3. The run was conducted over the holiday break in December of 2020. The detector was operated remotely with a lower gain setting to preserve the gas gain. The lower gain results in a lower spark rate which is expected to prolong the life of the target gas in-between refills. The total detector live-time was approximately 20 hours.

5.5 Cosmic Data Results and Analysis

The cosmic data run resulted in a total of 312 events over a span of several days with approximately 20 hours of true detector live time, with 91 events surviving all cuts. This run was not conducted continuously, but over a span of days due to detector dead time between camera exposures and breaks between runs to confirm data prior to starting the next run. These events are the surviving tracks after an image threshold

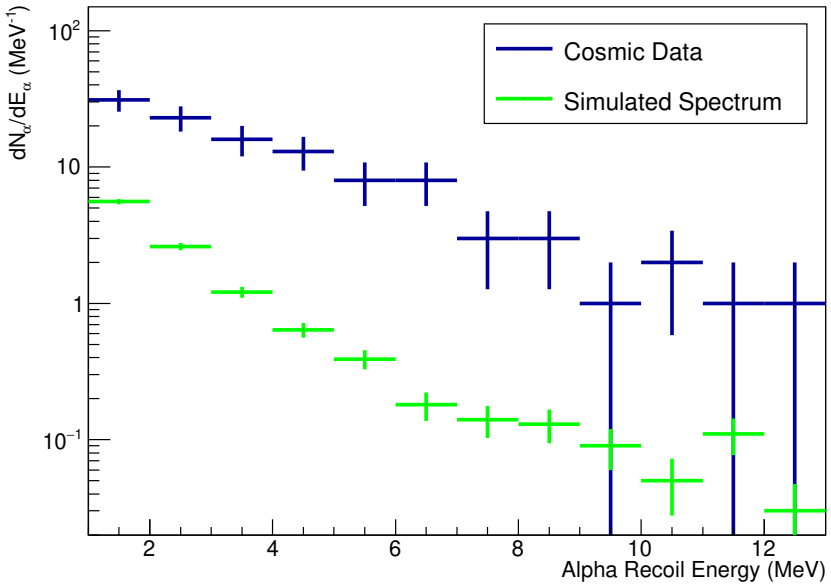

Figure 5-4: A comparison of the measured alpha recoil spectrum versus the simulated direct, cosmic-shower differential alpha recoil spectrum. This shows that the direct cosmic background is a contributing signal to the detector, but there is also a large contribution from spallation neutrons not accounted for in the the simulation as well as glancing collisions from neuron energies higher than 20 MeV. This measured curve serves as the benchmark background, where the ship effect neutrons are assumed to be also omni-directional since the detector is surrounded on all sides by concrete and steel from the building construction. Further, the energy spectrum is expected to be comparable to the direct cosmic shower neutrons.

cut to remove any alpha-decays in the chamber material. The energy distribution for the alpha recoils is given in Figure 5-4. The simulated curve used reference neutron differential energy spectra obtained from NYC at a medium sun activity, and were then corrected for different geomagnetic rigidity between Boston and NYC, as well as low sun activity in 2020 [93, 96–98]. The simulated rate extends up to 20 MeV neutrons, which implies a significant portion of the neutron background in the detector coming from high energy neutrons above 20 MeV. Another contributing factor to explain the difference between the measured rate and the simulated rate all indicate that the ship effect neutron is a contributing factor in the laboratory environment.

In addition to looking purely at the rate as a function of energy, the distribution of ranges can be plotted against the distribution of energies for the cosmic events, giving insight to the rate of alpha recoil versus ^{12}C or ^{19}F recoil. This can be seen in

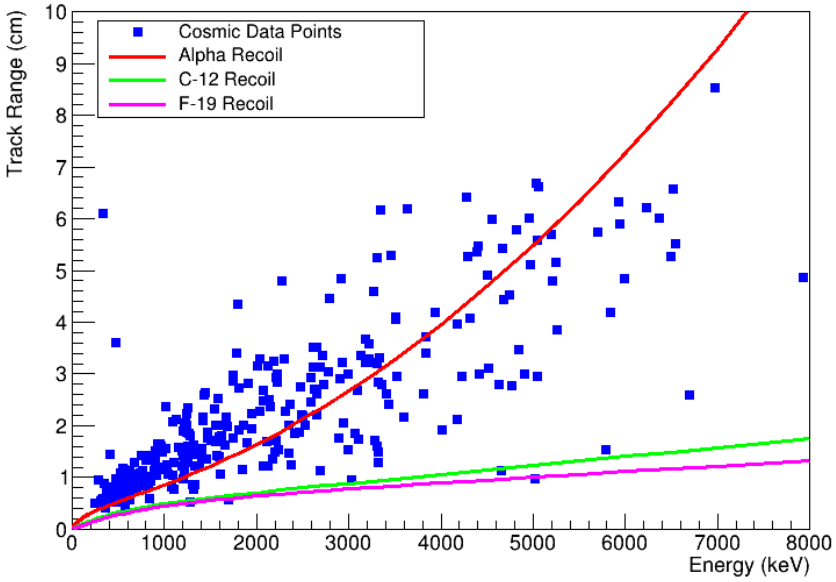

Figure 5-5: A comparison of the total range measured by the data analysis algorithms versus energy deposited across the 20-hour cosmic data run. The energy is the average between the PMT and CSP recorded energies. The PMT reported energy is the integral of the PMT waveform, with PMT calibrations discussed in Appendix A. The CSP reported energy is the maximum of the CSP waveform, also with calibrations discussed in Appendix A. It is apparent that the overwhelming majority of events are alpha recoil events. This plot also indicates an approximately 25% energy and equivalent range resolution.

Figure 5-5.

Finally, the angular distribution of alpha recoils is an important quantity since the goal of this detector is to use the alpha direction to build probabilistic models of neutron source locations. Unfortunately, as discussed earlier in this chapter, there is an extended range of cosmic neutron zenith angles as well as an extended tail into higher energies for direct cosmic neutrons. The higher energy neutrons favor forward scattering which results in alpha particles recoiling in angles across the 4π solid angle spectrum. This can be seen in the comparison between the simulated and actual angular double differential alpha recoil spectrum in Figure 5-7. However, the direct cosmic neutron angular spectrum is not expected to change with relatively small changes in position, resulting in a fairly uniform background signal that is unlikely to significantly impact the source location algorithms. Further, the ship effect neutron signal can be considered given the conditions of the data run.

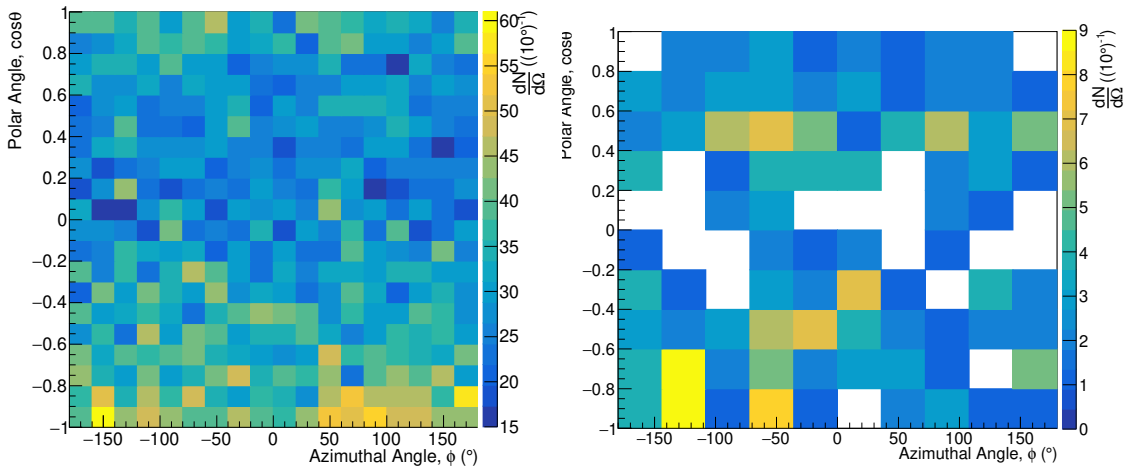

(a) (b)

Figure 5-6: (a) Simulated versus measured results for angular double differential spectrum of alpha recoil events for the cosmic-generated background as a function of azimuthal angle and polar angle. This shows a slight bias towards the downward direction for extended cosmic data runs. (b) Cosmic data from a 20-hour background run. The nearly isotropic nature of cosmic-related alpha recoils is evident.

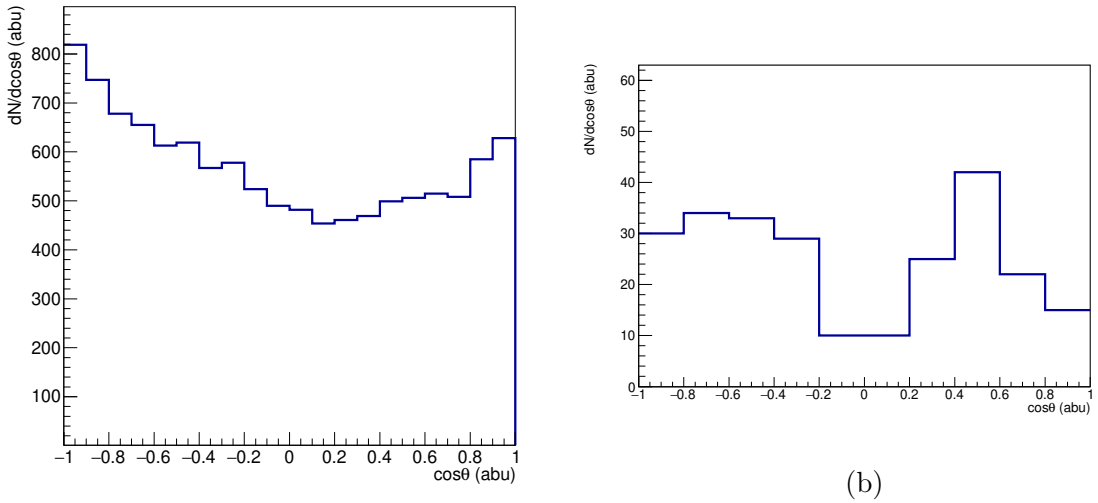

(a) (b)

Figure 5-7: (a) Simulated results of the alpha angular differential spectrum for direct cosmic-induced recoils. This shows a slight bias towards the downward direction for extended cosmic data runs. (b) With low statistics, this curve shows a slight agreement with the simulated polar angle distribution, where there is clearly a source of systematic noise at a polar angle of $cos\theta = .05$.

5.6 Detector Background Conclusion

The nature of background for a mobile Time Projection Chamber results primarily from neutrons created in cosmic showers that interact directly with the target gas and spallation neutrons created in nearby material which interact directly in the detector target gas. A conservative number for construction material radioisotope contamination shows an insignificant rate of alpha decays in the mesh material, in regions that are inseparable by image-based cuts. An extended background run shows an increased rate above direct cosmic events, indicating a higher than expected direct cosmic-shower neutrons due to neutron energies above 20MeV and a high ship effect rate, likely due to the amount of concrete and steel above, below, and to the sides of the detector.

Fortunately, the two primary sources of background can be accounted for. The direct-cosmic shower neutrons do not produce a converging signal when calculating probabilistic projections. This signal will reduce the signal-to-noise in probabilistic projections, as will be shown in Chapter 6, but it will not indicate an erroneous source of fast neutrons. At the very most, the slightly downward biased nature of alpha recoils due to cosmic neutrons will indicate a neutron source directly above the detector.

The ship effect neutrons in an industrial building are expected to be nearly isotropic from all of the construction material. If the detector is operated in an outdoor environment, this signal is expected to drop considerably. In either scenario, the detector is unlikely to indicate a neutron source presence. The limitation arrives when a single point of high-Z material is piled in the vicinity of the detector. In this scenario, the pile will eventually register a neutron source and must be accounted for through knowledge of the high-Z material. Future studies will need to examine the difference between bare piles of high-Z material and piles of high-Z material with an enclosed neutron source.

Chapter 6

Stationary AmBe Source Results

In order to characterize the detector, it was operated in a stationary position with a stationary source to test and fine-tune the data analysis algorithms and detector operational settings. The first data collection runs were conducted with a scientific CCD camera in 8X8 binning, resulting in approximately 500keV lower energy threshold. Later, data was collected with the image intensifier and Finger Lakes Instruments camera in order to provide performance estimates with a portable package. Additionally, for both sets of data runs, the field cage was reduced in size to only 15 cm to compensate for diffusion effects in reducing the signal-to-noise in the image.

6.1 Experimental Methods

A set of experimental data runs were conducted with a stationary neutron source in order to test the validity of the back projection. The back projection should be capable of pointing in the direction of the neutron source, given the expected response function from Chapter 7. Additionally, the detector is capable of producing a low resolution energy spectrum which can be used to characterize the source of fast neutrons.

For the stationary data runs, the detector was operated in the same lab setting and same orientation as the extended background run discussed in Chapter 5. An Americium-Beryllium neutron source was placed 71cm from the detector and the detector was operated for an extended period of time.

6.1.1 Neutron Source

The AmBe source is from an 1980s-era Series 3320 Troxler gauge, used to detect soil moisture after lowering the neutron source into a hole in the ground. The source of neutrons are a reaction product initiated by the alpha decay of an Americium-241, with an original decay activity of 10 mCi. With a 432 year half life and after forty years of decay, the $^{2}41$Am has a time-adjusted activity of approximately 9.4 mCi. The $^{2}41$Am is mixed with Beryllium-9, where the alpha decay from the $^{2}41$Am source results in a fast neutron emission through the two reactions given in Equations 6.1 and 6.2 [99].

$$^{9}_{4}\mathrm{Be} + ^{4}_{2}\mathrm{He} \rightarrow ^{12}_{6}\mathrm{C}^{*} + n \tag{6.1}$$

$$^{9}_{4}\mathrm{Be} + ^{4}_{2}\mathrm{He} \rightarrow ^{9}_{4}\mathrm{Be} + ^{4}_{2}\mathrm{He} \rightarrow ^{8}_{4}\mathrm{Be} + n + ^{4}_{2}\mathrm{He} \tag{6.2}$$

This results in an experimentally measured 70 neutrons per million decays of the $^{2}41$Am isotope, or roughly 25,000 neutrons per second from the 40 year old, 10 mCi $^{2}41$Am source in the Troxler gauge [99]. The reaction also produces gamma rays at approximately 75% of the intensity of neutrons [100].

The AmBe neutron source is contained within a steel capsule that is approximately 1.5 inches in diameter and 10 inches in length. The location within the 10 inches is expected to be towards the middle, with shielding contained in the first several inches and last several inches of the steel capsule. There is also a ^{3}He detector contained just forward of the AmBe neutron source, to be used for the originally intended use of measure the moisture content in holes bored into soil. The steel capsule with source is contained in a 6"×6"×10" high-impact plastic housing when not deployed and can be lowered on a thick cable into position when used for detecting soil moisture. The plastic housing also serves as a moderator for safe handling. The source can be removed from the plastic housing up to the length of the thick cable, or approximately 10 feet in order to gain a greater solid angle coverage.

6.1.2 Detector and Laboratory Environment

For the initial runs, the source was placed 71 cm from the TPC on an elevated platform, as depicted in Figure 6-1. The platform positioned the source at the same height as the detector for the initial characterization runs. The laboratory environment is the same as depicted in Figure 5-3. Concrete structural beams were present

Figure 6-1: A depiction of the experimental setup during the stationary AmBe source runs with the Alta Scientific CCD camera. The yellow box is the high impact plastic housing holding the steel capsule with an AmBe source within. The side not seen has a 1.5" hole in the plastic housing where the source capsule can slide out.

throughout the basement lab space, with a cinder block wall immediately adjacent the detector. The lab is located in the basement of a four story industrial building. The background is expected to be similar to the neutron environment measured in Chapter 5, except for minimal changes in solar activity.

As discussed earlier, the TPC is operated with a 50% reduction of field cage length due to diffusion concerns. This reduces the active volume by half, but diffusion would otherwise nullify a greater portion of the active volume. The total active volume of the TPC for these testing campaigns was a cylinder with 6.5 cm radius and 14 cm length. Runs were completed with the Apogee Alta U6 Scientific CCD camera and later with the Photonis Cricket image intensifier with Finger Lakes Instruments (FLD) CCD camera.

The goal of this experimental campaign was to test the probabilistic direction estimates with the given background setting discussed in 5 and the current data analysis algorithms discussed in Chapter 3. After testing with the Alta U6 camera, the imaging system was switched out with the higher portability option with the Cricket Image Intensifier and FLI camera combination. The optimal outcome would be a backpack scale, low power requirement TPC with algorithms capable of pointing towards a neutron source.

6.2 Experimental Results

There are a variety of aspects to confirm when establishing the effectiveness of a prototype detector. Possibly the most critical to building a system for field use, the expected versus actual reaction rate will inform about any systematic errors that result in a lower intrinsic efficiency. Further, the alpha particle recoil energy spectrum should agree with the simulated recoil energy spectrum, which will also improve the understanding of the effective intrinsic efficiency. Finally, these data sets can be used to test the probabilistic back projections discussed in Chapter 7 to compare the ability to point towards a known neutron source.

6.2.1 Reaction Rate and Intrinsic Efficiency

There are multiple areas where a reduction in expected intrinsic efficiency can be experienced in a Time Projection Chamber. First, any downtime in the data acquisition program results in a reduction in intrinsic efficiency, as any interaction that happens during the downtime will be missed. Second, if diffusion is too high, events that occur closer to the cathode will diffuse to the point of dropping below the imaging system threshold. This will result in CSP/PMT pulses, but no associated track in the image. An additional possibility is the time immediately after a spark, where the voltage across the ground-anode amplification meshes recharge. Finally, dead spots in the anode can result in the avalanche being weaker in some areas, again dropping the track signal below the imaging system threshold.

The down time for a spark in the operation of the detector can factor into the detector overall intrinsic efficiency through two mechanisms: the time required to recharge the voltage across the ground-anode mesh capacitor and the time required to flush the CCD. The ballast resistors can be selected to keep the recharge time to one second or less. This is readily achievable in a small TPC, since the capacitance is an order of magnitude smaller than the larger TPCs for previous varieties of this detector. For the latter effect, an issue call Residual Burn-In (RBI) occurs where the CCD pixel becomes saturated with charge and charge becomes trapped outside of the pixel. The charge slowly diffuses back into the pixel and is read out as a typical light signal. This effect causes the image following a spark to be a concern for RBIs leading to false tracks. As such, any image with a spark and the image following a spark are discarded. For the course of this work, the spark rate was held to approximately 1 spark every 30 seconds, resulting in an approximate 7% reduction in intrinsic efficiency.

For the Alta U6 camera, the actual rate versus expected rate should match fairly close, as the actual detector run time can be very accurately measured by the total detector images multiplied by the exposure time. This provides the ability to check the physical intrinsic efficiency while removing the effects of detector dead time, or in other words, check for diffusion problems and anode dead spots. However, the time between exposures when the camera is required to read also factors into the detector operational time and the effective intrinsic efficiency for making statements about future capabilities. When binned 8X8, the data acquisition resulted in a down time of approximately $33 \pm 2\%$, that varied slightly from run to run. When testing with the Cricket Image Intensifier, the downtime appeared to initially be close to 75%, but the algorithm was adjusted to reduce the downtime to approximately 25%.

As can be seen in Figure 6-2, there are some areas of significant reduction in events that is visible when the position is mapped across the amplification plane of the detector. The large red circle depicts the size of the anode mesh which dictates the active volume. The radius is further reduced by the uniformity of the electric field by the distance of ring-to-ring spacing of the field cage [49]. This is not depicted as the majority of that distance is already outside of the imaged volume, which is limited by the CCD chip size and lens combination and denoted by the large, blue square in the figure. The background events from the resistor chain added an additional reduction, by creating a spot in the imaging volume that had to be ignored. Finally, an obvious dead spot on the anode mesh is visible on the positive X-axis side of the amplification plane, denoted by a long dash, orange square. All of these effects add up to an approximate 47% reduction in overall intrinsic efficiency for this detector. All of these effects can be compensated for in future detector prototypes. As discussed in Chapter 5, the background events from the resistor chain serve as an excellent spot-check tool to make sure the detector performance is optimal. The dead spot is believed to be from a very slight flex in the anode and ground aluminum rings when compressed together, letting some areas sag closer while leaving the dead-spot of the mesh slightly further apart. Switching to stainless steel, increasing the thickness, and possibly adding some glass spacer lines every inch should help this non-uniformity.

To compare the expected rates and build the intrinsic efficiency of the TPC across multiple runs, simulations were written in GEANT4 to compare the alpha recoil differential energy spectrum with the background signal from Chapter 5 and the AmBe neutron spectrum from [101]. The simulations did not consider room return, where the likelihood of double scatter while remaining above the lower energy threshold of 1 MeV for the Alta U6 data runs were low enough to be ignored. The Troxler company

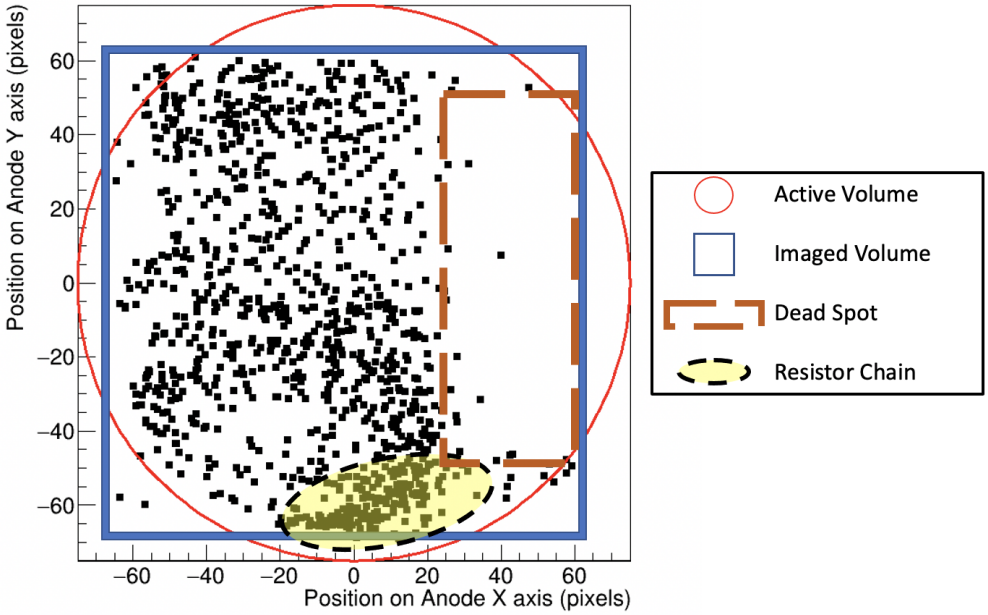

Figure 6-2: Reduction in intrinsic efficiency due to dead spots, resistor chain, and imaging volume. This is a depiction of the position of each event in the amplification plane. The active volume is physically limited by the physical size of the anode and reduced further by the non-uniformity of the electric field [49]. The resistor chain adds enough noise that the area in the immediate vicinity to the resistor chain had to be cut from analysis. Finally, a dead spot is clearly visible on the positive X-axis side of the amplification region. All of these effects add up to a 47% reduction in intrinsic efficiency.

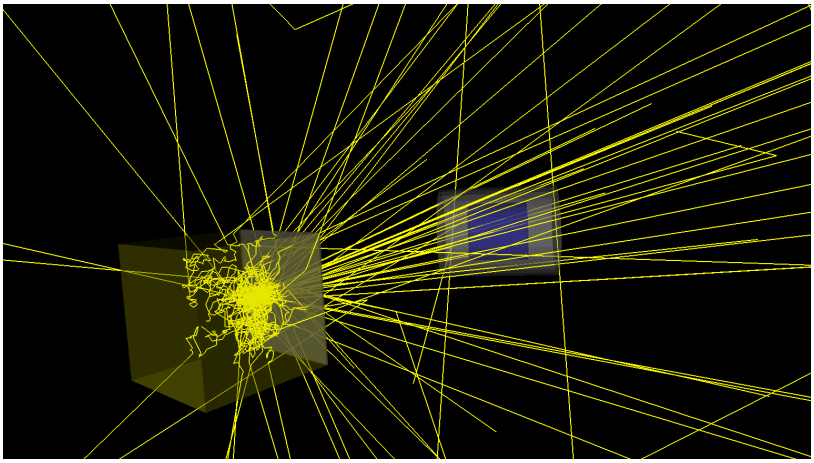

Figure 6-3: A snapshot of 100 simulated events. In this image, the yellow box on the left is the High Density Polyethylene (HDPE) Troxler Gauge housing, with a 0.125" aluminum (grey) and 0.0625" lead (grey) shielding in the forward direction. The Time Projection Chamber is in the background, denoted by an aluminum (grey) right cylinder, the active volume gas (blue), and 15 copper field cage rings. Only neutrons in the forward direction were simulated, as room return is expected to be a small contribution to the total signal.

provided an equivalent model number for a more recent detector, model 4301 and 4302 soil moisture gauges. The Device Registration sheet described a 6" high density polyethylene (HDPE) box around the source, with 0.125" Aluminum and 0.0625" Lead wrapped around the source containing bore hole. From an old image of the gauge in possession, it appears to be an approximate 2" of HDPE in the aluminum probe forward of the source. The box of HDPE and a layer each of aluminum and lead placed in front of the box were simulated in GEANT4 to compare the simulated differential spectrum with the detected spectrum. This can be seen in Figure 6-3.

Finally, after adjusted for the 7% reduction due to sparks and the 47% reduction due to anode dead spots for intrinsic efficiency, the simulated spectrum is compared against the data run spectrum in Figure 6-4. Above 4.5 MeV, the slight increase in counts could be statistical fluctuations, as well as alpha tracks from the soldered resistor chain that survived all cuts in the data analysis. The reasonable agreement between these two spectra show that diffusion is not causing any major issues with losing tracks generated near the cathode to excessive diffusion between the cathode and amplification region.

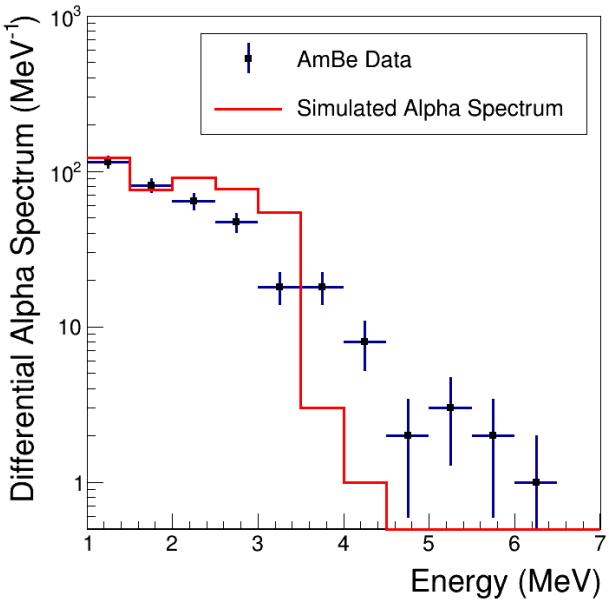

Figure 6-4: A comparison between the detected and simulated alpha recoil energy spectrum. The simulation includes the background signal measured in Chapter 5. As can be seen, there is reasonable agreement between the expected signal and the measured signal after adjustments are made for anode dead spots and shielding effects in the Troxler gauge.

6.2.2 Measured Energy Spectrum

If the position of the source is known or if the position of the source is determined by the back projection algorithms discussed in Chapter 7 and the next section, a low resolution neutron energy spectrum can be calculated by assuming all elastic collisions. With the TPC reporting the alpha recoil energy, position, and recoil direction, the neutron position constrains the problem enough to unfold the source neutron energy spectrum.

Using the equations discussed in Chapter 2 and the cross section to weight each reaction by the likelihood of the reaction, a histogram with neutron energy and weighted counts build the spectrum of neutron energies. After normalizing to compare with measured energy spectra for AmBe neutron sources, there is reasonable agreement between the two curves. Since there were fewer counts than hoped for due to the lower intrinsic efficiency, a Kernel Density Estimate was computed to smooth out the bin-to-bin variance.

The Kernel Density Estimate built into ROOT data analysis is built from the concept of Average Shifted Histograms and serves as a non-parametric estimator for the parent distribution when a smaller number of data points are available [102, 103]. For this process, a local variance approximately one tenth that of the total variance for the entire data set was selected, in order to highlight broad peaks at approximately 3 MeV, 5 MeV, 7.5 MeV, and 10 MeV. The results of the KDE are presented in Figure 6-5.

6.2.3 Direction to Neutron Source

In addition to providing a low-resolution energy spectrum and most applicable to locating a neutron source from a mobile platform, the detector is capable of providing the likely direction to a neutron source. Clearly, if enough statistics are collected for a source within a proximity close enough to overcome the rate of cosmic background events, simply collecting data over extended periods of time will result in an indication of a neutron source. However, in order to transition to a mobile platform, the algorithms from Chapter 7 were written to capitalize on the information gained from each event. These algorithms were tested with simulated data and actual data, with the results presented in Figure 6-6.

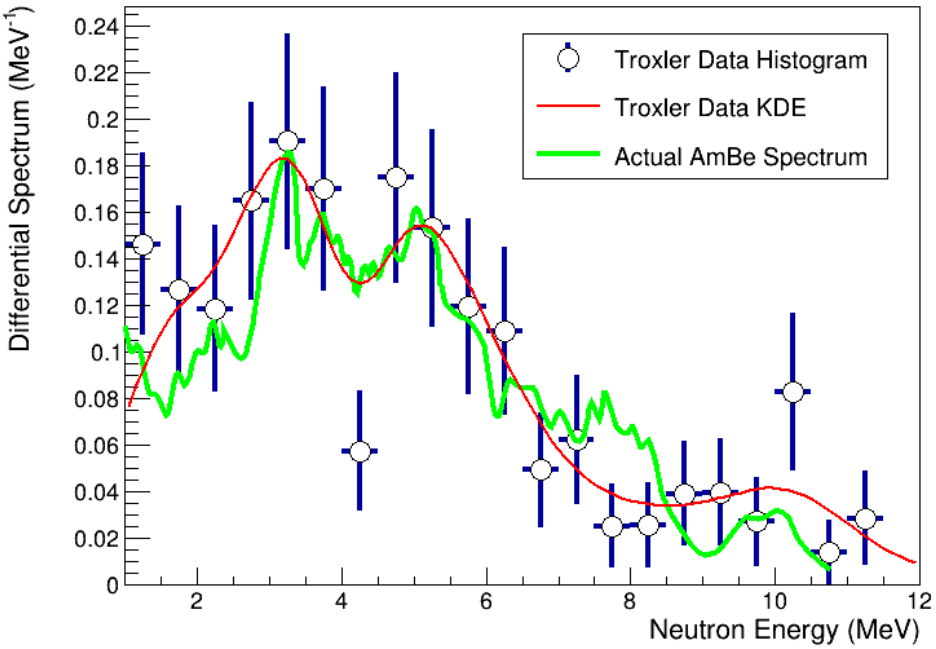

Figure 6-5: The neutron energy spectrum as calculated by unfolding the data from the Troxler source data over a 20-hour data run from 1 meter. This spectrum treats the source direction as a known entity, computes the neutron energy for each alpha recoil, and adjusts the weighting given the neutron-helium elastic scattering cross section. The Kernel Density Estimate, shown in red, shows a strong agreement with the high resolution AmBe neutron energy spectrum measured in [101].

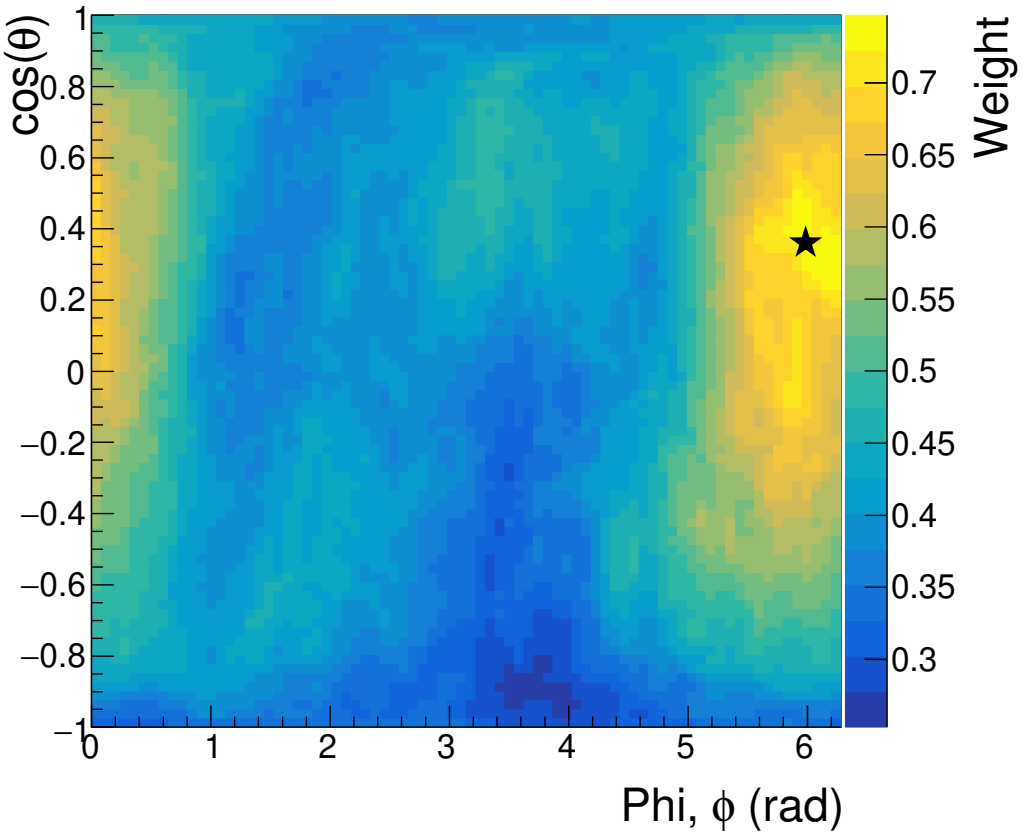

Figure 6-6: The predicted source direction using data from measurements involving the Troxler gauge source and the Alta U6 Scientific CCD camera. A higher weighting is indicative of a higher likelihood of a source present in that direction. The predicted position using full width half maximum above a noise floor of 0.25 for the weighting algorithm returns a direction of 323°in the phi direction, compared to a source direction of 350 °. In the $cos\theta$ direction, the algorithm essentially points to the positive Z-direction, with large uncertainty. However, the distribution is expected to a broad peak centered around the direction, as discussed in the next section.

6.3 Discussion

As discussed in Chapter 7, using this weighting algorithm provides an event-by-event directionality for a portable TPC, opening the door for dynamic back projection for a mobile version of this detector. While this TPC has a reduction in intrinsic efficiency, the active volume shows reasonable agreement between the simulated and detected alpha differential energy spectrum. The dead spot in the anode can be solved by an improved anode-ground mesh ring construction. This detector shows that 15 cm is within the limits for a drifting track to remain above the noise floor of a scientific CCD. Most importantly, the probabilistic back projection is an effective method to generate a direction on every recoil track. With cosmic background producing a nearly uniform background across the solid angle and ship-effect neutrons being a very low rate, this method shows a promising path forward for mobile TPC operations.

The steady background of neutrons adds an interesting background to deal with when determining the direction. Using Geant4 simulations with a neutron background comparable to that measured in Chapter 5 resulted in very similar results to the experimentally measured results in this chapter. Additionally, the resolution of each measured quantity impacts the probabilistic projection in different aspects. For example, adding 25% Gaussian error for the energy in the simulation, as reported in Chapter 3, has a minimal impact on the back projection, but 15% uncertainty in the measured Z-range adds considerable broadening to the distribution in the $\cos(\theta)$ axis. The effects from each adjustment in the simulation results can be seen in Table 6.1.

The energy showed a 25% uncertainty as discussed in Chapter 3. This had a minimal effect on the probabilistic projection when isolated in the simulation data. The X-Y range uncertainty can primarily be attributed to the electron diffusion across

Measured Quantity	Relative Uncertainty	Effect on Results
Energy	25%	No noticeable effect
X-Y Range	25%	Broadened in $cos\theta$
Z Range	35%	Broadened and/or Skewed in $cos\theta$
Azimuthal Angle, ϕ	5-10 °	Broadened in ϕ
X/Y position	1 mm	Broadened in ϕ
Z position	4 cm	Broadened in $cos\theta$
Time	4 μs	No effect for stationary

Table 6.1: The uncertainty from each measured quantity in the primary AmBe source data run.

the drift region, making it difficult to determine the exact starting position and ending position of the recoil. Along the same arguments, the X/Y position error is of the same origins. As such, an uncertainty on the order of the average diffusion is assigned. This has a tendency to broaden the azimuthal angular resolution.

The error in Z-range is a function of the uniformity of the drift field, the time characteristics of the PMT, and the diffusion across the drift field. At high diffusion, the longitudinal diffusion will cause the track to extend, resulting in a longer Z range measurement than the actual recoil track. This broadens the weighting distribution in $cos\theta$, and is likely the primary contributor to the additional uncertainty in this data run. Along the same argument, the time is reported by the PMT and will carry a similar error in timing due to the diffusion of the track. However, the timing only plays a role when the detector is mobile and the uncertainty in time will be several orders of magnitude smaller than the characteristic time of a human-portable Time Projection Chamber.

6.4 Minimum Expected Capabilities

With an expectation that future detectors will operate at 10 atm internal pressure with minimal added thickness to the vacuum/pressure chamber, the rate of interaction from the source and the cosmic-generated background neutron signal will increase at the same rate. As such, the minimum detection capabilities for this chamber should match the capabilities of a larger, higher pressure chamber. The primary difference will be the time required to achieve this directionality. With a chamber that is approximately double in size with no dead spots in the anode, an improvement in speed of four times is expected. Further, when switching from 1000 Torr to 7600 Torr, the an improvement of 7.6 in time is expected. Finally, using an improved energy threshold with a better imaging system will allow an energy cut as low as 100 keV. This will also double the interaction rate. As such, the same directionality should occur approximately 60 times faster than the current setup.

With the current setup, the direction to the source took more than 100 interactions to build a hot spot in the weighting algorithm, compared to 15 interactions in background free simulations. If the cosmic-generated neutron signal can be moderated by an order of magnitude with an overhead high density polyethylene shielding, the rate of cosmic-generated neutrons is expected to be less than 1 neutron per second when outdoors, and on the order of 10 neutrons per second with overhead cover consisting of an industrial building. With a source strength of 100,000 fission neutrons

per second, or approximately 1kg of Weapons Grade Plutonium [29], at a distance of 25 meters, a 4L detector operated at 10 atm will be capable of determining the source direction in just under 2 hours. However, by introducing the mobility, the point spread function should scale as inverse distance rather than inverse distances squared. The improvement is discussed in Chapter 7.

6.5 Conclusion

Barring the dead spot in the anode, the TPC is operating as expected and the results from stationary runs show a promising path forward for a portable TPC. Of the measured quantities and how they impact the reported position of the neutron source, the Z-range and the Z-position created the largest uncertainty, resulting in a very broad weighting distribution in $cos\theta$. As a result, future studies should focus on improving the Z-position. With an improved Z-position of the initial recoil track, adjustments can be made to the X/Y range and Z range to account for diffusion. Additionally, with the addition of cosmic-generated background neutrons, the direction finding algorithms require approximately 100 tracks before providing a crude direction. This is compared to background simulations reporting the position in approximately 15 tracks. With the cosmic-induced background affecting the weighting algorithm to this extent, future detector iterations should provide an HDPE moderator directly above the TPC, where the vertical direction has a thicker amount of moderator that gradually tapers in the polar angle. This could potentially reduce the cosmic-induced background, allowing faster terrestrial neutron source searches.

Chapter 7

Dynamic Probabilistic Back Projection

7.1 Introduction

If a detector is sensitive in all directions covering a 4π solid angle at any given time, a mobile form of this directional detector can significantly improve the time required to locate a radiation source. Previous work with gamma ray detectors have shown that a directional, moving detector has a source location point spread function that scales as the inverse distance, and not the inverse distance squared [33]. Handheld and directional gamma detectors have been used in locating radiation hot spots in the aftermath of the Fukushima accidents [104]. This backpack-scale TPC offers exactly this opportunity but with fast neutrons, using mobility to offset the reduced size and reduced intrinsic efficiency. With the penetrating nature of fast neutrons, a portable TPC offers a first-of-its-kind technology. Building on decades of computational tomography and directional gamma ray detector systems development, a probabilistic model of source location can be built. A portable TPC can provide an improved capability for radiation field mapping to first responders, military search operations, and IAEA safeguards inspectors.

7.2 Inverted Geometry Tomography

Dynamic reconstruction draws heavily from the developments of the varied fields of tomography. In the simplest case of tomography, the source is located inside an array of position sensitive detectors, where line integrals are performed, building a

probabilistic model of the source location through density maps. This is the case in Computed Tomography (CT), Positron Emission Tomography (PET), and acoustic ocean tomography [105]. These can be considered as forms of straight line tomography. Diffraction tomography, on the other hand, uses the diffraction patterns to build the probabilistic location of the source. Diffraction tomography is more commonly computed with sound waves propagating through a medium, as in photoacoustic computed tomography [106]. In addition to the difference between straight line and diffraction tomography, some systems have been designed in an inverted geometry, where the source is not surrounded by position-sensitive detectors, but instead a direction sensitive detector is used to locate a nearby source of radiation.

In a straight-line tomography setup, rays are drawn between two detectors, as in PET scans, or between source and detector, as in CT scans. The density of line integrals that converge on a single point results in points of increased positron emission activity or higher attenuation of x-rays, respectively. Each interaction in a detector results in a given set of rays that can trace back through the point of interest. In an inverted geometry setup, only half of the setup described is available, where the other end of the system is mimicked by a blocking mask. Many of the directional gamma ray detectors for nuclear security have been constructed in this manner, with straight line tomography and inverted geometry. This is made possible by relatively small amounts of material required to effectively block gamma rays from position sensitive gamma ray detectors, forming a version of an coded aperture [5, 107]. The rays trace through non-blocked areas of the mask. This can be depicted in two dimensions by considering a one-dimensional array of blocking masks and two separate detectors, as depicted in Figure 7-1.

Neutrons in the MeV energy range can be considered to travel in straight lines over 10s to 100s of meters to a high degree of confidence, as well. The flux-averaged cross section for fission source neutrons in air above 100 keV in air is 0.88 barns, resulting in a mean free path, λ of $\approx$ 450 meters. Approximately 97.8% of neutrons emitted above 100 keV will survive a 10 meter journey unaltered in energy or direction. However, this same penetrating nature of fast neutrons also prevents the use of small, simple blocking masks for use in a comparable handheld coded aperture for fast neutrons. Directional neutron detectors designed with a blocking mask are not feasible in one person portable packages, but are capable with larger systems such as the ACTINIDES detector [8]. Additional designs for directional neutron detectors to address the inverted geometry tomography have included multiple scattering and time encoded apertures with successful results [35, 108]. However, the multiple scattering

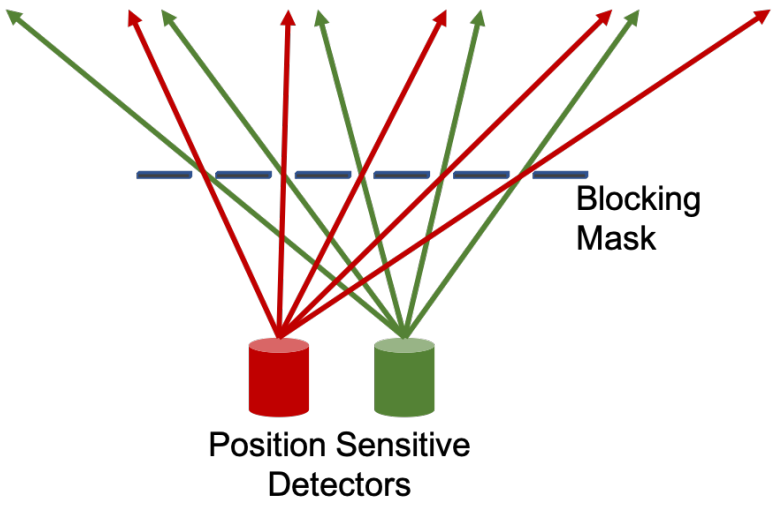

Figure 7-1: An example of a blocking mask used in typical gamma ray coded apertures for inverted geometry straight line tomography, reproduced from [33]. An array of position-sensitive detectors (here one red and one green) are used to project back through the blocking mask the possible source locations based on a blocking mask placed between the detectors and the possible source locations. These style of detectors typically only provide direction sensitivity over a portion of the solid angle, but they are capable of being built into small packages for gamma ray detection.

combined with a gaseous detector results in an extremely low intrinsic efficiency. Further, the time encoded detector is not one-person portable, but can be considered truck portable at best. With a portable time projection chamber and an assumption about the neutron energy spectrum gives the possibility of a back projection based purely on the probability of interaction.

7.3 Probabilistic Back Projection

The directional nature of a time projection chamber is not as straight forward as tracing rays back through a blocking mask. As discussed in Chapter 3, the detector provides the alpha recoil energy, the recoil direction, the position, and the time of interaction. With an assumed source neutron energy spectrum, the details of the neutron source direction can be inferred through weighting functions described in this section.

In the simplest example, take a mono-energetic neutron source of approximately 500 keV. Referring to the ^{4}He elastic scattering angular differential cross section presented in Figure B-1, the interaction of highest likelihood is a back-scattered neutron,

resulting in maximum energy transferred and the alpha recoil direction being in the exact opposite direction from the neutron source. Knowing the direction and energy of the alpha recoils, any alpha with energy of approximately 320 keV points in the opposite direction of the neutron source. Similarly, a cone drawn from alphas with less than 320 keV with an opening angle dependent on the alpha energy, will pass through the neutron source. While the fission neutron spectrum is not quite as simple as a 500 keV mono-energetic neutron source, the fundamentals remain the same.

The nature of data streaming from a Time Projection Chamber enables this probabilistic projection to restrict the possible neutron source directions based on the alpha recoil energy and direction. In a very rudimentary sense, an alpha recoil can immediately restrict half of the 4π solid angle by assuming only elastic collisions. However, this can be bounded even closer to the true information by considering the elastic scattering angular differential cross sections and the expected neutron source energy spectrum, as discussed in Chapter 2. The overwhelming majority of nuclear recoils will occur as a result of an approximately 1 MeV neutron scattering from a ^{4}He nucleus. Further, a 1 MeV recoil favors equally a forward and backward scatter in the center-of-mass coordinate system. The forward scattered neutron will likely result in an alpha that falls below the energy threshold of approximately 100 keV in a high pressure TPC, but the backward scattered neutron results in an approximate 600 keV alpha recoil at approximately 90° from the original neutron direction. Therefore, alpha recoils with energies at approximately 600-700 keV are the most likely recoil energies above 500 keV. Below 500 keV, there will be a large distribution of higher energy neutrons that scatter forward, resulting in lower energy alphas.

This can be extended further by building a two-dimensional probability distribution function in regards to alpha recoil energy and alpha recoil direction. This PDF is built using background-free Geant4 simulations. The simulation assumes a Watts fission spectrum for spontaneous fission source searches or the measured AmBe source neutron energy spectrum for AmBe calibration runs [101]. This two-dimensional probability distribution function is depicted in Figure 7-2, where the peak at alpha energy of 600 keV and $\cos(\theta)$ of 1 is visible, and a larger, broader peak at lower alpha energies. This is analytically equivalent to a two dimensional Probability Distribution Function (PDF), where the neutron energy spectrum, neutron-alpha interaction probability, and neutron-alpha angular differential scattering cross section are coupled to produce the distribution as a function of alpha energy and alpha recoil angle. The one-to-one correspondence between alpha energy and alpha recoil angle to incident neutron energy and neutron recoil angle allows converting measured data into this

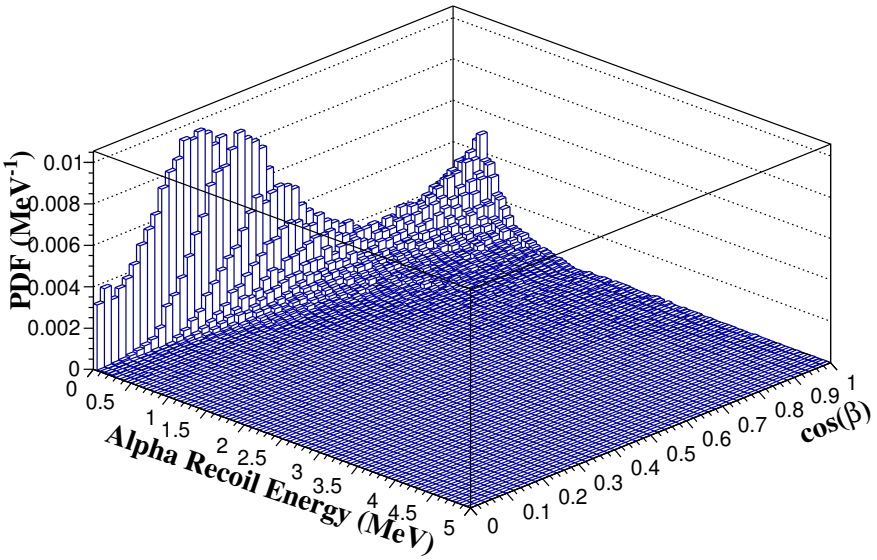

Figure 7-2: The double differential distribution function of alpha recoil events when a flux of fission spectrum neutrons is incident on the detector. Theta, (θ), represents the recoil angle from the incident neutron direction. This distribution was simulated by Geant4 and is used to condition the expected location of a neutron source, given the alpha energy and alpha recoil direction in the lab frame.

PDF. A simulation was used to build this distribution, as the simulation will include any additional features beyond elastic scattering.

In a Bayesian style of probability inference, this two dimensional PDF is used to condition the likely alpha recoil angle given the measured alpha-recoil energy. After each event, the recorded alpha energy is used to condition the 2D PDF, resulting in a one-dimensional Probability Distribution function. An example is provided in Figure 7-3(b). For the example in Figure 7-3 and given the recoil direction in the lab coordinate system, the probable neutron source locations are located at all back-projection angles that form an approximately 60˚angle with the alpha recoil direction. This appears as an cone projected in the opposite direction of the alpha recoil direction.

This is analytically equivalent to Equation 7.1, where each direction through the 4π solid angle is considered, resulting in a weighting function W that is dependent on the direction to the alpha recoil position (the origin in Figure 7-3), alpha energy E_α, and alpha recoil direction θ_α, $\phi\alpha$. It is a function of the conditional probability given the laboratory alpha recoil angle and alpha energy at the implied neutron source direction, denoted by ϕ_n and θn. The algorithms check every direction in 4π, compute the implied alpha recoil angle for a neutron from this direction, and give the direction

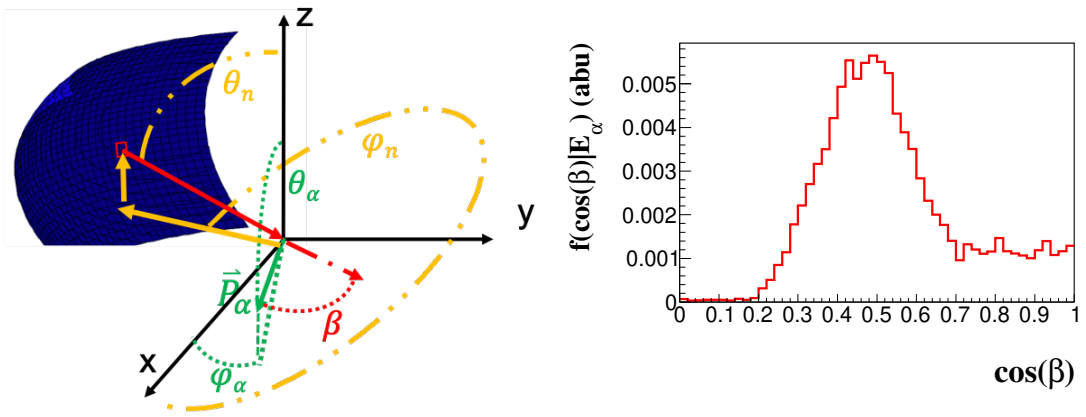

(a) (b)

Figure 7-3: (a) A cartoon diagram depicting the algorithm concept, where every neutron direction is used to compute the implied alpha recoil angle. In this diagram, the green β_α and ϕ_α imply a directly measurable quantity indicating the alpha recoil direction in the laboratory coordinate system and the red θ is the alpha recoil angle at the implied neutron source direction. The weighting is computed from the conditional PDF in (b). All directions to a possible neutron source, θ_n and β_n, in 4π are considered, resulting in a projected cone for this particular alpha energy. This probabilistic neutron source location serves as an analogue to a blocking mask, where a cone is projected in the opposite direction of the alpha recoil direction. (b) An example of the conditioned probability distribution function given an alpha recoil of 300 keV. This PDF is pulled from the two dimensional PDF in Figure 7-2, which is conditioned on the known alpha recoil energy.

a weight with the probability from the bin corresponding to the respective alpha recoil energy and angle.

$$W(\phi_\alpha, \theta_\alpha, E_\alpha, \phi_n, \theta_n) = f(cos\beta|E_\alpha)\Big|_{(\phi_\alpha,\theta_\alpha,\phi_n,\theta_n)} \tag{7.1}$$

7.4 Response Function

This probabilistic back projection will not produce an obvious response function. As a result, a background free simulation with 125,000 alpha recoils was conducted in Geant4 in order to understand the back projection response function, which can then be used as the expected distribution when determining the uncertainty in a measurement of the direction to a source in a stationary setting. This response function is depicted in Figure 7-4.

As discussed in Chapter 6, this response function is affected by the uncertainties in all of the different measurements being made in the detector. However, Chapter 6 shows that even with a low resolution measurement on the variety of data streaming from a TPC, the data still provides directional sensitivity across the 4π solid angle. As such, even at low energy resolution and high position and direction uncertainties, the detector offers a solution to locating a source of fast neutrons when operated in a dynamic sense. The remainder of this chapter will be dedicated to testing this dynamic probabilistic source location concept through simulations with realistic detector measurement uncertainties.

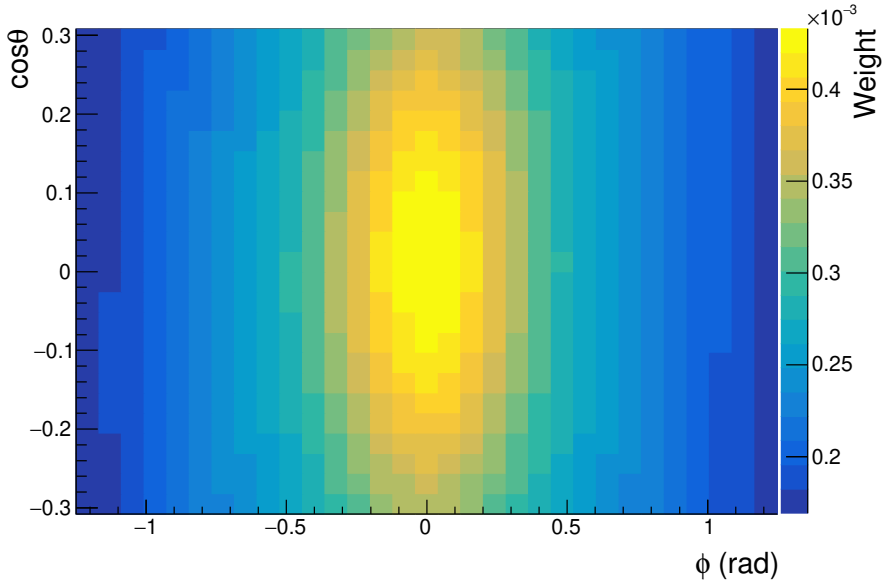

Figure 7-4: The response function for detecting the direction from a stationary detector.

7.5 Experimental Setup

Due to a lack of small, portable neutron source, the detector was tested against simulated data for stationary source results, with a discussion of the results provided in Chapter 6. The characteristics of the detector were then used to build a simulation in Geant4 with a moving neutron source and a stationary detector. After the simulation and during the back-end data analysis, the reference frame was converted to a stationary source and a moving detector. Further, the data from the simulations were adjusted with Gaussian error from the results of Chapters 3 and 6.

The detector was simulated as the full backpack detector operated at 10 atm. The dimensions of the detector simulated was 38 cm long by 15 cm in diameter, slightly larger than a standard firefighter's air supply backpack. The neutron source simulated was a kilogram of Weapons Grade Plutonium (WGPu) with a Watt's fission spectrum activity of 100,000 neutrons. The original position of the neutron source is approximately 4 meters from the detector, with an impact parameter of one meter. The source moves at a speed of 0.25 meters per second, where an active search for radioactive sources is expected to be slow and deliberate.

At the given source position, the percentage of solid angle that encloses the detector is computed and used to determine the distance the detector will travel before the next neutron is emitted into that cone. The cone of solid angle that contains the

detector is slowly varying as the source is either far away from the detector or close but moving in very small increments between each neutron emitted into the detector containing solid angle. A time lapse across an extended period of time is depicted in Figure 7-5.

In addition to the moving neutron source, the same cosmic-generated background that was measured in Chapter 5 and simulated in Chapter 6 was used in this simulation to provide a relevant expectation as to the effects of the detector's background. These background neutrons were generated with the same angular distribution in the zenith angle and the same energy spectrum as discussed in Chapter 5. The simulation adjusted the rate of cosmic neutrons based on the distance traveled by the neutron source between emitted fission neutrons.

Using this simulated setup, the simulation was written to use batch statistics to determine the error of the weighting function. 1,000 passes were made with this setup with no source present, with a 1kg WGPu source at 1m closest approach, and with 1kg WGPu at 2m closest approach. The uncertainties from Chapter 6 for each measured quantity was added in the back-end data analysis.

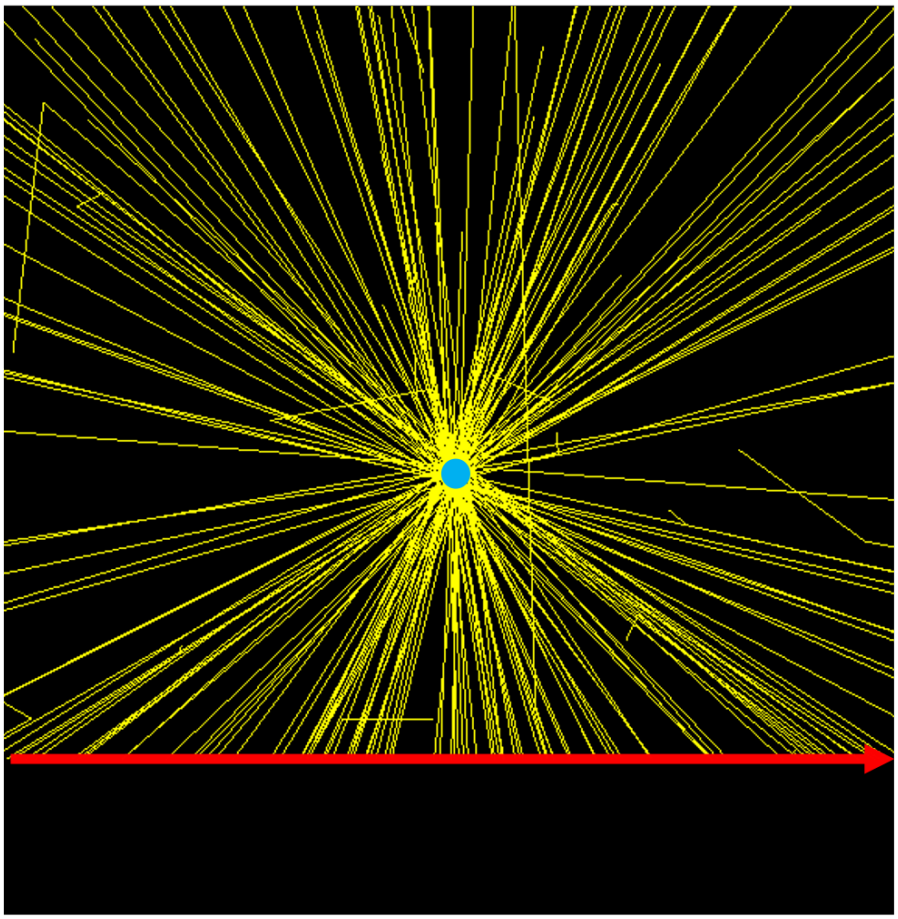

Figure 7-5: A visual rendering of the moving source and neutrons emitted in a portion of the solid angle that includes the detector. The portion of the solid angle enclosing the detector is recalculated at each step and used to adjust the next likely position of the moving source that a neutron is emitted in the portion of solid angle containing the detector. The source is propagated to the new position and the primary particle is generated in a randomly generated isotropic direction within that portion of solid angle, depicted here as yellow lines emanating from the source moving along the red arrow. In this rendering generated by OpenGL in Geant4, the red arrow has been added to help visualize the direction of motion of the neutron source and the blue circle has been added to indicate the active volume of the detector.

7.6 Experimental Results

In the data analysis, the same probabilistic projection method was used with appropriately added error on each measured quantity, but instead of producing a directional weighting function, a three dimensional grid in the physical space around the detector was weighted for possible neutron source locations. At each binned location of physical space, the direction between implied neutron source and detector resulted in a calculated alpha recoil angle, which produced the probabilistic weighting. This produces a weighting map as depicted in Figure 7-6.

After each simulated pass, the two-dimensional weighting function is analyzed for the maximum bins in the X- and Y- axes, and then a weighted mean in bin space is computed. This is converted into physical dimensions and a histogram is populated with the predicted source location. With a five meter running window, the maximum bin is plotted in a histogram for three different simulated scenarios in batches of 1,000 each: background alone as measured in Chapter 5, 1kg WGPu at 1m closest approach with the same background, and 2kg WGPu at 2m closest approach with the same background. This is shown in Figure 7-7.

Clearly, the portable TPC with the weighting function is capable of distinguishing between background signal and the presence of a nearby neutron source. However, there is overlap in the 2m-closest approach curve and the background curve, which opens the door for false negative and false positive reports. A false negative occurs when a source is present and the weighting function reports no source. A false positive occurs when no source is present and the weighting function reports the presence of a source. In consideration of mapping radiation sources, an assumption is made to minimize all false negatives, with a false positive having minimal impact. This logic does not necessarily hold true for portal operations where a false positive can significantly alter the operation of people and cargo coming through the port of entry as operations stop until the source is confirmed and cleared. However, for first responders, IAEA inspectors, and military searches, a false positive results in additional testing, allowing a determination of no source at a later time. As such, a false negative should be minimized to the maximum extent, and false positives minimized within reason.

After plotting the weighting function across a five meter by five meter window, the maximum of the weighting function is recorded for 1,000 passes. For the closest approach of one meter, the distribution of the weighting function maximums across these 1,000 passes is fit with a Gaussian of mean 0.07 and a sigma of 0.01. The

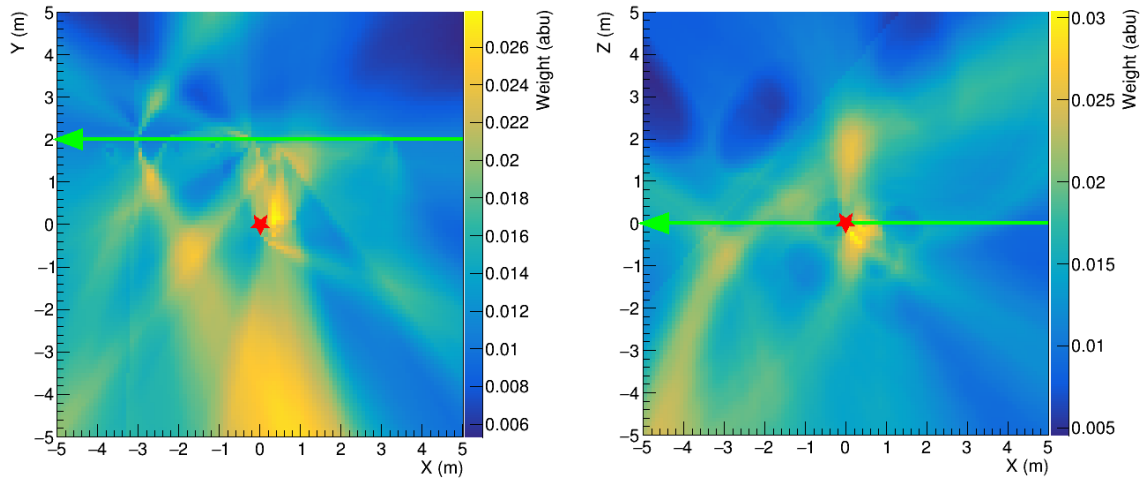

Figure 7-6: The three dimensional weighting from a single pass of a portable TPC at a closest approach of two meters from 1kg of WGPu. The green arrow depicts the location and direction of travel of the detector and the red star depicts the location of the source. The weighting is computed by the same alogirthms used in directional testing with a stationary AmBe source.

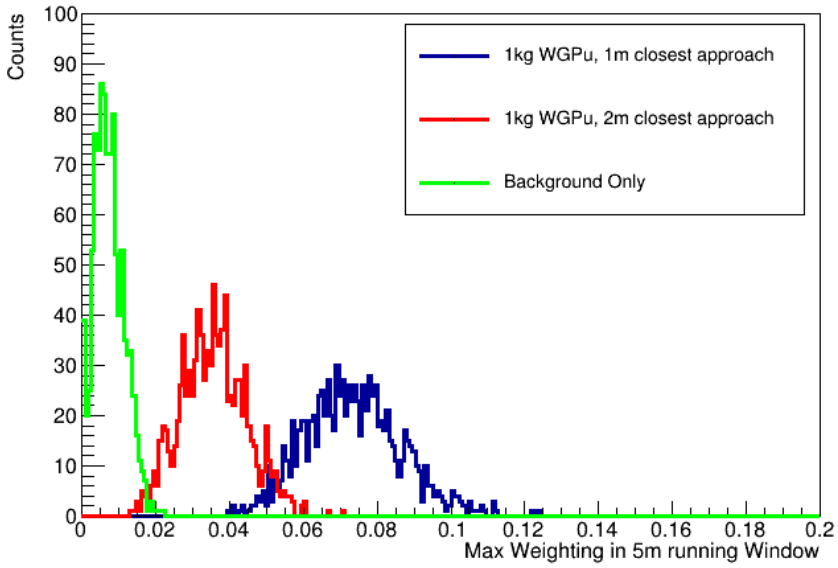

Figure 7-7: A comparison of the signal-to-noise in the weighting function compared between simulated background signals and simulated background with 1 kg WGPu. The green curve represents 1,000 separate passes through a 10m by 10m location with background alone. The green curve represents the same, but with a 1kg WGPu source located at a closest approach of 1m. The blue shows the same, but with a closest approach of 2m.

weighting algorithm for simulated background fits, with no source present, is fit in the same manner with a mean of 0.0069 and a sigma of 0.004 for the distribution of maximum weighting values in a rolling five meter by five meter window. Using a trigger based purely on the maximum weight in a rolling five meter window and setting the trigger threshold to a weighting value of six sigma, the detector will falsely report the presence of a source 24% of the time on a single pass with background only, while missing a source approximately 1 in 10 billion times. Using the same threshold with the 2m closest approach, approximately 2 in 1,000 passes will miss the presence of a source on a single pass. Using multiple detectors evenly spaced to account for this rate of false negatives will reduce this number to 4 in a million passes. If this number of false negatives is not acceptable given the operational environment, the user needs to consider passing every location of the facility closer than 2 m or consider moving more slowly through the facility.

In addition to the presence of a source, as can be seen in the weighting map of Figure 7-6, a physical location is also reported. After 1,000 passes in Geant4 simulations, the maximum bin is recorded and then used to build a local weighted maximum to report the position of the source. The distribution of these source predictions is presented in Figure 7-8.

Figure 7-8 indicates a reported position accuracy of 50 cm in the direction of travel (X axis) and 60 cm in the direction orthogonal to travel (Y axis). Again, these results are focused on a single plane of search, but the algorithm is a three dimensional algorithm and can readily be extended to account for height above and/or below ground.

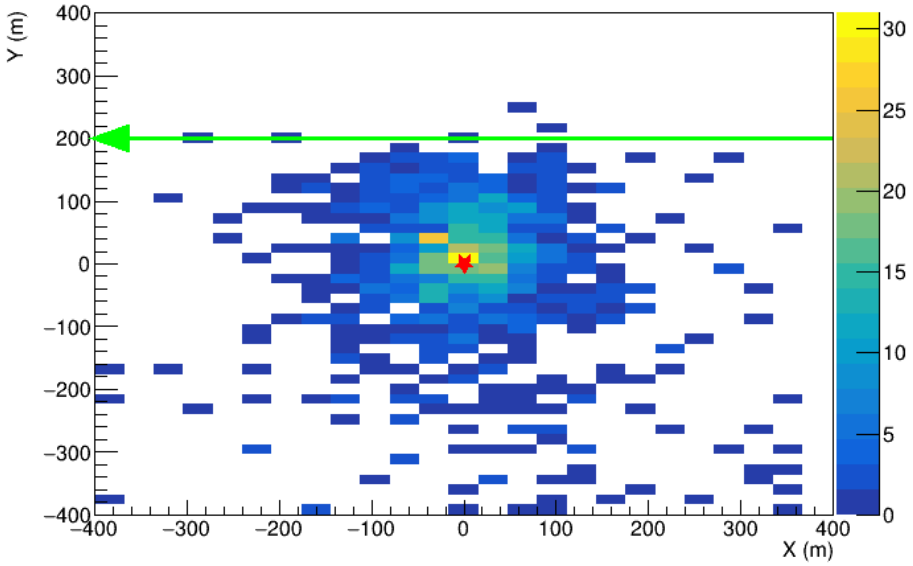

Figure 7-8: The distribution of the predicted source location after 1,000 single passes at a minimum approach of 2m and a walking pace of 1 mph. The source is located at the red star in the plot, with an activity of 10^5 n/s. Using a Gaussian fit on the projection of the middle three bins, the error in the direction of travel is 50 cm and on the orthogonal direction is 60 cm. While this course of work focuses on detection in a two-dimensional plane, this algorithm is immediately extendable to three dimensions, where position can include a height-above-ground position as well.

7.7 Discussion of Results

The use of a directional detector coupled with the relative motion between the source and the detector helps offset the cosmic-generated fast neutron background. The 1kg WGPu source is capable of being detected and located at approximately two meter closest approach on a single pass with a false negative less than 2 out of 1,000 passes. Multiple detectors carried by different personnel will increase the distance of detection or further decrease the rate of false negatives. More importantly, each of these detected sources is tied to a physical location in three dimensional space. As such, moving closer to the predicted source location can quickly confirm or deny a positive source reporting.

Inevitably, the background will be the driving factor for determining the distance at which a source can be detected. Significantly increasing the pressure will increase both the background as well as the source signal, equally. Increasing the size of the detector, while impeding the mobility of the detector, will increase the interaction rate from the source as well as from the cosmic background.

As such, future work should include creating shielding mechanisms that can moderate the overhead fast neutron signal to reduce the cosmic-generated background. This should first include an extended and detailed measurement of the cosmic-generated background. The double differential angular energy spectrum should be measured to determine the relationship between angular flux and neutron energy spectrum. This is discussed in further detail in Chapter 8.

The combination of a source reported by the maximum value of the weighting function and the reported position make this technology an exciting capability for radiation field mapping, neutron source localization, and source characterization. With the reported positions and with time allowing, the threshold can be aggressively reduced on the first pass, intentionally allowing an increased false positive rate while simultaneously increasing the rate of detection. The second pass can deliberately move within a meter of each reported source position to confirm or deny the presence of a source.

Finally, as discussed in Chapter 6, all of the data can be locally stored throughout the run. Whenever a source is reported, the position can be used to unfold the energy spectrum using the physical location of each alpha recoil, the recoil direction, the recoil energy, and the reported position of the neutron source. Using the energy spectrum, the source can be characterized through isotope analysis and source activity. This is demonstrated for a stationary source and detector in Chapter 6.

7.8 Conclusion

Using the expected uncertainties from the measurements made in Chapter 6 and the background signal measured in Chapter 5, the simulations discussed in this chapter show that a mobile version of this detector, when operated at 10 atm and 6.7L of active volume, is capable of detecting and locating a 1kg source of unshielded WGPu. This is a first-of-its kind technology, as the only directional neutron detectors are field-deployable at best, but not one person portable. This detector compliments directional, one-person portable gamma detectors that are currently being deployed for radiation field mapping operations.

Chapter 8

Conclusion

The concept of a portable Time Projection Chamber opens the door for a detector with 4π directional sensitivity and a low gamma sensitivity. The research discussed herein demonstrates the capabilities and necessary future work to increase the readiness of this technology. The background is primarily composed of cosmic-generated neutrons either directly from cosmic showers or indirectly from spallation neutrons, known as "Ship Effect" neutrons. The effect of this background can be minimized by capitalizing on the omnidirectional nature of cosmic-generated neutrons. In a stationary setting, this detector demonstrated a novel new directional capability that has a foundation in Bayesian probability and improves the speed at which the source direction is confirmed. Using this new directional approach and the uncertainties measured and inferred from Chapter 6, simulations show that this detector, when operated at 10 atm, is capable of locating a fast neutron source with an activity of 10^5 n/s to a point within 60 cm on a single pass at a minimum approach of 2m. Using the same thresholds, the false positive rate is approximately 2 false positives per 1,000 passes with a false negative threshold of approximately 24%, where false negatives are intentionally allowed to be higher as a second pass can be made closer to any reported hot spots.

While this is exciting new technology, there are a host of areas for future work to continue and improve this technology for future operational use. The research discussed here kept a maximum pressure of 1,000 Torr to prevent damage to the viewports. This pressure should be increased to the maximum pressure given structural limits for a portable package and given the imaging capability limits for track length in higher pressure systems. Additionally, increasing the signal-to-noise in the imaging setup should improve the reconstructed range, reported z-position within the detector, and reconstructed angle within the amplification plane, ϕ.

8.1 Operating at Higher Pressures

In order to increase the interaction rate and decrease the amount of time required to pinpoint a location of fast neutrons, the operating pressure should be increased. The upper-end of the pressure is limited by the pitch of the mesh, the resolution of the imaging system, and the structural capability of a backpack-scale chamber. Comparing to a modern firefighter backpack, a 300 bar pressure tank weighs only 3.9 kg [109]. As such, a final product is expected to have minimal weight when constructed in a composite over-wrapped pressure vessel and the limiting factor becomes the track length capable of being imaged.

When the lowest energy alpha recoil tracks are on the scale of the pitch of the amplification mesh, directionality will be lost. A range of 5 wire squares across the mesh serves as a reasonable lower bound for track length. At this length, a track that is pitched at 45° in polar angle and 45° to the primary axes of the mesh, the length of track in the amplification plane will reach 3 mesh squares. It appears from simulations that the electron drifts around the ground mesh and avalanches near the center of the open square in the mesh, as opposed to being masked behind mesh wire. Therefore, increasing to higher pitch mesh should not cause any major reduction in total light collected at the imaging system. With a readily available wire mesh of 400 wires per inch, the pitch is 63.5 μm, resulting in the shortest track length with five mesh squares being 320 μm. At 10 atm, SRIM simulations show a track length of (340 ± 40) μm for 50 keV. However, at this track length, the imaging system will need to be reconsidered, as a 15cm diameter anode would need an imaging system with resolution of 5.8 megapixels. This is readily achievable in modern CMOS cameras, but in switching to low power equipment, the image intensifier will be the limiting factor. The current Cricket image intensifier is capable of 55 line pairs per millimeter, with a diameter of 18 mm. This results in 990 line pairs across the diameter of the anode, or 150 μm minimum resolvable thickness. In the near term, the current Cricket image intensifier can be used to test a high pressure system, with energy cuts occurring at 200 keV and track lengths of 800 μm.

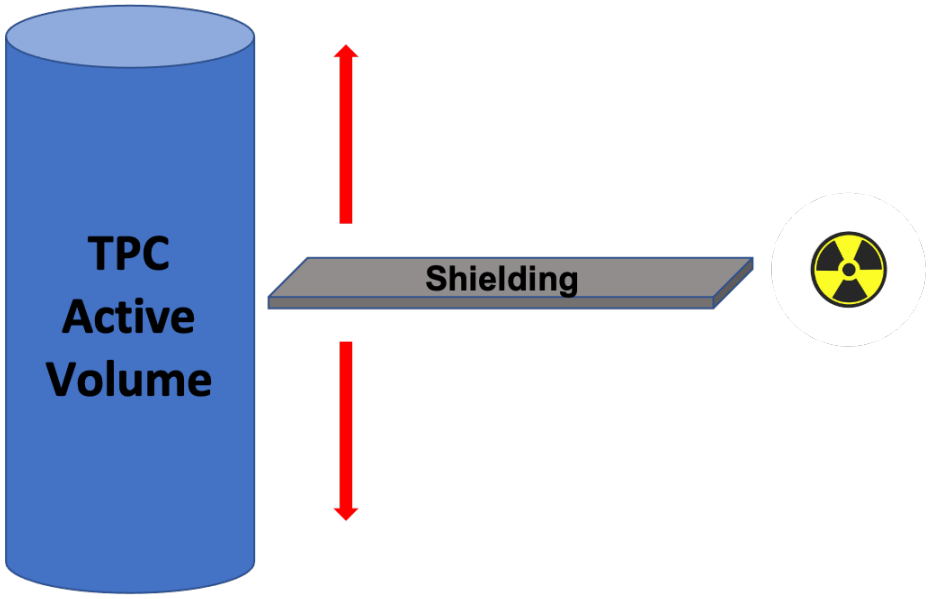

Figure 8-1: A future test setup to confirm the uncertainty in the Z-position reconstruction. With a long, thin shield depicted by a thin grey rectangular shape and a higher activity source denoted by the radioactive symbol, the reaction rate should be high enough above the cosmic-generated background neutrons to produce a void region when plotting the position of all alpha recoils in the TPC. The position of the shield can be varied along the active volume of the TPC to determine the uncertainty in Z-position measurement, depending on the position in the active volume.

8.2 Image Signal to Noise and Z-Position Reconstruction

An improved signal-to-noise in the image of the track should also translate to an improved Z-position measurement. Previous studies have shown that increasing pressure increases the percentage of CF_4 light that scintillates in the visible range. This should immediately help the image signal to noise. The Z-position measurement should also improve with an improved image signal to noise. With an improved Z-position measurement, testing should be conducted to measure the resolution in Z-position. This can be done by placing a long, thin moderator between a higher activity neutron source and the TPC, as depicted in Figure 8-1. With a higher activity source, the reaction rate should be high enough to create a region within the detector that is void of alpha recoils. Specifically, a projection of all recoils onto the Z-axis will show the uncertainty in the Z-position measurement by the depth and width of the void region.

8.3 Adding Sensitivity to Thermal Neutrons

In order to provide the optimal capability for the system, adding sensitivity to thermal neutrons would improve the overall capability of this technology. Some options pitched in the past include adding ^{3}He in small concentrations to add sensitivity to thermal neutrons [37]. While this is an attractive approach, the ^{3}He response to thermal neutrons would be difficult to distinguish from elastic alpha recoils, washing out the directional resolution. Again, the thermal signal has already lost most of the directional information and only provides a rate. Further, ^{3}He continues to be an expensive item to purchase. This added component to the gas composition could potentially double the cost of the entire detector.

One novel approach is to add boron wire strung cylindrically through the chamber. Each wire would have a known radial position, allowing a position cut to be applied in the image in order to separate the thermal neutron from the fast neutron signal. In the reaction between ^{1}0Boron and thermal neutrons, an alpha and a ^{7}Li isotope is created. Either the alpha or the ^{7}Li would be emitted from the boron wire with enough energy to allow detection through the typical image, PMT, and CSP channels. Showing an increase in thermal neutron activity while also showing a weak fast neutron signal in the vicinity increases the likelihood that a source is present.

8.4 Conclusion

In conclusion, this work demonstrates a new technology that has promising applications in military searches, IAEA inspections, emergency response operations, and portal security. The ability to locate a source of fast neutrons to within 60 cm from 2m away on a single pass from a backpack-sized detector is the first demonstrated capability for a directional, portable fast neutron detector. With future studies covering higher pressures, improved image signal to noise, and adding thermal neutron sensitivity, this technology can provide a capability that is not yet available in a one-person portable package.

Appendix A

Equipment and Source Calibrations

This detector used a CREMAT Charge Sensitive Preamplifier (CSP), a Ludlow 3.5" Photomultiplier Tube (PMT), and an AlazarTech ATS860 PCI digitizer. This equipment required calibration prior to using it for measurements. The CREMAT CSP and evaluation board was calibrated with a Rigol waveform generator, passed through the test-in port, and read-out through the ATS 860 digitizer. The PMT was calibrated with an alpha source with a known energy spectrum. These calibrations are discussed in this appendix.

A.1 Calibration Source

For the majority of this work, a 0.9μCi Americium-241 source was used with a small thickness of foil as a moderator. Am-241 releases two primary alpha particle energies in the decay to Np-247, with energies of 5.476 and 5.433 MeV [110]. Due to range straggling in the foil, the energy spectrum of these alpha particles was reduced and broadened, as depicted in Figure A-1. The alpha source was given a short collimator in order to prevent alpha tracks from ending short at the anode plane.

With the broad spectrum, adding any additional moderator would wash out any peak, causing an almost impossible scenario to calibrate the detector's gain, due to lack of peak. As such, no additional moderating material was used, but rather, the alpha particles traversed the full diameter of the detector's field cage at lower pressures and simulations were used to calculate the expected number of electrons released in the recoil. In this set-up, at pressures of 300 and 600 Torr for triple mesh experimentation, a significant majority of the emitted alpha particle would traverse

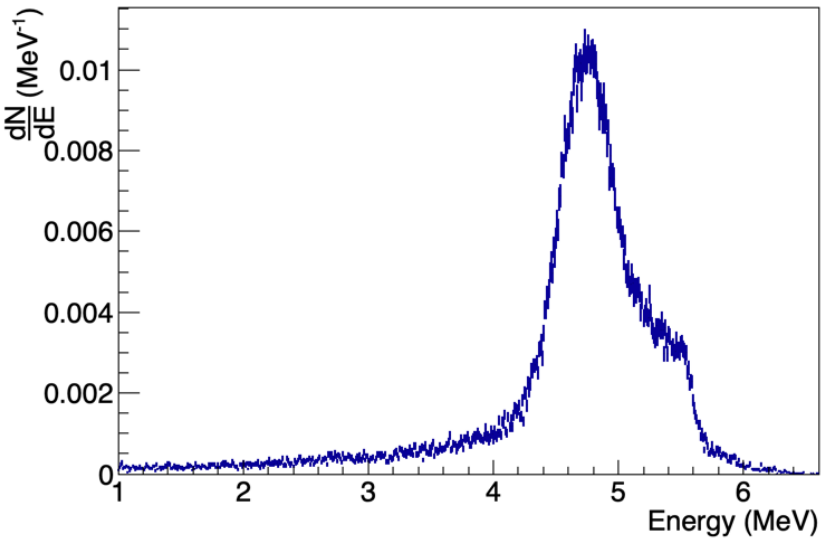

Figure A-1: The energy spectrum of the Am-241 0.9 μCi source. The spectrum was built by first calibrating a Passive Implanted Planar Silicon (PIPS) detector with an alpha source of known energy in moderate vacuum. The alpha calibration source was then replaced with the source from this work, measuring and recording the energy spectrum.

the full width of the field-cage without picking up any electrons. In this set-up, the alpha particles maintained a relatively constant number of generated electrons, producing a peak related to the amount of energy lost and ionizations produced over the diameter of the field cage. This peak can then be used to calibrate gain settings.

At each pressure, simulations were run in Garfield+, sampling from the measured Am-241 alpha energy spectrum distribution, and producing the expected distribution of electrons in the alpha track within the active volume of the TPC. At each pressure and each voltage setting, the curve produced from the CSP and PMTs were fitted against this expected curve by adjusting one variable: the single electron gain in the avalanche. As such, each point on the gain curve represents a least squares fit between a simulated number of electrons and the measurement of CSP and/or PMT data with a calibration factor.

A.2 Work Function

The work function was not reported in the literature for a gas mixture of 90% ^{4}He and 10% CF_4 but is an important input to the measurement of the gain. As such, the

work function was measured by running at a higher pressure in order to decrease the track length and increase the number of electrons created in the active volume of the detector. However, even at higher pressure, a majority of the tracks were longer than the anode plate. A heavily reduced field cage was used to reduce the complexity of the system. The two- or three-mesh amplification region was replaced with a flat plane anode to reduce any possible avalanche occurring in the immediate vicinity of the mesh wires where the field strength increases rapidly. Data was primarily collected with the CSP in this setup, where the CSP had been calibrated as discussed in the next section. The mean of the first 100 data points in the waveform was subtracted from the maximum value of the smoothed waveform. This accounted for the bias offset in the CSP. These values were recorded for 10,000 alpha recoils.

Since many of the tracks were longer than the anode plane, simulations were conducted in Garfield+ where the only variable changed was the work function for the fill gas to determine the distribution of total electrons liberated in the active volume. The work function was varied from 35 eV to 47 eV. Each of these simulated data sets were then compared to the actual data in a bin-to-bin mean squared error. The least squared error across the variation of the simulated work function is shown in Figure A-2.

The work function was expected to occur between 44 eV as measured for pure helium and 34 eV as measured for pure CF_4 [64, 111]. Considering the necessity to use simulations to approximate the work function, an increased uncertainty was placed on the measured value.

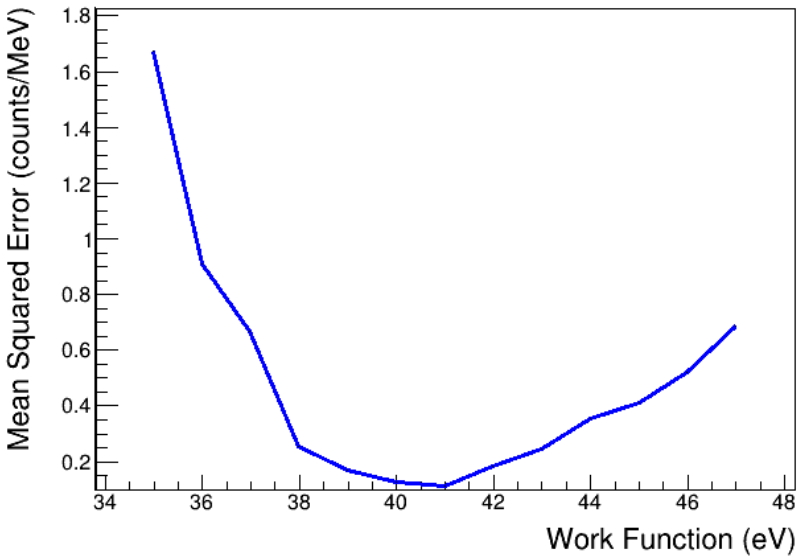

Figure A-2: The measurement of the work function using simulations fit to data by a least squares method. The simulations were run at work functions ranging from 35 to 47 and each batch used to computed the squared error between the two curves. This work function is therefore given a value of 41 $\pm$ 2 eV. The error on the work function is primarily derived from the use of simulations to correct for the discrepancy between the track lengths and the anode plane dimensions.

A.3 Charge Sensitive Preamplifier (CSP) Calibration

The CSP evaluation board used in this research offered a test input BNC plug that allowed test waves to be used for calibration. The CSPs were calibrated by passing square waves from a Rigol function generator through the test port and read at the ATS860 digitizer. The test port was terminated at 47 Ohms resulting in a 52% drop in voltage and capacitively coupled to the input channel by a 1 pF capacitor. The wave amplitudes were varied every 100 recorded waveforms. After each 100 data points, the 100 CSP waveform maximums were fit with a Gauss and the mean and standard deviation were recorded. The square pulses were also directly recorded, placed in a histogram, and later fit with a Gauss function to pull the mean and standard deviation. These data points were plotted against each other and fit with a linear function to determine the slope. An example of the fitting is provided for a CSP-110 in Figure A-3. The values plotted account for the input voltage drop. The four CSPs used in this research were found to agree with the manufacturer specifications to less than 1% deviation.

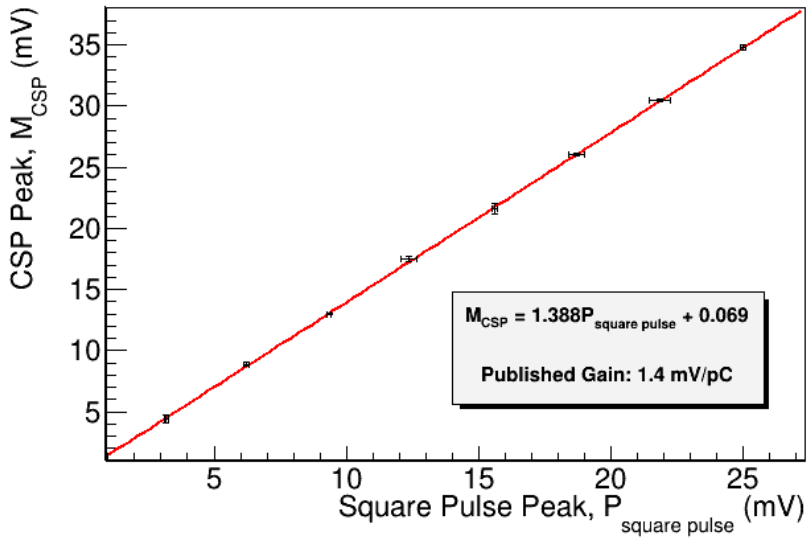

Figure A-3: An example of a linear fit to determine the gain for the Charge Sensitive Preamplifiers, the Cremat 110 CSP. A square wave pulse was supplied through the test port of the CSP and measured on an ATS860 PCI digitizer. The slope in this curve represents the measured gain, in mV/pC. As can be seen, the measured value agrees with the published value to better than 1%.

A.4 Calibration of the Ludlow 3.5" Photomultiplier Tube (PMT)

In order to significantly boost the performance of the PMT compared to previous versions of the DMTPC detector, a 3.5" Ludlow PMT placed in close proximity to the amplification region was used. The PMT was directly adjacent to the avalanche region on the other side of a large 3.75" viewport. In order to calibrate the detector in the anticipated operational regime, the alpha source with the previously measured energy spectrum was used and the detector was operated at the expected voltage, and hence gain, settings. The source was kept close to the avalanche region in order to minimize effects of diffusion. While the peak was broad for the calibration source, it served as a reasonable calibration due to the higher activity compared to a more typical mono-energetic calibration source.

The alpha source was kept in the same acetyl collimater discussed earlier in this chapter, which placed the alpha source approximately 1.5 cm outside the active volume of the detector. As such, approximately 20% of the energy was already lost before entering the detector. Further, the PMT was close enough that solid angle

corrections became a significant factor in the calibration. As such, each pulse was adjusted to account for the solid angle losses and then the collection of pulses were fit by a least squares with the measured energy spectrum. The only variable to adjust was the calibration factor, which was adjusted until the least squares was achieved.

Appendix B

Calculating Reaction Rates

In order to accurately predict and compare the performance of the detector in a variety of conditions, the reaction rate of the detector was computed and simulated in a variety of conditions. This appendix covers the calculation of the reaction rate for the cosmic neutron background and the simulation for the reaction rates for AmBe source runs.

B.1 Cosmic Neutron Energy Spectrum

The cosmic neutron spectrum spans many orders of magnitude and extends into very high energies. Many studies have been published analyzing this spectrum; this calculation uses the empirical formula for the energy spectrum produced by Gordon *et al* [93]. This spectrum is reproduced in Figure 5-2. Further, the neutron-alpha elastic recoil angular differential distributions from 10 keV up to 20 MeV were downloaded from the Evaluated Neutron Data File (ENDF) [1]. For a flat incident neutron spectrum, this data is reproduced in Figure B-1(b). After downloading the data from ENDF, the data is re-binned into uniform binning to ease further calculations.

From the incident neutron flux and the angular differential distribution, the angular differential distribution is scaled to match the incident neutron flux and modified to account for interaction probabilities for neutron-helium elastic scattering. In other words, if this two dimensional distribution is projected onto the energy axis, the distribution would match the neutron flux. At each data point in the two dimensional distribution, the knowledge of the incident neutron energy and the neutron recoil angle provides the ability to convert the neutron recoil angle to the alpha recoil energy. This is completed by an assumption of conservation of energy and conservation of an-

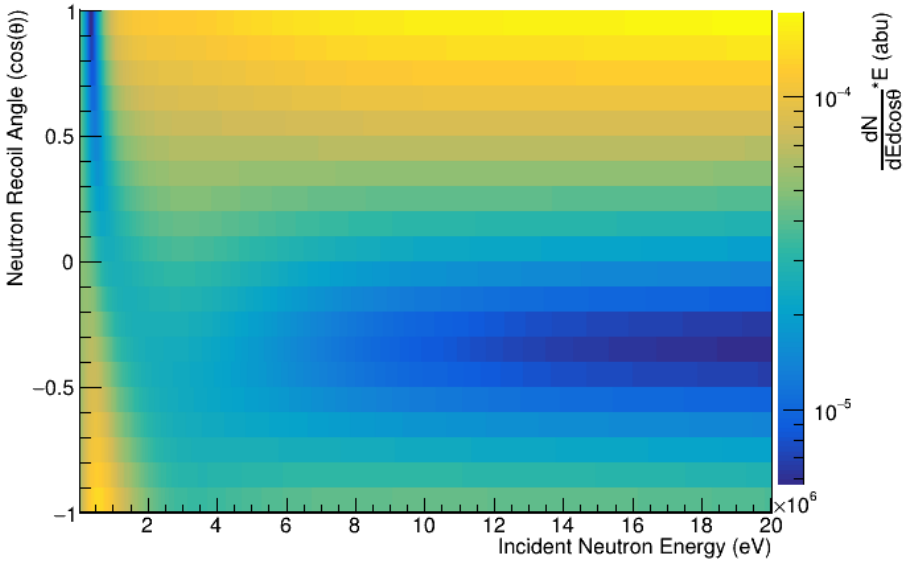

Figure B-1: The elastic scattering, angular, differential distribution for a flat neutron energy spectrum from 10keV to 20MeV, built from data downloaded from the Evaluated Neutron Data File [1]. This distribution is normalized into a two-dimensional distribution, normalized across scattering angle and incident neutron energy.

gular momentum, from equations 2.1 and 2.2. Combining these equations and solving for the alpha recoil energy as a function of incident neutron energy and neutron recoil angle gives the ability to convert the ordinate from the cosine of the scattering angle to the alpha recoil energy. This is denoted in Equation B.1.

$$E_\alpha = E_n\Big\{1 - \frac{1}{2}\Big((1 + \frac{(A-1)^2}{(A+1)^2}) + (1 - \frac{(A-1)^2}{(A+1)^2})cos\theta_C\Big)\Big\} \tag{B.1}$$

The result of converting the ordinate axis from the scattering angle to the alpha recoil energy and scaling for the cosmic flux reaction rate is depicted in Figure B-2.

When the curve from Figure B-2 is projected onto the ordinate, the expected differential alpha recoil rate is produced. This rate can be used to compare with cosmic run data to determine what fraction of events are expected to be direct cosmic neutrons versus ship effect neutrons or alpha decays in the detector construction material.

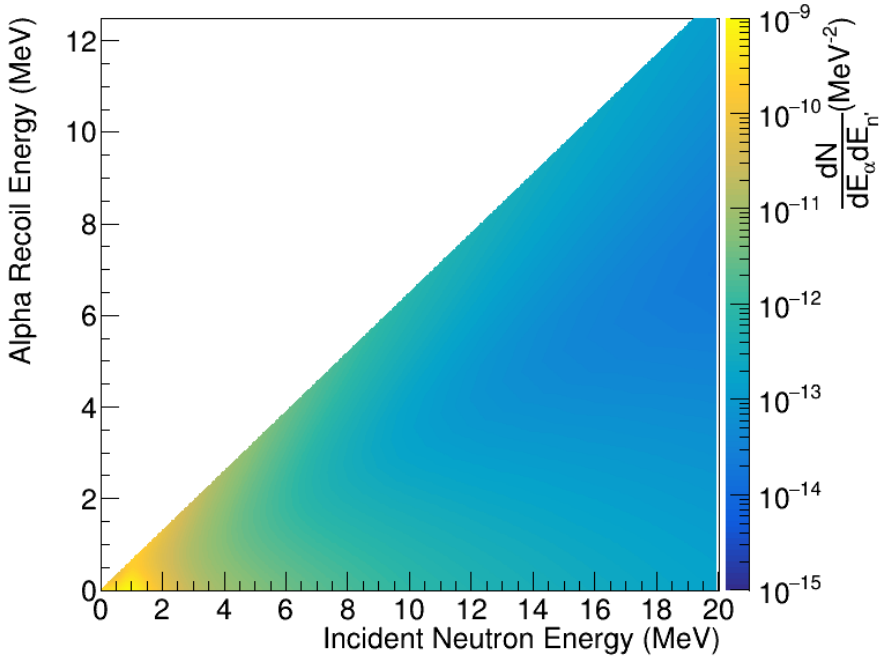

Figure B-2: The expected distribution of alpha energy given a cosmic neutron energy flux from Figure 5-2(a). The two dimensional plot projected onto the abscissa is the cosmic flux, scaled by the interaction rate. The interaction rate can be seen as the brightest spot occurring around 1 MeV, where the helium cross section is the greatest. When projected onto the ordinate, the expected spectrum of alpha recoil energies from direct cosmic shower neutrons is produced. This is depicted in Figure 5-4.

Bibliography

[1] M.B. Chadwick et al. Endf/b-vii.1 nuclear data for science and technology: Cross sections, covariances, fission product yields and decay data. *Nuclear Data Sheets*, 112(12):2887–2996, 2011. Special Issue on ENDF/B-VII.1 Library.

[2] José N. Reyes Jr. Nuscale plant safety in response to extreme events. *Nuclear Technology*, 178(2):153–163, 2012.

[3] Exploring the natrium™ technology's energy storage system, October 2020. [Online].

[4] Nuscale: Diverse applications, 2021. [Online].

[5] Michelle Galloway et al. Simulation and detector response for the high efficiency multimode imager. *Nuclear Instruments and Methods in Physics Research Section A: Accelerators, Spectrometers, Detectors and Associated Equipment*, 652(1):641 – 645, 2011.

[6] Andrew Haefner, Ross Barnowski, Paul Luke, Mark Amman, and Kai Vetter. Handheld real-time volumetric 3-d gamma-ray imaging. *Nuclear Instruments and Methods in Physics Research Section A: Accelerators, Spectrometers, Detectors and Associated Equipment*, 857:42–49, 2017.

[7] Yidong Fu, Yang Tian, Yulan Li, Jian Yang, and Jin Li. Directional fast neutron detection using a time projection chamber and plastic scintillation detectors. *Nuclear Instruments and Methods in Physics Research Section A: Accelerators, Spectrometers, Detectors and Associated Equipment*, 954:161445, 2020. Symposium on Radiation Measurements and Applications XVII.

[8] *An active interrogation detection system (ACTINIDES) based on a dual fast neutron/gamma-ray coded aperture imager*. IEEE, 2012.

[9] Nuclear powers pennsylvania: History, March 2021. [Online].

[10] Dwight D. Eisenhower. Text of the address delivered by the president of the united states before the generay assembly of the united nations in new york city tuesday afternoon, december 8, 1953.

[11] International atomic energy agency: Statute, March 2021. [Online].

[12] Elisabeth Roehrlich. Iaea history research project: Timeline. `https://iaea-history.univie.ac.at/timeline`, June 2020.

[13] *Guidance for States Implementing Comprehensive Safeguards Agreements and Additional Protocols*. Number 21 in Services Series. International Atomic Energy Agency, Vienna, 2016.

[14] Treaty on the non-proliferation of nuclear weapons (npt).

[15] William D. Watson. Trust, but verify: Reagan, gorbachev, and the inf treaty. *The Hilltop Review*, 5(5):22–38, December 2011.

[16] Justin V. Anderson and Amy J. Nelson. The inf treaty: A spectacular, inflexible, time-bound success. *Strategic Studies Quarterly*, 13(2):90–122, 2019.

[17] Alexander Glaser, Boaz Barak, and Robert J. Goldston. A zero-knowledge protocol for nuclear warhead verification. *Nature*, 510:497–502, 2014.

[18] Nuclear Smuggling Detection and Deterrence FY 2016 Data Analysis Annual Report: A Summary of Data Received and Analyzed by ORNL. Technical report, Oak Ridge National Laboratory, 2017. Accessed 8-May-2019.

[19] Ezra Engel and Areg Danagoulian. A physically cryptographic warhead verification system using neutron induced nuclear resonances. *Nature Communications*, 10:4433, 2019.

[20] Gordon Corera. *Shopping for Bombs: Nuclear Proliferation, Global Security, and the Rise and Fall of the A.Q. Khan Network*. Oxford University Press, New York, 2006.

[21] Iran: Nuclear, June 2020. [Online; updated June 2020].

[22] Hartigan Kelsey, Hinderstein Corey, Newman Andrew, and Squassoni Sharon. *A New Approach to the Nuclear Fuel Cycle : Best Practices for Security, Nonproliferation, and Sustainable Nuclear Energy.* Center for Strategic '|&' International Studies, 2015.

[23] Matthew P. Crozat, Jor-Shan Choi, Robert Hill, and Victor Reis. *Nuclear Fuel Leasing, Recycling and Proliferation: Modeling a Global View*. Lawrence Livermore National Laboratory, 3 2004.

[24] J. Carson Mark, Frank Von Hippel, and Edward Lyman. Explosive properties of reactor-grade plutonium. *Science & Global Security*, 17(2-3):170–185, 2009.

[25] Gary Philips, David Nagel, and Timothy Coffey. A primer on the detection of nuclear and radiological weapons. page 72, 05 2005.

[26] J.G. Wilson. *The Principles of Cloud-Chamber Technique*. Cambridge University Press, 2014.

[27] Glenn F Knoll. *Radiation detection and measurement*. John Wiley, Hoboken, N.J. SE - xxvi, 830 pages : illustrations ; 26 cm, 4th ed. edition, 2010.

[28] J. Kataoka et al. Ultracompact compton camera for innovative gamma-ray imaging. *Nuclear Instruments and Methods in Physics Research Section A: Accelerators, Spectrometers, Detectors and Associated Equipment*, 912:1–5, 2018. New Developments In Photodetection 2017.

[29] Steve Fetter et al. Detecting Nuclear Warheads. Technical report, 1990.

[30] Brian Henderson. Linac based photofission inspection system employing novel detection concepts. *Nuclear Instruments and Methods in Physics Research Section A: Accelerators, Spectrometers, Detectors and Associated Equipment*, 652:124–128, 2011.

[31] Jill Rahon, Areg Danagoulian, Thomas D. MacDonald, Zachary S. Hartwig, and Richard C. Lanza. Spectroscopic neutron radiography for a cargo scanning system. *Nuclear Instruments and Methods in Physics Research Section A: Accelerators, Spectrometers, Detectors and Associated Equipment*, 820:141 – 145, 2016.

[32] A. Danagoulian, W. Bertozzi, C. L. Hicks, A. V. Klimenko, S. E. Korbly, R. J. Ledoux, and C. M. Wilson. Prompt neutrons from photofission and its use in homeland security applications. In *2010 IEEE International Conference on Technologies for Homeland Security (HST)*, pages 379–384, Nov 2010.

[33] Berthold Horn, Richard Lanza, Jayna Bell, and Gordon Kohse. Dynamic reconstruction. *Nuclear Science, IEEE Transactions on*, 57:193 – 205, 03 2010.

[34] Richard S. Woolf et al. Fast-neutron, coded-aperture imager. *Nuclear Instruments and Methods in Physics Research A*, 784:398–404, 2015.

[35] J. Brennan et al. Results from field tests of the one-dimensional Time-Encoded Imaging System. Technical report, Sandia National Laboratories, 09 2010.

[36] Jeremy M. Osborn et al. Computational and experimental forensics characterization of weapons-grade plutonium produced in a thermal neutron environment. *Nuclear Engineering and Technology*, 50(6):820–828, 2018.

[37] S. Ahlen et al. The case for a directional dark matter detector and the status of current experimental efforts. *International Journal of Modern Physics A*, 25(01):1–51, Jan 2010.

[38] Hidefumi Tomita. *Detector development for direction-sensitive dark matter research*. PhD thesis, Boston University, 2011.

[39] William L. Koch. Imaging the ionization track of alpha recoils for the directional detection of weapons grade plutonium. Master's thesis, Massachusetts Institute of Technology, Cambridge, MA 02139, 2013.

[40] Jeremy Lopez et al. A prototype detector for directional measurement of the cosmogenic neutron flux. *Nuclear Instruments and Methods in Physics Research Section A: Accelerators, Spectrometers, Detectors and Associated Equipment*, 673:22 – 31, 2012.

[41] Andor Oxford Instruments. ixon ultra: The world's highest performanceback-illuminated emccds. `https://andor.oxinst.com/products/ixon-emccd-cameras`, 1 2021.

[42] Apogee Instruments Inc. Alta u6: High performance cooled ccd camera system. `http://www.kusastro.kyoto-u.ac.jp/~iwamuro/Kyoto3m/u6.pdf`, 1 2021.

[43] Jessica Orwig. Time projection chambers: a milestone in particle detector technology. `https://www.symmetrymagazine.org/article/october-2012/time-projection-chambers-a-milestone-in-particle-detector-technology`, 2012 (accessed 29 November 2020).

[44] The alice time projection chamber (tpc). `http://aliceinfo.cern.ch/Public/en/Chapter2/Chap2_TPC.html`, accessed 29 November 2020.

[45] T2K ND280 TPC collaboration. Time projection chambers for the t2k near detectors, 2010.

[46] Cosmin Deaconu et al. Measurement of the directional sensitivity of dark matter time projection chamber detectors. *Phys. Rev. D*, 95:122002, Jun 2017.

[47] M Gai et al. An optical readout tpc (o-tpc) for studies in nuclear astrophysics with gamma-ray beams at higs. *Journal of Instrumentation*, 5(12):P12004–P12004, Dec 2010.

[48] Walter Blum, Werner Riegler, and Luigi Rolandi. *Particle detection with drift chambers*. Springer, 2008.

[49] Cosmin Deaconu. *A Model of the Directional Sensitivity of Low-Pressure CF 4 Dark Matter Detectors*. PhD thesis, Massachusetts Institute of Technology, Cambridge, MA 02139, 2015.

[50] A. Kaboth et al. A measurement of photon production in electron avalanches in cf4. *Nuclear Instruments and Methods in Physics Research Section A: Accelerators, Spectrometers, Detectors and Associated Equipment*, 592(1):63 – 72, 2008.

[51] L M S Margato et al. Effective decay time of CF4 secondary scintillation. *Journal of Instrumentation*, 8(07), July 2013.

[52] Anna Peisert and Fabio Sauli. Drift and Diffusion of Electrons in Gases: A Compilation (With an Introduction to the Use of Computing Programs). Technical report, CERN, 1984.

[53] Asher Kaboth. *Detecting the Invisible Universe with Neutrinos and Dark Matter*. PhD thesis, Massachusetts Institute of Technology, Cambridge, MA 02139, 2012.

[54] S. F. Biagi. Monte carlo simulation of electron drift and diffusion in counting gases under the influence of electric and magnetic fields. *Nuclear Instruments and Methods in Physics Research Section A*, 421:234–240, 1999.

[55] J. L. Pack, R. E. Voshall, A. V. Phelps, and L. E. Kline. Longitudinal electron diffusion coefficients in gases: Noble gases. *Journal of Applied Physics*, 71(11):5363–5371, 1992.

[56] K. Baraka et al. Garfield++. `https://garfieldpp.web.cern.ch/garfieldpp/`, June 2020.

[57] James F. Ziegler, M.D. Ziegler, and J.P. Biersack. Srim – the stopping and range of ions in matter (2010). *Nuclear Instruments and Methods in Physics Research Section B: Beam Interactions with Materials and Atoms*, 268(11):1818 – 1823, 2010. 19th International Conference on Ion Beam Analysis.

[58] G J M Hagelaar and L C Pitchford. Solving the boltzmann equation to obtain electron transport coefficients and rate coefficients for fluid models. *Plasma Sources Science and Technology*, 14(4):722–733, oct 2005.

[59] Yuri P. Raizer. *Gas Discharge Physics*. Springer-Verlag, 1987.

[60] Robert J. Esterling and Norman H. Lipman. Helium gas scintillation. *Review of Scientific Instruments*, 36(4):493–497, 1965.

[61] A. Pansky, A. Breskin, A. Buzulutskov, R. Chechik, V. Elkind, and J. Va'vra. The scintillation of cf4 and its relevance to detection science. *Nuclear Instruments and Methods in Physics Research Section A: Accelerators, Spectrometers, Detectors and Associated Equipment*, 354(2):262–269, 1995.

[62] M. M. Bibby, B. J. Toubelis, and G. Carter. Ionisation and dissociation in cf4. *Electronics Letters*, 1(2):50–51, April 1965.

[63] Akihiro Takeuchi et al. Scintillation and ionization yields of helium–xenon gas mixture for application in neutron detectors. *Japanese Journal of Applied Physics*, 59(4):046001, mar 2020.

[64] Ian Wolfe. Measurement of work function in cf_4 gas, 2010.

[65] Ccc database. `https://www.lxcat.net`, retrieved on 1 December 2020.

[66] Matsusada Precision. High voltage power supplies for photomultiplier tube. https://www.matsusada.com/product/hvps2/module/j4j6/, 1 2020.

[67] Labjack Measurement and Automation. Ljtick-dac datasheet. https://labjack.com/support/datasheets/accessories/ljtick-dac, 1 2020.

[68] Labjack Measurement and Automation. Labjack u3-hv. https://labjack.com/sites/default/files/product_brief/U3-HV%20Product%20Brief%20v2.pdf, 1 2020.

[69] Cremat. Cr-113-r2.1 charge sensitive preamplifier. https://www.cremat.com/CR-113-R2.1.pdf, 10 2018.

[70] CAEN: Tools for Discovery. Dt5423: Quad desktop linear power distributor. https://www.caen.it/?downloadfile=4015, 7 2016.

[71] AlazarTech. Ats860: 250 ms/s 8-bit pci digitizer. https://www.alazartech.com/en/download/product/428/312/ats860-datasheet-and-specifications/1-2f/, 1 2020.

[72] FLI Camera. Microline ccd camera: Mlx285. http://www.flicamera.com/spec_sheets/MLx285.pdf, 1 2020.

[73] Jeremy Lopez. *First Results from a 20-Liter Prototype Dark Matter Detector with Directional Sensitivity*. PhD thesis, Massachusetts Institute of Technology, Cambridge, MA 02139, 2013.

[74] K. N. Buckland, M. J. Lehner, G. E. Masek, and M. Mojaver. Low pressure gaseous detector for particle dark matter. *Phys. Rev. Lett.*, 73:1067–1070, Aug 1994.

[75] Photonis Scientific Detectors. Cricket advanced intensifier adapter. https://www.photonis.com/products/crickettm, 3 2018.

[76] D.A. Orlov, J. DeFazio, S. Duarte Pinto, R. Glazenborg, and E. Kernen. High quantum efficiency s-20 photocathodes in photon counting detectors. *Journal of Instrumentation*, 11(04):C04015–C04015, apr 2016.

[77] Branko Leskovar. Microchannel plates. *Physics Today*, 30:42–49, 1977.

[78] A. Lehmann et al. Systematic studies of micro-channel plate pmts. *Nuclear Instruments and Methods in Physics Research Section A: Accelerators, Spectrometers, Detectors and Associated Equipment*, 639(1):144–147, 2011. Proceedings of the Seventh International Workshop on Ring Imaging Cherenkov Detectors.

[79] Léon A. Bosch. Image intensifier tube performance is what matters. https://stanfordcomputeroptics.com/download/GaAs%20versus%20SuperS25%20%20Tube%20performance%20matters%20000629.PDF.

[80] Shawn Henderson. *An Assessment of the Sensitivity of a Low Pressure Time Projection Chamber to the Direction of WIMP-Induced Nuclear Recoils*. PhD thesis, Massachusetts Institute of Technology, Cambridge, MA 02139, 2013.

[81] A. A. Grishkov, Y. D. Korolev, and V. A. Shklyaev. Monte carlo simulation for development of electron avalanches in nitrogen at moderate and high reduced electric field. *Physics of Plasmas*, 27(10):103504, 2020.

[82] J. S. Townsend. *The Theory of Ionization of Gases by Collision*. Nostrand Company, New York, 1910.

[83] O. Bunemann, T. E. Cranshaw, and J. A. Harvey. Design of grid ionization chambers. *Canadian Journal of Research*, 27a(5):191–206, 1949.

[84] R. Bevilacqua et al. A procedure for the characterization of electron transmission through frisch grids. *Nuclear Instruments and Methods in Physics Research Section A: Accelerators, Spectrometers, Detectors and Associated Equipment*, 770:64 – 67, 2015.

[85] Adel G E Abbady and A M El-Arabi. Naturally occurring radioactive material from the aluminium industry—a case study: the egyptian aluminium company, nag hammady, egypt. *Journal of Radiological Protection*, 26(4):415–422, nov 2006.

[86] Thorium. `https://pubs.usgs.gov/of/2004/1050/thorium.htm`, accessed 19 January 2021.

[87] K. Bunzl and W. Kracke. Natural radioactive contaminants in solder. *Nuclear Instruments and Methods in Physics Research Section A: Accelerators, Spectrometers, Detectors and Associated Equipment*, 238(1):191–192, 1985.

[88] K. O'Brien, H. A. Sandmeier, G. E. Hansen, and J. E. Campbell. Cosmic ray induced neutron background sources and fluxes for geometries of air over water, ground, iron, and aluminum. *Journal of Geophysical Research: Space Physics*, 83(A1):114–120, 1978.

[89] Y.-F. Wang, V. Balic, G. Gratta, A. Fassò, S. Roesler, and A. Ferrari. Predicting neutron production from cosmic-ray muons. *Phys. Rev. D*, 64:013012, Jun 2001.

[90] Richard T. Kouzes et al. Cosmic-ray-induced ship-effect neutron measurements and implications for cargo scanning at borders. *Nuclear Instruments and Methods in Physics Research, Section A: Accelerators, Spectrometers, Detectors and Associated Equipment*, 587(1):89–100, 2008.

[91] Estanislao Aguayo, Richard T. Kouzes, and Edward R. Siciliano. Ship effect neutron measurements and impacts on Low-Background experiments. *Pacific Northwest National Laboratory*, (PNNL-22953):5, 2013.

[92] N. Mascarenhas, J. Brennan, K. Krenz, P. Marleau, and S. Mrowka. A measurement of the flux, angular distribution and energy spectra of cosmic ray induced neutrons at fission energies. In *2007 IEEE Nuclear Science Symposium Conference Record*, volume 3, pages 2050–2052, 2007.

[93] M. S. Gordon et al. Measurement of the flux and energy spectrum of cosmic-ray induced neutrons on the ground. *IEEE Transactions on Nuclear Science*, 51(6):3427–3434, 2004.

[94] Takaumi KIMURA. Quantitative evaluation of multiple production of neutrons induced by cosmic rays in materials. *Journal of Nuclear Science and Technology*, 27(12):1147–1150, 1990.

[95] Takaumi Kimura. Quantitative evaluation of multiple production of neutrons induced by cosmic rays in materials. *Journal of Nuclear Science and Technology*, 27(12):1147–1150, 1990.

[96] James Ziegler. Terrestrial cosmic rays. *IBM Journal of Research and Development*, 40:19–40, 01 1996.

[97] John M. Clem and Lev I. Dorman. Neutron monitor response functions. *Space Science Reviews*, 93:335–359, July 2000.

[98] Waraporn Nuntiyakul et al. Bare neutron counter and neutron monitor response to cosmic rays during a 1995 latitude survey. *Journal of Geophysical Research: Space Physics*, 123, 08 2018.

[99] K.W. Geiger and L. Van Der Zwan. Radioactive neutron source spectra from 9be(α, n) cross section data. *Nuclear Instruments and Methods*, 131(2):315–321, 1975.

[100] Isao Murata, Iehito Tsuda, Ryotaro Nakamura, Shoko Nakayama, Masao Matsumoto, and Hiroyuki Miyamaru. Neutron and gamma-ray source-term characterization of ambe sources in osaka university. *Progress in Nuclear Science and Technology*, 4:345–348, 01 2014.

[101] J.W. Marsh, D.J. Thomas, and M. Burke. High resolution measurements of neutron energy spectra from ambe and amb neutron sources. *Nuclear Instruments and Methods in Physics Research Section A: Accelerators, Spectrometers, Detectors and Associated Equipment*, 366(2):340–348, 1995.

[102] Kyle S. Cranmer. Kernel estimation in high-energy physics. *Comput. Phys. Commun.*, 136:198–207, 2001.

[103] Rene Brun and Fons Rademakers. Root — an object oriented data analysis framework. *Nuclear Instruments and Methods in Physics Research Section A: Accelerators, Spectrometers, Detectors and Associated Equipment*, 389(1):81–86, 1997. New Computing Techniques in Physics Research V.

[104] S. Mochizuki et al. First demonstration of aerial gamma-ray imaging using drone for prompt radiation survey in fukushima. *Journal of Instrumentation*, 12, Nov 2017.

[105] Bruce Cornuelle, Peter Worcester, and Matthew Dzieciuch. Ocean acoustic tomography. *Journal of Physics: Conference Series*, 118:012002, 10 2008.

[106] Shuai Na, Xiaoyun Yuan, Li Lin, Julio Isla, David Garrett, and Lihong V. Wang. Transcranial photoacoustic computed tomography based on a layered back-projection method. *Photoacoustics*, 20:100213, 2020.

[107] Andrew Haefner et al. Handheld real-time volumetric 3-d gamma-ray imaging. *Nuclear Instruments and Methods in Physics Research Section A: Accelerators, Spectrometers, Detectors and Associated Equipment*, 857:42 – 49, 2017.

[108] Yidong Fu et al. Performance study of a directional fast neutron detection system based on TPC and plastic scintillation detectors. *JINST*, 14:P06034, 2019.

[109] Ams composite cylinders: Firefighting. `https://ams-composites.com/scba-cylinders-for-firefighters/`, 2021 (accessed 20 April 2021).

[110] Frank Asaro, F. L. Reynolds, and I. Perlman. The complex alpha-spectra of am^{241} and cm^{242}. *Phys. Rev.*, 87:277–285, Jul 1952.

[111] Nobumiti Ishida, Jun Kikuchi, and Tadayoshi Doke. The w values and fano factors in helium and argon-doped helium. *Japanese Journal of Applied Physics*, 31(Part 1, No. 5A):1465–1469, may 1992.